Nonlinear phononics and structural control of strongly correlated materials

Dissertation

zur Erlangung des Doktorgrades an der Fakultät für
Mathematik, Informatik und Naturwissenschaften

Fachbereich Physik
der Universität Hamburg

vorgelegt von

Roman Mankowsky

aus Berlin

Hamburg
2015

Hiermit erkläre ich an Eides statt, dass ich die vorliegende Dissertationsschrift selbst verfasst und keine anderen als die angegebenen Quellen und Hilfsmittel benutzt habe. Diese Arbeit lag noch keiner anderen Person oder Prüfungsbehörde im Rahmen einer Prüfung vor.

I hereby declare, on oath, that I have written the present dissertation on my own and have not used other than the mentioned resources and aids. This work has never been presented to other persons or evaluation panels in the context of an examination.

für Astrid, Panko und Miriam

Abstract

Mid-infrared light pulses can be used to resonantly excite infrared-active vibrational modes for the phase control of strongly correlated materials on sub-picosecond timescales. As the energy is transferred directly into atomic motions, dissipation into the electronic system is reduced, allowing for the emergence of unusual low energy collective properties. Light-induced superconductivity, insulator-metal transitions and melting of magnetic order demonstrate the potential of this method. An understanding of the mechanism, by which these transitions are driven, is however missing. The aim of this work is to uncover this process by investigating the nonlinear lattice dynamics induced by the excitation and to elucidate their contribution to the modulation of collective properties of strongly correlated materials.

The first signature of nonlinear lattice dynamics was reported in the observation of coherent phonon oscillations, resonant with the excitation of an infrared-active phonon mode in a manganite. This nonlinear phononic coupling can be described within a model, which predicts not only oscillatory coherent phonons dynamics but also directional atomic displacements along the coupled modes on average, which could cause the previously observed transitions. We verified this directional response and quantified the anharmonic coupling constant by tracing the atomic motions in a time-resolved hard x-ray diffraction experiment with sub-picometer spatial and femtosecond temporal resolution.

In a subsequent study, we investigated the role of nonlinear lattice dynamics in the emergence of superconductivity far above the equilibrium transition temperature, an intriguing effect found to follow lattice excitation of $YBa_2Cu_3O_{6+x}$. By combining density functional theory (DFT) calculations of the anharmonic coupling constants with time-resolved x-ray diffraction experiments, we identified a structural rearrangement, which appears and decays with the same temporal profile as the signature of superconductivity. DFT calculations of the electronic properties associated with the transient structure show an enhancement of superconductivity. A second important result of this study is the excellent agreement between the ab-initio microscopic theory and the experimental data, implying that this theory can be used to predict nonlinear phonon coupling in other materials.

Zusammenfassung

Dass die resonante Anregung von infrarot-aktiven Gitterschwingungen die Kontrolle von kollektiven Eigenschaften von stark korrelierten Materialien ermöglicht, zeigte sich in den letzten Jahren in der Beobachtung von Isolator-Metall Übergängen, dem Schmelzen magnetischer Ordnung sowie durch Licht induzierter Supraleitung. Trotz dieser experimentellen Erfolge blieb die eigentliche physikalische Ursache für diese Übergänge unklar. Das Ziel dieser Arbeit ist es, einen Beitrag zur Erforschung dieser Ursache zu leisten, indem die nichtlinearen Gitterdynamiken, die durch den Anregungsprozess ausgelöst werden, und deren Auswirkungen auf die kollektiven elektronischen Eigenschaften von stark korrelierten Materialien untersucht werden.

Die ersten Anzeichen von nichtlinearen Gitterwechselwirkungen wurden in einem Manganit entdeckt. Nach der Anregung einer infrarot-aktiven Gitterschwingung wurden kohärente Oszillationen einer anderen, Raman aktiven Mode beobachtet. Diese nichtlineare Kopplung verschiedener Schwingungsmoden kann mit einem Modell erklärt werden, das neben den kohärenten Oszillationen eine gerichtete Verschiebung der Atome entlang der gekoppelten Mode vorhersagt. Diese strukturellen Veränderungen könnten Ursache der beobachteten Phasenübergänge sein. In einem Experiment konnten wir diese Voraussage mit Hilfe von zeitaufgelöster Röntgenbeugung nachweisen und die zugehörige Kopplungskonstante messen.

In einer anschließenden Studie haben wir die Rolle der nichtlinearen Gitterdynamik in der Enstehung von Supraleitung weit oberhalb der Übergangstemperatur untersucht, die nach Gitteranregung von $YBa_2Cu_3O_{6+x}$ entdeckt wurde. Durch Kombination von zeitaufgelöster Röntgenbeugung mit Berechnungen der Kopplungskonstanten mittels Dichtefunktional Theorie (DFT), konnten wir die strukturelle Veränderung bestimmen, die auf denselben Zeitskalen erscheint und abklingt wie die Signatur der Supraleitung. DFT Berechnungen der elektronischen Eigenschaften in der transienten Kristallstruktur zeigen positive Auswirkungen auf die Supraleitung. Ein weiteres wichtiges Ergebnis dieser Studie ist die gute Übereinstimmung der theoretischen Rechnungen mit dem Experiment, woraus gefolgert werden kann, dass diese Theorie zukünftig genutzt werden kann, um Kopplungen von Schwingungsmoden in anderen Materialien vorauszusagen.

Contents

1

Introduction

Strongly correlated materials exhibit many interesting and potentially technologically useful properties, such as insulator-metal transitions [1, 2], colossal magnetoresistance [3, 4] and high temperature superconductivity [5]. The control of these properties with light pulses on sub-picosecond timescales opens possibilities for future applications in the design of photonic devices, as for instance ultrafast non-volatile data storage.

Many of their collective properties occur on energy scales below 100meV. While excitation with femtosecond light pulses in the visible has been shown to induce ultrafast phase transitions, the light directly couples to electronic excitations and inevitably heats up the electronic system, melting these low energy phenomena. Thus, switching between phases by reversing transitions with subsequent light pulses, as necessary for storage devices, is not possible.

One approach to overcome this problem is to drive the phase changes by coupling to low energy excitations such as vibrational modes of the crystal lattice. With the energy transferred directly into structural motions, dissipation into the electronic system is reduced, allowing for the emergence of unusual low energy collective properties. Light-induced superconductivity [6, 7, 8], insulator-metal transitions [9, 10] and melting of magnetic order [11, 12] demonstrate the potential of this method. An understanding of the microscopic mechanism, by which these transitions are driven, is however missing.

The aim of this work is to uncover this process by investigating the lattice dynamics induced by the excitation and elucidate their effect on collective properties of strongly correlated materials. These atomic motions are traced with a combination of lab-based optical techniques and time-resolved hard

3

x-ray diffraction with sub-picometer spacial and femtosecond temporal resolution at the Linac Coherent Light Source Free Electron Laser. In the following, strongly correlated materials are introduced and the experiments on the structural control of their properties presented, which form the basis for the research problem investigated in this work. A short summary of the structure of this thesis is given in the last section.

Strongly correlated materials

In the quantum mechanical description of metals, semiconductors and insulators, developed between 1928-1937 [13, 14, 15, 16], valence electrons are considered to move in an effective Coulomb potential, formed by periodically arranged ionic cores. Interactions between electrons are only taken into account as an *average* electric field, felt by otherwise non-interacting electrons, and are included in this potential. This description failed in predicting the electronic transport properties of strongly correlated materials, in which the Coulomb correlation, that is the Coulomb repulsion between electrons due to their spatial position, plays an important role. Their electronic and magnetic properties are already strongly affected by small structural changes. This sensitivity was first pointed out by Mott in 1949, who envisioned a crystal of atoms with one valence electron in a periodic lattice of variable distance d to describe the physics of strongly correlated materials [17, 18].

He argued, that for large values of d, the material must be insulating, as the motion of one electron from one atomic site to the next requires an activation energy $\epsilon = I - E$, given by the difference between ionization energy and electron affinity. For small values of d, the material must be a metal, because of the large overlap of the atomic wave functions. Thus, there must be a critical value d_0, at which a transition occurs from an insulator to a metal. At this lattice spacing, the activation energy decreases to zero, because the attractive force of the electron and the positively charged core it left behind is screened by other free charges. As a consequence, small structural changes can dramatically affect the electronic transport properties in materials, which are close to this critical value.

4

Such materials are practically realized in transition metal oxides. The oxygen ligands ionize the transition metal atoms, which are left with partially filled d-orbitals. The occupation of these orbitals and the degree of their overlap with the adjacent oxygen p-orbitals plays the dominant role in determining the electronic and magnetic properties of the material. The electronic transport properties result from a competition between delocalization due to orbital overlap, which is described as a tunneling of electrons from one transition metal site to the next and the onsite Coulomb repulsion, counteracting the occupation of one orbital by two electrons. This combination of local physics and long range interactions leads to the formation of high temperature superconductivity and other collective phenomena as mentioned above.

First experiments in manganites

The first attempt to control these phases by resonant lattice excitation with mid-infrared laser pulses was reported in 2007 [9] by switching the electronic state of $Pr_{0.7}Ca_{0.3}MnO_3$ (PCMO$_{0.3}$), a rare-earth manganite. Manganites can be pictured as a practical realization of Mott's gedankenexperiment. They crystallize in a Perovskite structure with the chemical formula AMnO$_3$. Their unit cell is comprised of Mn ions, surrounded by oxygen ligands in an octahedral coordination. The transport properties are derived from a competition between onsite Coulomb repulsion, which favors localization and an insulating ground state, and a lowering in kinetic energy due to increasing overlap of the orbital wave functions along the Mn-O-Mn bond, which promotes delocalization and metallic properties [19]. Replacing the A-site cations and dopants by atoms with ionic radii smaller than those of the Mn ions introduces rotational distortions of the MnO_6 octahedra. These distortions reduce the Mn-O-Mn bond angle α and, as a result, the overlap of the orbital wave functions along this direction as shown in panel (a) of Figure 1. The decrease in orbital overlap has the same effect as an increase in the lattice spacing d of the artificial crystal in the experiment of Mott described above - it favors charge localization and an insulating state. Figure 1 shows the temperature

5
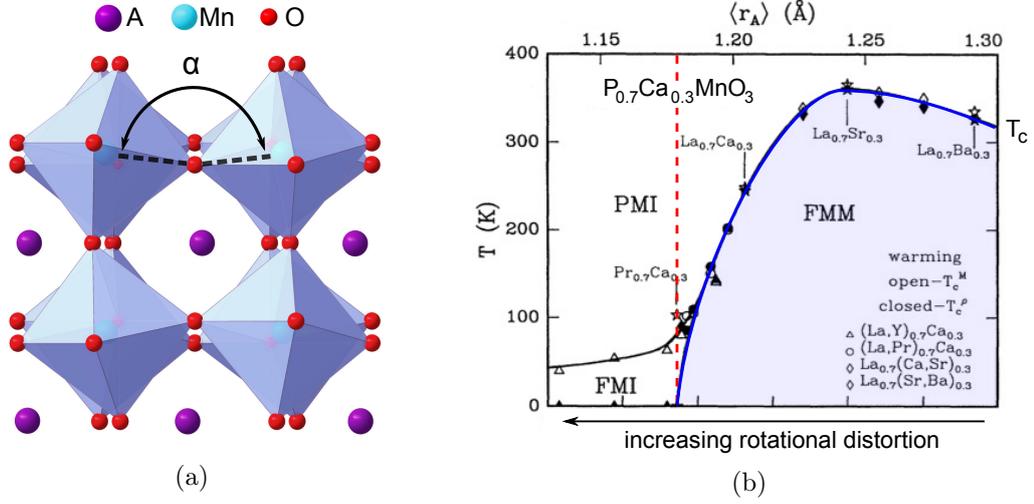
Figure 1: (a) AMnO$_3$ Perovskite structure. Replacing the A-site cations and dopants by atoms with ionic radii smaller than those of the Mn ions introduces rotational distortions of the MnO$_6$ octahedra and the Mn-O-Mn bond angle α. (b) Temperature dependent electronic phases of manganites with different chemical compositions. The Curie temperature T$_C$ decreases with increasing rotational distortions due to the reduction of orbital overlap. PCMO$_{0.3}$, marked by the red dashes line has no metallic phase anymore. The Figure of panel (b) has been adapted from [21].

dependent electronic phases of various manganites with different chemical compositions. The Curie temperature T$_C$, which marks the transition from a metallic to an insulating state, decreases with increasing rotational distortions, with Pr$_{0.7}$Ca$_{0.3}$MnO$_3$ (PCMO$_{0.3}$) showing no metallic phase anymore. PCMO$_{0.3}$ can thus be pictured as being close to the critical value and, therefore, very sensitive to small external perturbations. Indeed, the application of pressure has been shown to induce an insulator-metal transition by straightening the Mn-O-Mn bond angles [20]. This was the motivation for an attempt to induce a similar transition on ultrafast timescales by resonant lattice excitation with light pulses.

In the experiment, an infrared-active Mn-O stretching mode of PCMO$_{0.3}$ was resonantly excited and the transient sample conductivity determined by measuring the time resolved voltage drop across a 50Ω resistor. Following this excitation a transition into a metallic state was found, as evidenced by

an increase in conductivity by several orders of magnitude. The experiment further shows that the phase state of solids can be controlled by resonant lattice excitation. In 2011, two experiments involving resonant lattice excitation of manganites were reported, one of which found signatures of a nonlinear response of the crystal lattice [22, 11].

Coherent oscillations of a Raman mode were found to follow the excitation of $La_{0.7}Sr_{0.3}MnO_3$ ($LSMO_{0.3}$) with mid-infrared light pulses. The amplitude of these oscillations peaked, when the mid-infrared pulses were tuned to resonance with an infrared-active phonon mode. Such nonlinear phononic coupling was theoretically predicted more than 40 years ago, then called Ionic Raman Scattering [23, 24, 25]. Interestingly, this model predicts not only the observed coherent oscillations, but also a directional displacement of the atoms along the coupled phonon modes. The transformation of oscillatory atomic motions into directional changes of the crystal structure *on average* might explain the previously observed phase transitions. To evaluate, whether these displacements are large enough to drive phase changes, the real space amplitudes of the atomic motions have to be measured. This motivated the first experiment presented in this thesis, in which the atomic motions induced by the lattice excitation of $LSMO_{0.3}$ were traced with sub-picometer spatial and femtosecond temporal resolution using time resolved hard x-ray diffraction [26]. In this experiment, we verified the displacive response and quantified the nonlinear coupling constant.

Discovery of light-induced superconductivity in cuprates

In parallel, resonant lattice excitation was found to cause the emergence of transient superconductivity up to 20 K in the high temperature superconductor $La_{1.8-x}Eu_{0.2}Sr_xCuO_4$ at a doping level of x=1/8, at which the equilibrium superconducting phase is suppressed by a competing order of the charges and spins in stripes [6, 27]. This lattice excitation was proposed to melt the competing charge order and restore superconductivity. This interpretation
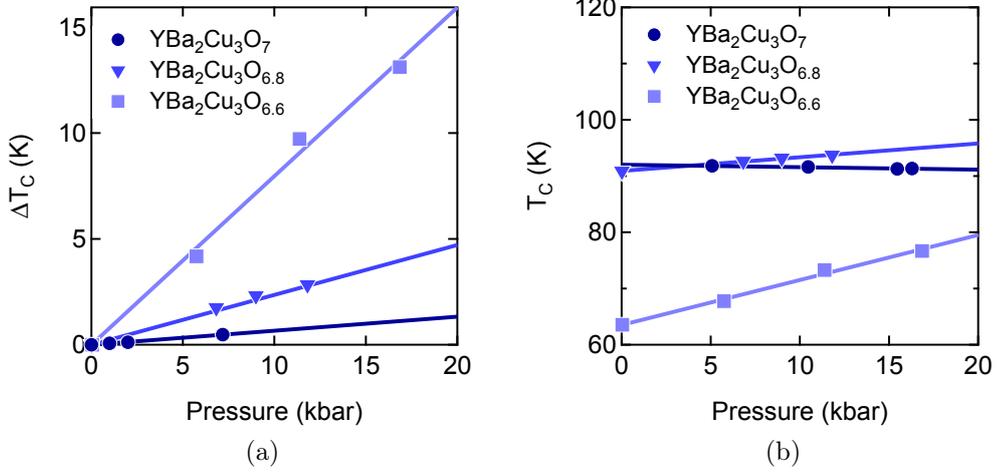
Figure 2: (a) The application of pressure increases the transition temperature T_c of $YBa_2Cu_3O_x$($YBCO_x$). This enhancement is smallest for optimally doped $YBCO_7$ samples and increases with decreasing hole doping, which corresponds to decreasing oxygen content x. (b) The transition temperature of underdoped samples can exceed the transition temperature of optimally doped $YBCO_x$. The data for these Figures was taken from [29, 30, 31].

was supported by a subsequent time-resolved resonant soft x-ray diffraction experiment, which confirmed the melting of charge order within the same timescale, during which superconductivity emerges [28].

These experiments demonstrated that resonant lattice excitation can be used to induce unusual low energy collective properties such as superconductivity. In following studies, the effect of vibrational excitation on superconductivity in $YBa_2Cu_3O_{6+x}$ (YBCO) was investigated. YBCO crystallizes in an orthorhombic structure comprising bilayers of CuO_2 planes. The interlayer region contains Cu-O chains, which serve as charge reservoir for these planes, increasing their hole doping with increasing oxygen content. The superconducting state is characterized by coherent tunneling of cooper pairs both within bilayers as well as between them through the interbilayer region. Above the transition temperature T_c, interbilayer coupling is lost, while signatures of coherent tunneling processes within the bilayers were found to persist up to temperatures far above T_c.

The coupling between structural degrees of freedom and superconductivity has been investigated extensively by comparing transition temperatures of different compounds and by measuring the structure and transport properties of superconductors with different doping levels under pressure. As shown in Figure 2 the transition temperature increases with the application of pressure [29, 30, 31]. While this effect is very small for optimally doped $YBa_2Cu_3O_7$ samples, it increases rapidly for samples with decreasing hole doping levels. Investigations of pressure-induced structural changes revealed a reduction in distance d between the planar copper atoms and the apical oxygen atoms in the interbilayer region as shown in Figure 3 [32]. Based on these results, the increase in transition temperature was proposed to be due to a charge redistribution from planes to chains, effectively increasing the hole doping mediated by the reduction in O-Cu distance d. This model explained, why the effect was smallest for $YBa_2Cu_3O_7$ samples, in which the hole doping is already at the optimal value. The application of pressure in $YBa_2Cu_3O_{6.8}$ was further found to raise the transition temperature above the highest value of optimally doped samples (see panel (b) of Figure 2).

These results raised the question of whether the modulation of this Cu-O distance by resonant excitation of the vibrational mode shown in Figure 3 could enhance superconductivity and increase the transition temperature T_c above its equilibrium value. In 2014, this lattice excitation was found to cause the emergence of transient superconductivity at temperatures as high as 300 K, far above the transition temperature of 90 K at optimal doping [7, 8].

The emergence of a superconducting state at such high temperatures cannot simply be explained by the melting of a competing order. Recalling that structural modifications by pressure increase T_c above its optimal value and that vibrational excitation can affect the structure in a similar way through nonlinear phonon coupling, we investigated the structural dynamics during the emergence of this effect. By combining density functional theory (DFT) calculations of the anharmonic coupling constants with time-resolved x-ray diffraction experiments, we identified a structural rearrangement, which appears and decays with the same temporal profile as the signature of su-
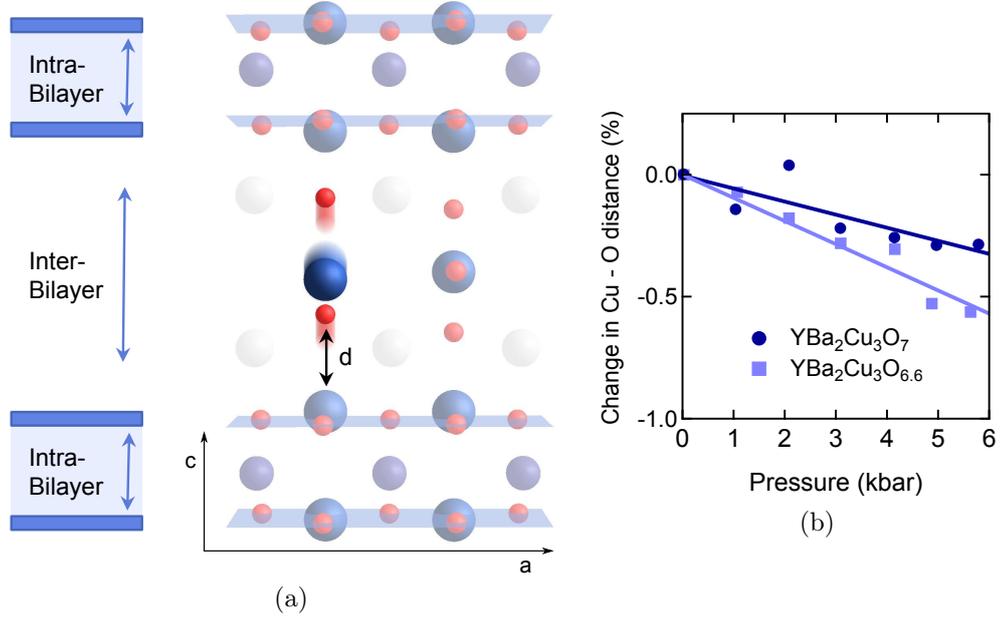
Figure 3: (a) Structure of orthorhombic $YBa_2Cu_3O_{6.5}$ and motions of the vibrational mode, modulating the apical oxygen-copper distance d at empty chain sites [35, 33]. (b) The application of pressure reduces this Cu-O distance and increases the transition temperature. Both effects are larger for underdoped samples. [32].

perconductivity [33]. DFT calculations of the electronic properties in the transient structure suggest positive effects on superconductivity, which was confirmed by a recent theoretical study [34]. In accordance with the application of pressure, the structural changes involve a decrease in Cu-O distance d, which is found by DFT calculations to cause a charge redistribution from the planes to chains. With these results, we found a possible explanation for the observed emergence of superconductivity at room temperature.

Thesis structure

This thesis is structured as follows. The theoretical framework used to explain nonlinear phononic coupling is presented in Chapter 1. The experiments on manganites, in which the displacive lattice response was first demonstrated, are covered in Chapter 2. Chapter 3 introduces high temperature superconductors of the cuprate family and the emergence of superconductivity in $YBCO_x$ following resonant lattice excitation. The measurements of the nonlinear lattice response, consisting of atomic displacements and coherent oscillations, are covered in chapters 4 and 5, followed by a conclusion of this thesis.

Chapter 1

Theory of nonlinear Phononics

In this chapter, the direct excitation of an infrared-active lattice vibration and its coupling to other phonon modes is discussed. The theory describing this process resembles in many ways the excitation by stimulated Raman scattering and was indeed first discussed as Ionic Raman Scattering, that is the ionic contribution to Raman scattering. Raman scattering describes an inelastic scattering process, in which a Raman phonon is either generated or absorbed through the interaction of the light with an intermediate electronic state. The scattered light thus either looses or gains energy, giving rise to intensity at the Stokes and anti-Stokes lines, respectively [36, 37]. Light in the visible and ultraviolet range with high energies compared to the phononic energy scales was used for Raman scattering experiments due to the availability of narrowband sources and spectrometers at these wavelengths. As these energies are far above phonon resonances, the ionic contribution to Raman scattering can be neglected.

With the development of CO_2 lasers in 1964, which allowed the generation of highly intense mid-infrared light, the investigation of ionic contributions to Raman scattering became a possibility. The first theories on nonlinear phonon coupling came up a few years later [23, 24, 25]. The ionic contribution to the Raman scattering process, in which the intermediate electronic states are replaced by an infrared-active phonon mode, as well as mixed electronic-ionic terms were calculated and compared to the pure electronic

13

normal   ionic

$$\omega_{\mathrm{r}} \qquad\qquad \omega_{\mathrm{r}}$$
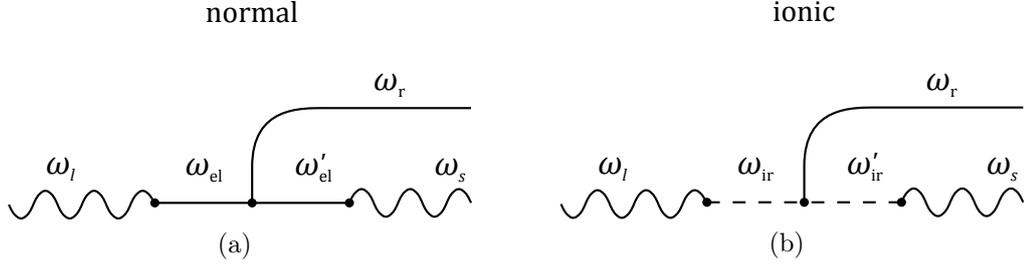
Figure 1.0.1: (a) In the normal Raman scattering process, a photon with frequency ω_l excites an intermediate electronic state ω_{el}, which is modulated by the absorption or generation of a Raman phonon with frequency ω_r and subsequently decays, emitting a photon with frequency $\omega_s = \omega_l \pm \omega_r$. (b) Ionic Raman scattering describes the same process with vibrational infrared-active intermediate states [25].

contribution (see Figure 1.0.1). Although the results published in 1971 indicated a substantial enhancement in scattering efficiency when tuning the light to resonance with an infrared active phonon mode, 15 years passed until the first experimental demonstration of an enhanced susceptibility in the vicinity of phonon resonances was published [38]. After the first signatures were discovered, several groups calculated the ionic contributions in different materials and improved the theory of ionic Raman scattering [39]. All theories were however focused on the calculation of Raman cross sections.

In this chapter, a theory of nonlinear phononics is presented with a focus on the lattice dynamics that can be induced in order to control the phase states of solids. Here, the resonant excitation of an infrared-active (IR) mode with femtosecond mid-infrared pulses is taken as starting point. This direct excitation can be described as an externally driven harmonic oscillator. Upon tuning the energy of the incident light field to the resonance frequency of the phonon mode, large amplitude oscillations can be excited. Note that the wavelength of mid-infrared light λ is four orders of magnitude larger than lattice constants a and its wave vector $|\mathbf{k}| = 2\pi/\lambda$ is thus approximately 0 compared to the wave vectors of lattice vibrations ($0 \leq |\mathbf{k}| \leq \pi/a$). Thus, due to momentum conservation only optical modes with finite frequency at $\mathbf{k} = 0$ can directly be excited. The nonlinear lattice dynamics induced by this excitation can be described as a coupling of this directly excited IR mode

to other phonon modes, adding mixed, higher order terms to the lattice potential. The response of a crystal lattice to strong, resonant excitation of an infrared-active phonon mode can thus be described by separating the crystal Hamiltonian into its linear and nonlinear terms H_0 and H_1. The linear term

$$H_0 = \sum_{\mathbf{k}} \frac{1}{2} \left(P_{\mathbf{k},\mathrm{ir}}^2 + \omega_{\mathbf{k},\mathrm{ir}}^2 Q_{\mathbf{k},\mathrm{ir}}^2 \right) + \sum_{\mathbf{q}} \frac{1}{2} \left(P_{\mathbf{q},\mathrm{j}}^2 + \omega_{\mathbf{q},\mathrm{j}}^2 Q_{\mathbf{q},\mathrm{j}}^2 \right) - V\left(t \right)$$

holds the kinetic energy and harmonic contribution to the lattice potential energy and describes harmonic oscillations of the atoms about their equilibrium positions. Here, $P_{\mathbf{k},\mathrm{ir}}$, $\omega_{\mathbf{k},\mathrm{ir}}$, $Q_{\mathbf{k},\mathrm{ir}}$ and $P_{\mathbf{q},\mathrm{j}}$, $\omega_{\mathbf{q},\mathrm{j}}$, $Q_{\mathbf{q},\mathrm{j}}$ are the momentum, frequency and normal coordinate of the infrared mode and the mode coupled to it at wave vectors $\mathbf{k}$ and $\mathbf{q}$, respectively. The external potential $V(t) \sim E(t) Q_{\mathbf{k},\mathrm{ir}} \delta_{\mathbf{k},\mathbf{0}}$ describes the incident electric field, tuned to resonance with the infrared mode. Note that the infrared mode is an optical mode excited at $\mathbf{k} \approx 0$, which is not necessarily the case for the coupled mode as discussed in the sections on cubic and quartic coupling. The interaction Hamiltonian can be expressed as an expansion in the normal coordinates of the driven infrared-active mode and the mode coupled to it with the anharmonic coupling constants a_{nm} by:

$$H_1 = \sum_{\mathbf{q}} \big(a_{12} Q_{\mathbf{0},\mathrm{ir}} Q_{\mathbf{q},\mathrm{j}}^2 + a_{21} Q_{\mathbf{0},\mathrm{ir}}^2 Q_{\mathbf{q},\mathrm{j}} + a_{22} Q_{\mathbf{0},\mathrm{ir}}^2 Q_{\mathbf{q},\mathrm{j}}^2 +$$
$$+ a_{13} Q_{\mathbf{0},\mathrm{ir}} Q_{\mathbf{q},\mathrm{j}}^3 + a_{31} Q_{\mathbf{0},\mathrm{ir}}^3 Q_{\mathbf{q},\mathrm{j}} + \ldots \big). \qquad (1.0.1)$$

1.1 Cubic order coupling

Nonlinear phononics is typically dominated by the lowest order anharmonicity, which is cubic. Cubic coupling involves a displacive force that acts onto the crystal lattice in two ways. Firstly, a phononic analogue to rectification in nonlinear optics causes a quasi-static displacement along the normal mode coordinates of all coupled phonon modes. Secondly, whenever the displacive force rises promptly compared to the period of any of the anharmonically coupled modes, coherent oscillatory motions of these modes are excited. This second effect is the ionic equivalent of stimulated Raman scattering. The materials $La_{0.7}Sr_{0.3}MnO_3$ and $YBa_2Cu_3O_{6.5}$, in which cubic nonlinearities have been measured [22, 26, 33, 40], have a centrosymmetric crystal structure. This inversion symmetry has to be conserved by the interaction Hamiltonian. It follows that the term $a_{12}Q_{ir}Q_j^2$ is forbidden as any infrared mode Q_{ir} is odd (breaks inversion symmetry), whereas Q_j^2 is even (conserves inversion symmetry). Further, Q_j in $a_{21}Q_{ir}^2Q_j$ has to be a Raman mode (Q_R) as Q_{ir}^2 is even. The interaction Hamiltonian thus reduces to

$$H = \sum_{\mathbf{q}} a_{21}Q_{\mathbf{0},ir}^2 Q_{\mathbf{q},R}.$$

Since the infrared mode is driven at $\mathbf{k} = 0$, only Raman modes at wave vector $\mathbf{q} = 2\mathbf{k} = 0$ can be excited through cubic coupling. The sum over the wave vector can be omitted and the total Hamiltonian written as

$$H = \frac{1}{2}\left(P_{ir}^2 + \omega_{ir}^2 Q_{ir}^2\right) + \frac{1}{2}\left(P_R^2 + \omega_R^2 Q_R^2\right) - a_{21}Q_{ir}^2 Q_R - V\left(t\right).$$

For any finite distortion of the infrared mode Q_{ir}^*, the harmonic energy potential of the Raman mode is shifted along Q_R according to $V_R(Q_R) = \omega_R^2 Q_R^2/2 + a_{21}Q_{ir}^{*2}Q_R$ (see Figure 1.1.1a). This modification of the lattice potential allows the atoms to shift towards an energetically favorable structure along the Raman mode Eigenvector. Importantly, the direction of this shift is proportional to Q_{ir}^2 and therefore independent of the sign of Q_{ir}. On average, an oscillatory motion along Q_{ir} results in a directional shift of the

16
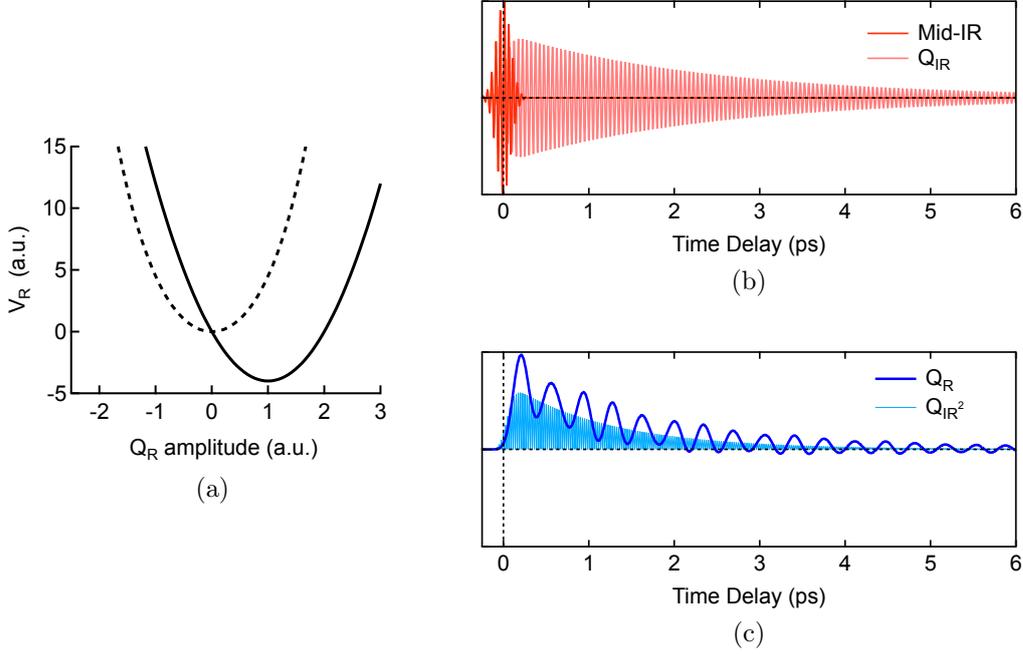
Figure 1.1.1: (a) A static distortion Q_{ir}^* shifts the equilibrium potential (dashed line) of all modes Q_R that are coupled through $Q_{ir}^2 Q_R$ coupling (solid line), displacing the potential energy minimum. (b) Response of the infrared-active normal coordinate Q_{ir} (light red) to resonant excitation by a 140fs mid-infrared pulse (red). (c) Within cubic coupling, a directional force proportional to Q_{ir}^2 (light blue) is exerted on the coupled mode Q_R, which displaces the atoms as long as the infrared mode oscillates coherently and drives coherent oscillations for modes Q_R with a period long compared to the rise time of this force. The images are taken from ([33, 40]).

energy potential of the Raman mode. The corresponding dynamical response is described by the equations of motion[41]

$$\ddot{Q}_{ir} + 2\gamma_{ir}\dot{Q}_{ir} + \omega_{ir}^2 Q_{ir} = f(t) + 2a_{21}Q_{ir}Q_R \qquad (1.1.1)$$

$$\ddot{Q}_R + 2\gamma_R\dot{Q}_R + \omega_R^2 Q_R = a_{21}Q_{ir}^2. \qquad (1.1.2)$$

Dissipation is accounted for phenomenologically by the terms containing γ, which is the inverse lifetime of the respective phonon mode $\gamma = \tau^{-1}$. The equation for the IR mode Q_{ir} describes a damped harmonic oscillator driven

by the electric field of the mid-infrared pulse $f(t) = A(t) \exp(i\omega_{\text{ir}}t)$, with $A(t)$ being the gaussian envelope of the pulse. Upon excitation, the atoms perform oscillations along the IR mode eigenvector about their equilibrium positions as shown in Figure 1.1.1b in light red. This motion, for a finite anharmonic coefficient a_{21}, exerts a directional force $F(t) = a_{21}Q_{\text{ir}}^2$ proportional to Q_{ir}^2 onto the coupled Raman mode that oscillates with twice the frequency of the infrared mode ω_{ir}. For excitations of high frequency infrared-active modes, these oscillations are too fast for the coupled Raman modes to follow. The effective force acting on the Raman modes is then proportional to the envelope of the squared infrared coordinate (Fig. 1.1.1c).

1.1.1 Modification of the crystal structure

This directional component forces the atoms to displace along all coupled Raman-mode eigenvectors. The displacement may occur fast or slow compared to the eigenfrequency of each coupled mode. It relaxes back to equilibrium over a timescale that is one half of the dephasing time of the infrared mode $\tau_{\text{ir}} = 1/\gamma_{\text{ir}}$ assuming no transition into a metastable state takes place. The one half factor for the relaxation time descends from the fact that the squared amplitude of the IR mode appears in the driving term in Equation 1.1.2. By exciting infrared modes to amplitudes of $\sim 10pm$, atomic displacements of several pm can be achieved.

As the Hamiltonian is the operator for the total energy, it must be even to all symmetry operations of the crystal point group. This also applies to the interaction Hamiltonian and all individual coupling terms. For the coupling to a certain Raman mode to be allowed by symmetry, the irreducible representation of the Raman mode must be part of the product group of the irreducible representation of the IR mode with itself $I(Q_{\text{R}}) \subseteq I(Q_{\text{ir}}) \otimes I(Q_{\text{ir}})$. The third order coupling term $a_{21}Q_{\text{ir}}^2 Q_{\text{R}}$ then belongs to the totally symmetric A_g irreducible representation. The direct product between irreducible representations can be found in the product table of the point group for a given crystal structure. Generally, if the excited infrared mode is non-degenerate (A_u or B_u), cubic coupling is only allowed to Raman modes of A_g symme-

try that do not break any symmetries. For degenerate infrared modes, the product group is multidimensional and coupling to Raman modes of many symmetries is possible.

While a certain selectivity is given by resonantly exciting an infrared-active phonon mode with specific coupling strengths to other Raman modes, the direction of the lattice displacement is set by the anharmonic coupling constant a_{21}, a property of the material. It is thus not possible to control the direction of the lattice displacement. Possible mechanisms to overcome this limitation are discussed in the next sections.

1.1.2 Coherent control

All effects discussed so far are derived from coupling between two phonon modes only. The force acting on the Raman modes only depends on the amplitude of the infrared mode, not on its phase. While the crystal structure can be modified for a certain time, the direction of the lattice displacement is set by the sign of the coupling constant a_{21} and cannot be controlled. If a certain lattice displacement favors one phase over another, it would be essential to control the direction of the displacement in order to switch between phases. This limitation may be overcome by exciting two phonon modes with similar frequencies and a fixed phase difference.

In most perovskites, the phonon modes along the three crystal axis have similar frequencies. These phonon modes can be individually excited by two cross-polarized mid-IR pulses with a stable relative phase, either generated separately or by splitting one mid-IR pulse into two. By changing the time delay between these two pulses, the relative phase of the phonon modes can be controlled. From the interaction Hamiltonian for cubic coupling of a Raman mode with two infrared modes

$$H = a_{111}Q_{\mathrm{ir1}}Q_{\mathrm{ir2}}Q_{\mathrm{R}} + a_{201}Q_{\mathrm{ir1}}^2 Q_{\mathrm{R}} + a_{021}Q_{\mathrm{ir2}}^2 Q_{\mathrm{R}},$$

the force acting on the Raman mode can be derived as

$$F(t) = a_{111}Q_{\mathrm{ir1}}(t)Q_{\mathrm{ir2}}(t) + a_{201}Q_{\mathrm{ir1}}^2(t) + a_{021}Q_{\mathrm{ir2}}^2(t).$$

The last two terms are equivalent to the cubic coupling discussed above and depend only on the amplitudes of Q_{ir1} and Q_{ir2}, respectively. The sign of the mixed term $F'(t) \sim |A_{ir1}(t)| \cos(\omega_{ir1}t) \cdot |A_{ir2}(t)| \cos(\omega_{ir2}t + \Delta\varphi)$ can however be controlled by the relative phase of the two infrared modes. Assuming both modes have a similar frequency, ($\omega_{ir1} \approx \omega_{ir2}$) the equation can be expressed as

$$F'(t) \sim |A_{ir1}(t)| \cdot |A_{ir2}(t)| \cos(\omega_{ir}t) \cos(\omega_{ir}t + \Delta\varphi).$$

For a phase difference of $\Delta\varphi = \pi$, the force clearly switches sign. The numerical solution to the two coupled equations of motion derived from the interaction Hamiltonian is shown in Figure (1.1.2) for the two cases of no phase difference and a phase difference of π.

It is important to note that only the mixed term $a_{111}Q_{ir1}Q_{ir2}Q_R$ changes sign. As noted in the previous chapter, cubic coupling of only one single IR mode is only allowed to A_g Raman modes. The mixed term thus dominates coupling to Raman modes of symmetries other than A_g. In rhombohedral crystals, the two degenerate E_u modes can couple to E_g Raman modes, for example, which has been observed experimentally in the manganite $La_{0.7}Sr_{0.3}MnO_3$ [22, 26] (see chapter 2). Note also, that for the excitation of two non-degenerate infrared-active modes Q_{ir1} and Q_{ir2}, the force exerted on the Raman mode will oscillate at the difference frequency of the IR modes as illustrated in Figure 1.1.3. For a directional excitation, the decay time of one of the two infrared-active modes must then be smaller than the half period of their difference frequency for the force to decay before switching sign. Further experiments have to show, whether the phase control allows switching forth and back between phases of solids.

(a) In Phase   (b) Out of Phase
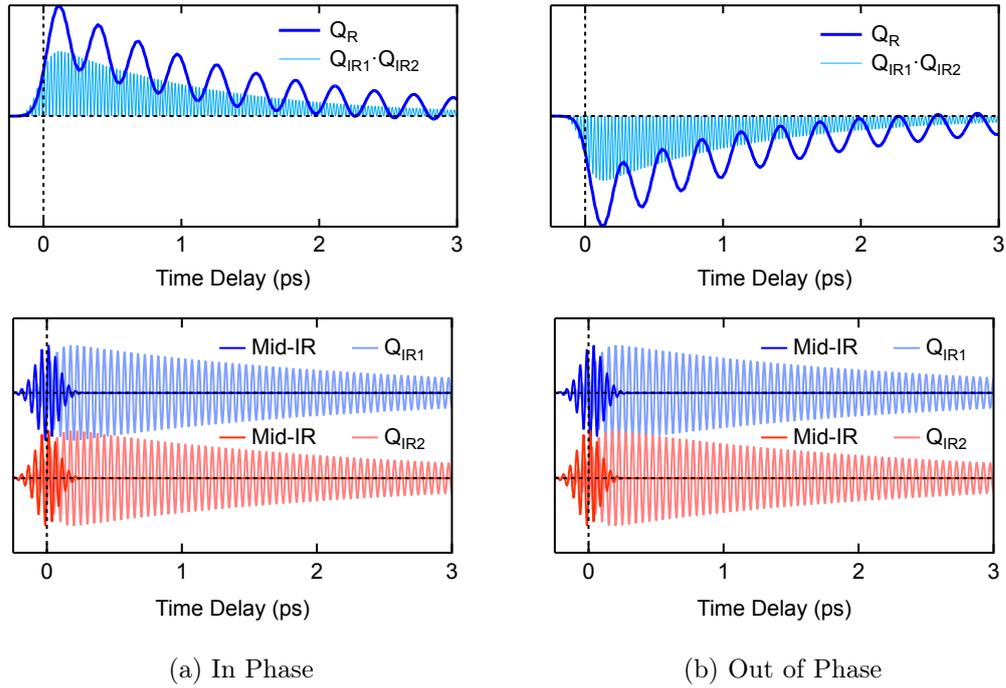
Figure 1.1.2: Cubic coupling of two directly driven infrared modes to a Raman mode exerts a directional force $F'(t) \sim \cos(\omega_{ir}t)\cos(\omega_{ir}t + \Delta\varphi)$ onto the Raman mode (light blue). (a) If the modes oscillate in-phase ($\Delta\varphi = 0$), minima and maxima of the oscillations coincide and the force is always positive. (b) Changing the relative phase $\Delta\varphi$ of the IR mode oscillations by π switches the sign of the force, allowing for a control of the direction of the lattice displacements.
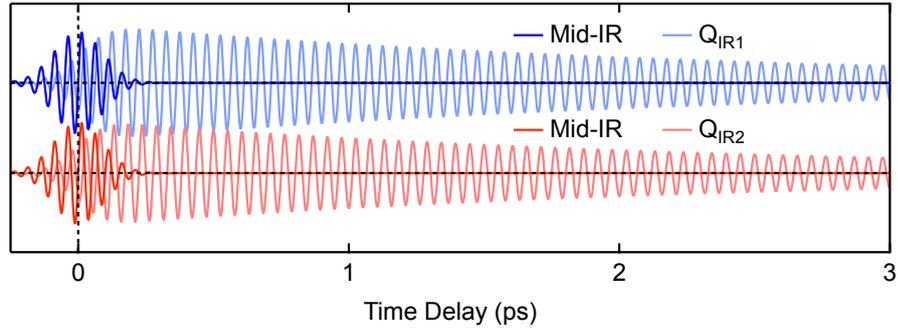
(a)
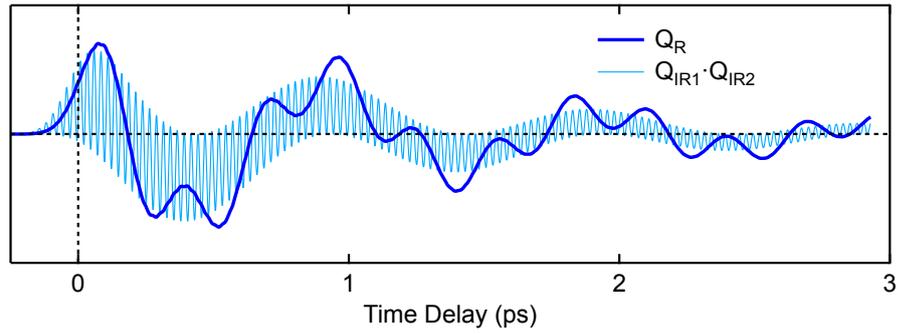
(b)

Figure 1.1.3: a) Cubic coupling of two directly driven infrared modes with frequencies of 20 THz and 19THz to a Raman mode Q_R. b) The force acting on the Raman mode oscillates at their difference frequency of $2\pi\Delta\omega = 1$THz. Changing the phase of the two infrared modes will only result in a phase change of the oscillatory force acting on the Raman mode. Note that the Raman mode will be driven resonantly, if the difference frequency between the two IR modes equals the Raman mode frequency. The force will only be directional, if one of the IR modes decays before it switches sign, that is, if the decay time is smaller than the half period of the difference frequency.

1.1.3   Generation of coherent phonons

Alongside the lattice displacement, the coupled Equations (1.1.1) and (1.1.2) predict that all of the displaced modes, which have a long enough eigenperiod, will exhibit coherent oscillations about the displaced atomic positions. Specifically, this happens only for those modes with eigenperiod T_{R} long compared to the rise time of the directional force, or, equivalently, compared to the width of the mid-infrared pulse envelope Δ_{ir} driving the odd mode Q_{ir}. The precise oscillation amplitude will further depend on the anharmonic coupling constant. Further, unlike for the displacive response discussed above, these oscillations relax over a timescale that is determined by the lifetime of the Raman mode $\tau_{\mathrm{R}} = 1/\gamma_{\mathrm{R}}$, which may be far longer than $\tau_{\mathrm{ir}}/2$ (see blue and red oscillations in Figure 1.1.1).

The phase of the oscillations with respect to the peak of the exciting laser pulse may be zero or finite, depending on whether the process is in the impulsive or displacive limit. In the impulsive limit, ($T_{\mathrm{R}} \gg \Delta_{\mathrm{ir}}, \tau_{\mathrm{ir}}$ and $\omega_{\mathrm{ir}} \gg \omega_{\mathrm{R}}$) the infrared-active mode decays back to its ground state before the Raman mode has started oscillating. Hence, Raman oscillations take place about the equilibrium lattice coordinates, with $Q_{\mathrm{R}} \sim \sin\left(\omega_{\mathrm{R}}t\right)$. In the displacive limit, ($T_{\mathrm{R}} \gg \Delta_{\mathrm{ir}}$, $T_{\mathrm{R}} \ll \tau_{\mathrm{ir}}$ and $\omega_{\mathrm{ir}} \gg \omega_{\mathrm{R}}$) the IR mode and the displacive response decay slowly, and the Raman excitation occurs about the shifted atomic positions. The force $F(t)$ acting on the Raman mode can be approximated by a step function and $Q_{\mathrm{R}}(t) \sim (1 - \cos\left(\omega_{\mathrm{R}}t\right))$. In most cases, the oscillations will have a phase that is neither sine nor cosine, or the phase of the Raman mode may change over time.

In the following, the process of conventional and ionic stimulated Raman scattering will be compared. For conventional electronic stimulated Raman scattering, the equation of motion (Eq. (1.1.2)) has the same structure and the same limits discussed above can be derived [42, 43]. Specifically, in an insulating material, the force acting on the Raman mode is proportional to $|E(t)|^2$, with $E(t)$ being the incident electric field:

$$F\left(t\right) = \left(\frac{\partial \chi}{\partial Q_{\mathrm{R}}}\right) |E(t)|^2 .$$

In transparent materials, coherent phonons are driven through a coupling to virtual electronic states that are excited by the light pulse and very short lived, leading to an impulsive driving force. Raman scattering with visible light in opaque materials can lead to a lattice displacement. Here, real electronic states are excited that modify the lattice potentials of certain phonon modes, displacing the lattice. The physical process is however fundamentally different, as in conventional stimulated Raman scattering the driving force derives from electronic transitions [44]. On the contrary, in ionic stimulated Raman scattering the driving force solely depends on lattice variables. As a consequence, the excitation process is most sensitive to phase transitions that affect the lattice. Atomic motions along Raman coordinates modify the refractive index of a material and can be detected by tracking changes in the reflectivity of 800nm probe pulses in a pump probe measurement. The source term relevant for this process is given by the polarization $P(t)$, which is induced by the electric field of the probe pulse $E(t)$ and modulated by the coherent phonon oscillation given by $Q_\mathrm{R}(t)$

$$P(t) \sim \frac{\partial \chi}{\partial Q_\mathrm{R}} E(t) \cdot Q_R(t).$$

1.2 Quartic order coupling

Although third order coupling usually dominates the nonlinear lattice dynamics, fourth order coupling can become sizable for higher driving fields and is the leading coupling term if third order coupling is forbidden by symmetry. According to the general Hamiltonian of nonlinear phononics (Eq. 1.0.1), fourth order coupling is captured by

$$H = \sum_{\mathbf{q}} \left(a_{22} Q_{\mathbf{0},\mathrm{ir}}^2 Q_{\mathbf{q},\mathrm{j}}^2 + a_{13} Q_{\mathbf{0},\mathrm{ir}} Q_{\mathbf{q},\mathrm{j}}^3 + a_{31} Q_{\mathbf{0},\mathrm{ir}}^3 Q_{\mathbf{q},\mathrm{j}} \right) + \sum_{\mathbf{q}} a_{04} Q_{\mathbf{q},\mathrm{j}}^4 + a_{40} Q_{\mathbf{0},\mathrm{ir}}^4,$$

where the last two terms are the fourth order corrections to the harmonic potential of the IR mode and the coupled mode. For centrosymmetric materials, the second two terms in the sum are only allowed by symmetry, if $Q_{\mathbf{q},\mathrm{j}}$ is an odd mode (infrared-active). As the force acting on $Q_{\mathbf{q},\mathrm{j}}$ is either linear or cubic in $Q_{\mathbf{0},\mathrm{ir}}$, it has no impulsive component. While atomic vibrations can be induced through decay processes, the lattice structure is not modified.

For the controlled modification of crystal structures with light, the first term $a_{22} Q_{\mathbf{0},\mathrm{ir}}^2 Q_{\mathbf{q},\mathrm{j}}^2$ shows more interesting effects. As opposed to cubic coupling, where the symmetry of coupled phonon modes is constrained to modes of symmetries that belong to the product group of the IR mode with itself, this requirement is always met in fourth order coupling. The totally symmetric irreducible representation A_g is part of the product of any irreducible representation with itself so that $I\left(Q_{\mathrm{j}}\right) \otimes I\left(Q_{\mathrm{j}}\right) \subseteq I\left(Q_{\mathrm{ir}}\right) \otimes I\left(Q_{\mathrm{ir}}\right)$ is true for modes of any symmetry. Furthermore, coupling is not constrained to optical modes, as momentum conservation only requires the generation of pairs of phonons with opposite wavevectors: $\mathbf{q_1} = -\mathbf{q_2}$. Thus, even acoustic modes can couple to the directly driven infrared mode. The lattice Hamiltonian of fourth order coupling to a phonon mode of wavevector $\mathbf{q}$ is given by

$$H_{\mathbf{q}} = \frac{1}{2}\left(P_{\mathrm{ir}}^2 + \omega_{\mathrm{ir}}^2 Q_{\mathrm{ir}}^2\right) + \frac{1}{2}\left(P_{\mathbf{q},\mathrm{j}}^2 + \omega_{\mathbf{q},\mathrm{j}}^2 Q_{\mathbf{q},\mathrm{j}}^2\right) - a_{22} Q_{\mathrm{ir}}^2 Q_{\mathbf{q},\mathrm{j}}^2. \qquad (1.2.1)$$

(a) Cubic Coupling
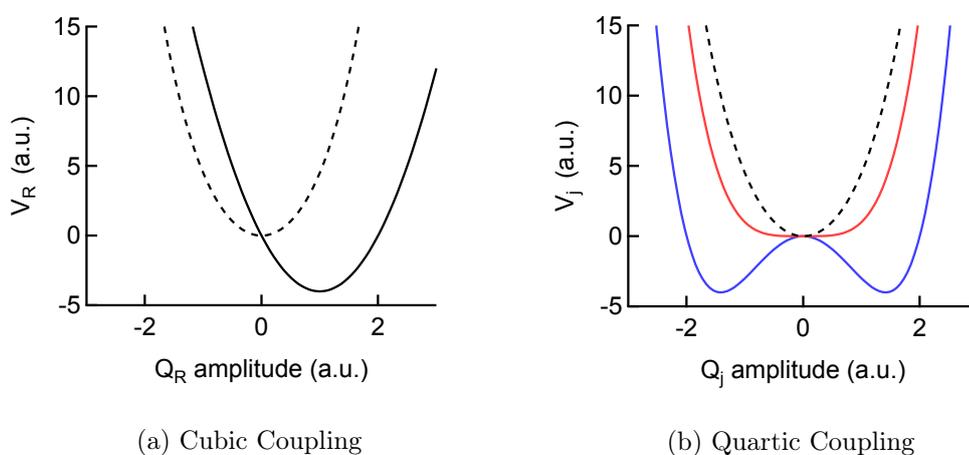
(b) Quartic Coupling

Figure 1.2.1: Comparison of cubic and quartic coupling. Dashed lines: Potential energy of a mode Q as a function of mode amplitude in equilibrium. (a) A static distortion Q_{ir}^* shifts the potential of all Raman modes Q_R that are coupled through cubic $Q_{ir}^2 Q_R$ coupling (solid line), displacing the equilibrium position towards a new minimum. (b) Due to quartic $Q_{ir}^2 Q_j^2$ coupling, the energy potential of a coupled mode Q_j is deformed symmetrically upon static distortion Q_{ir}^*. The frequency of the mode first softens (red solid line) until it is destabilized, which manifests in a double well potential (blue solid line). The image in panel (a) is taken from [33].

1.2.1 Modification of the crystal structure

Following this Hamiltonian, small amplitude IR mode excitations would simply renormalize the frequency of a second mode $Q_{\mathbf{q},\mathrm{j}}$. This can directly be deduced from the equation of motion, where the driving force is given by the coupling term $a_{22}Q_{\mathrm{ir}}^2 Q_{\mathbf{q},\mathrm{j}}$, which is linear in $Q_{\mathbf{q},\mathrm{j}}$:

$$\ddot{Q}_{\mathbf{q},\mathrm{j}} + 2\gamma_{\mathbf{q},\mathrm{j}}\dot{Q}_{\mathbf{q},\mathrm{j}} + \omega_{\mathbf{q},\mathrm{j}}^2 Q_{\mathbf{q},\mathrm{j}} = 2a_{22}Q_{\mathrm{ir}}^2 Q_{\mathbf{q},\mathrm{j}}.$$

Upon displacement of the infrared mode Q_{ir}, the anharmonically coupled mode experiences a renormalization of its frequency $\omega'_{\mathbf{q},\mathrm{j}} = \sqrt{\omega_{\mathbf{q},\mathrm{j}}^2 - 2a_{22}Q_{\mathrm{ir}}^2}$. However, above a threshold-amplitude $Q_{\mathrm{ir}}^{2*} = \omega_{\mathbf{q},\mathrm{j}}^2/2a_{22}$, the frequency of the second mode Q_{j} becomes imaginary[41] and the lattice becomes unstable. Importantly, such instability can take place in two directions, depending on the random instantaneous state of the system, given by the mode amplitude Q_{j} and its velocity dQ_{j}/dt, which manifests in a change from a parabolic to a double well energy potential as shown in Figure 1.2.1. This poses a certain difficulty for pump-probe experiments, in which the usual procedure is to repeat an experiment and average over hundreds or thousands of interactions. In order to measure these lattice deformations, which happen randomly in one or the other direction, the deviation from the average has to be determined by measuring the signal from each individual shot and comparing it to the average of many shots. Note that the perfectly symmetric potential is an ideal case and one minimum may well be preferred due to internal degrees of freedom such as inhomogeneities or external influences. For a system with large fourth order coupling it might be possible to control the lattice displacements simply by applying an external field which breaks the symmetry between the two energy potential minima. Controlling the direction of the lattice displacements would enable switching forth and back between states, which is necessary for applications as explained in the introduction.

1.2.2 Generation of squeezed phonon fields

As discussed above, for infrared mode excitations below a threshold amplitude, the impulsive force acting on the coupled mode

$$F = 2a_{22}Q_{\text{ir}}^2 Q_{\mathbf{q},\text{j}}$$

does not destabilize the lattice. Instead, it causes a sudden change in the frequency of the coupled mode Q_{j}. This effect is known as phonon squeezing and has been observed following excitation with electric fields in the visible range, in which the acting force has the same structure [45, 46, 47]:

$$F = \frac{1}{2}\left(\frac{\partial^2 \chi}{\partial Q_{\mathbf{q},\text{j}}^2}\right)|E(t)|^2 Q_{\mathbf{q},\text{j}}.$$

While this excitation does not change the expectation value of the equilibrium position at any time ($\langle Q_{\text{j}} \rangle = 0$), it does affect its variance $\sigma_{\mathbf{q},\text{j}}^2 = \langle (Q_{\mathbf{q},\text{j}} - \langle Q_{\mathbf{q},\text{j}} \rangle)^2 \rangle = \langle Q_{\mathbf{q},\text{j}}^2 \rangle$, a measure of the average distance of the atoms away from their equilibrium positions. The equation of motion for the variance can be derived from the Hamiltonian for fourth order coupling (see appendix A.4) as

$$\frac{d^3\langle Q_{\mathbf{q},\text{j}}^2\rangle}{dt^3} + 4\left[\omega_{\mathbf{q},\text{j}}^2 - a_{22}Q_{\text{ir}}^2(t)\right]\frac{d\langle Q_{\mathbf{q},\text{j}}^2\rangle}{dt} = 2\langle Q_{\mathbf{q},\text{j}}^2\rangle\left(a_{22}\frac{d}{dt}Q_{\text{ir}}^2\right). \quad (1.2.2)$$

For the special case of a light pulse with a pulse duration Δ much shorter than the phonon mode period $\triangle \ll T_{\mathbf{q},\text{j}}$, the pulse can be approximated as a delta function. The solution to equation (1.2.2) is then[45]:

$$\langle Q_{\mathbf{q},\text{j}}^2(t)\rangle \approx \langle Q_{\mathbf{q},\text{j}}^2(0)\rangle\left(1 + A\sin\left(2\omega_{\mathbf{q},\text{j}}t\right)\right).$$

Note first that while the impulsive excitation of coherent phonons through third order coupling results in oscillations at discrete frequencies given by the optical phonon modes at $\mathbf{q} = 0$, squeezed phonon fields generated through fourth order coupling consist of a continuum of phonon modes at different $\mathbf{q}$ vectors and frequencies $\omega_{\mathbf{q},\text{j}}$. The oscillations from squeezed phonons will
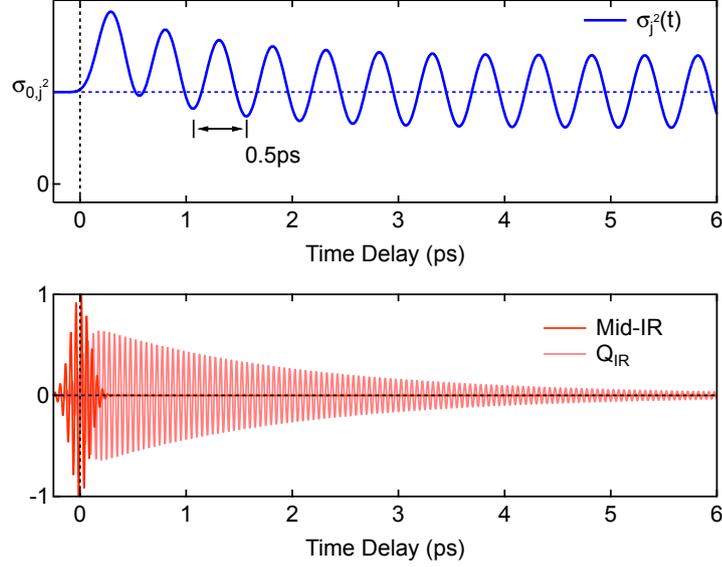
Figure 1.2.2: Within quartic coupling, the excitation of infrared mode oscillations to amplitudes below a threshold Q_{ir}^{2*} does not involve lattice displacements or the excitation of coherent phonons. Instead, the variance $\sigma_j^2 = \langle Q_j^2 \rangle$ of a coupled mode is driven to oscillations (blue). According to Eq. 1.2.2, the variance oscillates at twice the frequency of the coupled mode (here $2\pi\omega_j = 1\,\mathrm{THz}$) and can temporarily be reduced below its equilibrium value $\sigma_{0,j}^2 = \sigma_j^2(0)$ during a cycle.

thus have a spectral content, which is determined by the phonon density of states. The squeezed phonon field interacts with the polarization $P(t)$ induced by the electric field of a probe pulse $E(t)$ according to:

$$P\left(t\right) \sim \frac{\partial^2 \chi}{\partial Q_{\mathbf{q},j}^2} E(t) \cdot \left\langle Q_{\mathbf{q},j}^2\left(t\right) \right\rangle.$$

Hence, changes in the variance directly modify the refractive index of the material and can be detected by tracking changes in the reflectivity of 800nm probe pulses in a pump probe measurement. Note that the variance oscillates with a frequency twice as large as the phonon mode frequency $\omega_{\mathbf{q},j}$ coupled to the infrared mode as shown in Figure 1.2.2.

1.3 Outlook

As set forth in the introduction, the application for photonic devices requires the switching between different phases of matter, which can only be achieved if the direction of the light induced lattice displacements can be controlled. In the previous sections, two approaches for such control have been presented.

The first approach involves vibrational excitation of two phonon modes with individual light pulses. Varying the arrival time delay between these pulses changes the relative phases of the two phonon modes, which gives control over the direction of the displacement along the coupled phonon mode as presented in section 1.1.2.

A second approach is given in section 1.2. For materials, which exhibit large quartic coupling, the harmonic energy potential of a coupled mode can be transformed into a symmetric double well potential. The mode will be destabilized with the direction of the lattice displacement depending on the random instantaneous state of the system. Additional, external stimulations might break this symmetry and select the direction of the lattice displacements. These two approaches are abstract ideas that could be applied and tested in future experiments.

This section introduces a specific concept for switching the polarization state of ferroelectrics [48]. Density Functional Theory calculations predict strong coupling between the highest frequency infrared-active mode Q_{ir} to the ferroelectric soft mode Q_{p} in a number of ferroelectrics. This coupling can be intuitively understood on the example of LiNbO$_3$, which, above the Curie temperature, crystallizes in the rhombohedral $R\bar{3}c$ space group, similar to the structure of La$_{0.7}$Sr$_{0.3}$MnO$_3$ shown in Figure 2.1.5. The transition into the ferroelectric phase involves a polar distortion along the pseudocubic (111) direction and the loss of inversion symmetry [49]. Vibrations of the highest frequency infrared-active mode Q_{ir}, which is composed of Nb-O stretching motions along the same direction, periodically modify the Li-O bond distances and thus the energy potential of the polar mode. Note that as ferroelectrics are non-centrosymmetric materials, phonon modes cannot be classified as either infrared or Raman modes and the simplifications derived

in the previous sections do not hold. The coupling between the ferroelectric soft mode Q_{p} and the infrared-active mode Q_{ir} is dominated by the two terms

$$aQ_{\mathrm{ir}}^2 Q_{\mathrm{p}} + bQ_{\mathrm{ir}}^3 Q_{\mathrm{p}}.$$

In line with the discussion of cubic anharmonicities, coupling is only allowed to $\mathbf{q} = 0$ modes, which is why the wavevectors have been omitted. In the following, the effect of these two coupling terms will be discussed.

Cubic coupling $\mathbf{aQ_{ir}^2 Q_p}$

As discussed in section 1.1, the force applied on the ferroelectric mode by the oscillatory motions of the infrared active mode through cubic coupling is rectified, leading to a directional displacement of the atoms. The direction of this displacement is given by the coupling constant a and cannot be controlled as explained above. The DFT calculations of Ref. [48] revealed however, that the sign of this coupling constant depends on the initial polarization state of the ferroelectric and is such that the atoms are always displaced in the direction that switches the polarization.
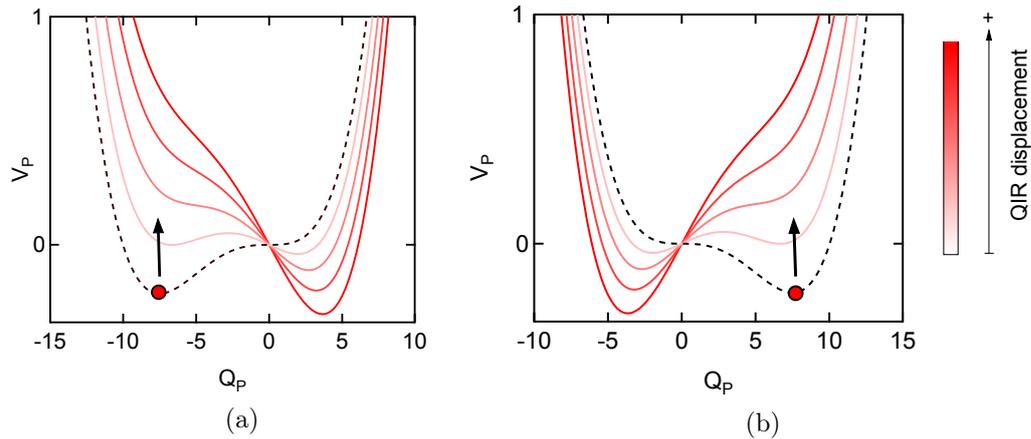

Figure 1.3.1: (a) and (b) Static displacements of the infrared-active mode Q_{ir} destabilize the equilibrium energy minimum (black dashed line) such that a force is exerted on the atoms towards a new energy minimum corresponding to the opposite polarization state.

Panels a and b of Figure 1.3.1 show the modification of the equilibrium potential (dashed lines) due to a static displacement of the infrared-active mode Q_{ir} for the two different initial polarization states, respectively. The modification of the energy potential destabilizes the initial energy minimum and favors atomic motions towards the other polarization state. Note that this switching mechanism requires the directional force, which is exerted on the atoms, to be maintained long enough for the system to relax in the new minimum position. This requirement might intrinsically be fulfilled, if the lifetime of the excited infrared-active phonon mode is long enough. Otherwise, the phonon mode has to be driven either repeatedly with multiple pulses or continuously with one pulse of picosecond time duration.

Quartic coupling $bQ_{ir}^3 Q_p$

According to the second, quartic coupling term $Q_{ir}^3 Q_p$, the energy potential V_p of the coupled mode Q_p is modified periodically at the fundamental and third harmonic frequency of the driven mode Q_{ir}. As opposed to the cubic anharmonicity discussed above, the coupling is uneven in Q_{ir} and there is no rectification of the force applied on the ferroelectric mode. Despite the lack of changes of the energy potential on average, the driving *dynamically* stabilizes the $Q_p = 0$ position of the potential.

This effect will in the following be illustrated for the a simplified, symmetric potential V_p. The periodic modulation by quartic coupling is shown in Figure 1.3.2 for different Q_{ir} amplitudes. For continuous wave excitation of the high frequency mode Q_{ir}, the coupled mode shifts from its initial value of $Q_p = +1$ or -1 towards 0 such that the zero polarization state is stabilized. This average force is the result of the asymmetry of the energy potential in the vicinity of the initial state, i.e. one of the two energy minima corresponding to the two polarization states.

For a pulsed excitation, the average force acting on Q_p, which is directed towards the center point of the energy potential, decays within one third of the decay time of the driven mode Q_{ir} and can transfer momentum on the coordinate Q_p, which results in a change of the polarization state.
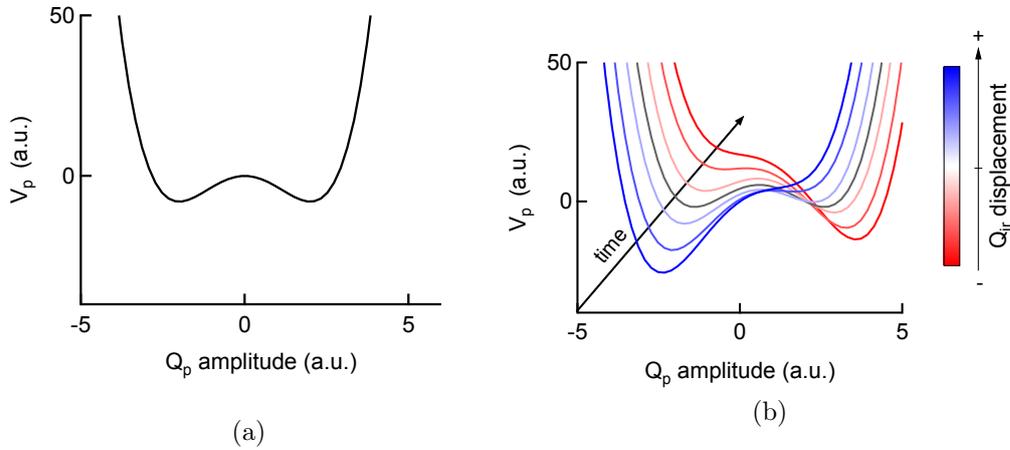
Figure 1.3.2: (a) The energy potential V_p of the ferroelectric mode Q_p has two minima (here shown simplified as symmetric double well potential). The two minima correspond to the two polarization directions. (b) The excitation of the highest frequency infrared-active mode Q_ir modifies the energy potential of the ferroelectric mode according to $Q_\mathrm{ir}^3 Q_\mathrm{p}$. As the term is odd in Q_ir^3, the energy potential is modified differently for positive (blue) and negative (red) Q_ir amplitudes.

The numerical solution of the coupled equations of motion for pulsed excitation is shown in Figure 1.3.3, considering only quartic coupling in the potential shown in Figure 1.3.2. Importantly, the sign of the average force shown in light blue depends on the initial state and always points towards the other potential minima. For high enough driving fields, switching between polarization states on picosecond timescales might be possible using multiple light pulses. Whether or not the coupling is strong enough to allow for switching of the polarization has to be experimentally investigated in future studies.
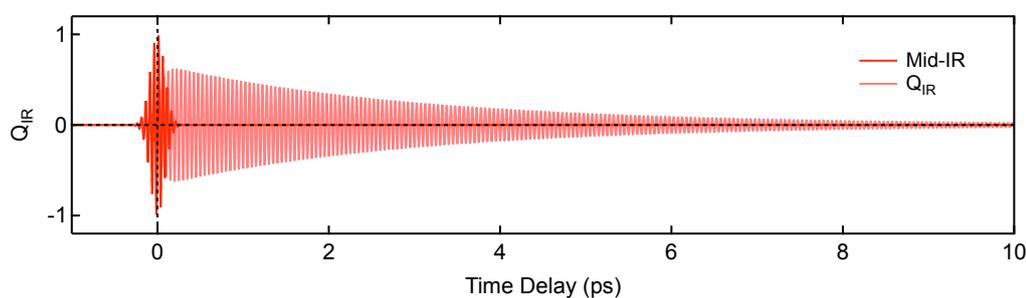
(a)
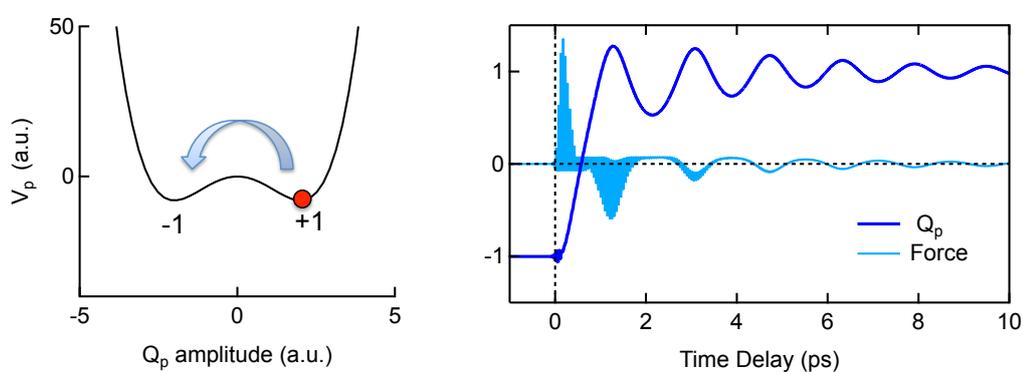
(b) In Phase
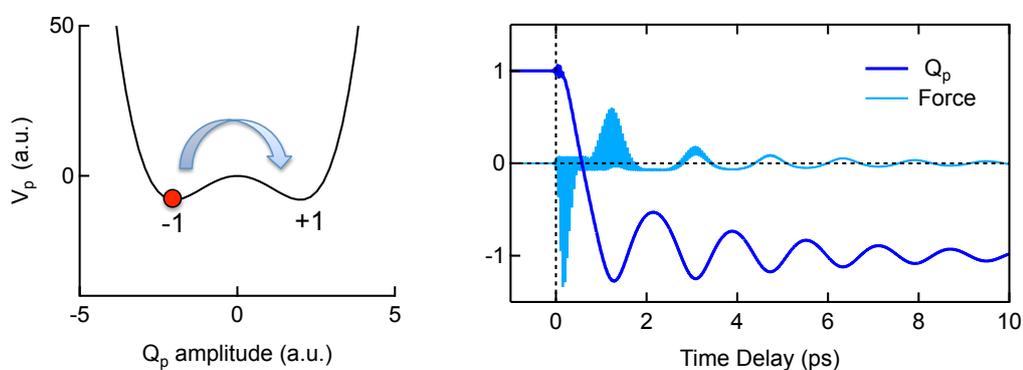
(c) Out of Phase

Figure 1.3.3: (a) Shown are the oscillatory motions of the resonantly driven infrared-active mode Q_{ir} (light red). (b), (c) Due to the asymmetric energy potential in the vicinity of the two minima denoted by -1 and +1, the periodic modulation of the lattice potential from quartic coupling results in an *average* force $F \sim -dV/dt$ (light blue) different from zero. This force depends on the initial state and always acts towards the other minimum. For high enough Q_{A1} amplitudes, the polarization switches (blue).

Chapter 2

Structural control of Manganites

This chapter covers experiments on the control of collective electronic and magnetic properties of manganites by resonant lattice excitation. In the first section, the first direct observation of nonlinear lattice dynamics is discussed, followed by a quantitative determination of the lattice displacements by ultrafast x-ray diffraction. This study shows how Raman rotational and Jahn-Teller degrees of freedom can be controlled by direct lattice excitation. In the next sections, the coupling of these distortions to the electronic and spin degrees of freedom is explained. Previous measurements of ultrafast insulator to metal transitions and melting of orbital and magnetic order in manganites are presented and discussed in the framework of nonlinear phononics.

2.1 Nonlinear lattice dynamics in $La_{0.7}Sr_{0.3}MnO_3$

The first direct observation of nonlinear lattice dynamics following resonant excitation of infrared-active vibrations was reported in 2011 by Först et al. [22]. At that point, selective excitation of infrared-active lattice vibrations has already been proven to be a valuable tool for the control of macroscopic properties of solids. Insulator-metal transitions, melting of magnetic order and even the emergence of superconducting order have been shown to follow low energy lattice excitation. However, the issue of how lattice vibrations with zero average displacement could drive such dramatic phase transitions has not been solved. Parts of this chapter are taken from Ref. [26].

35
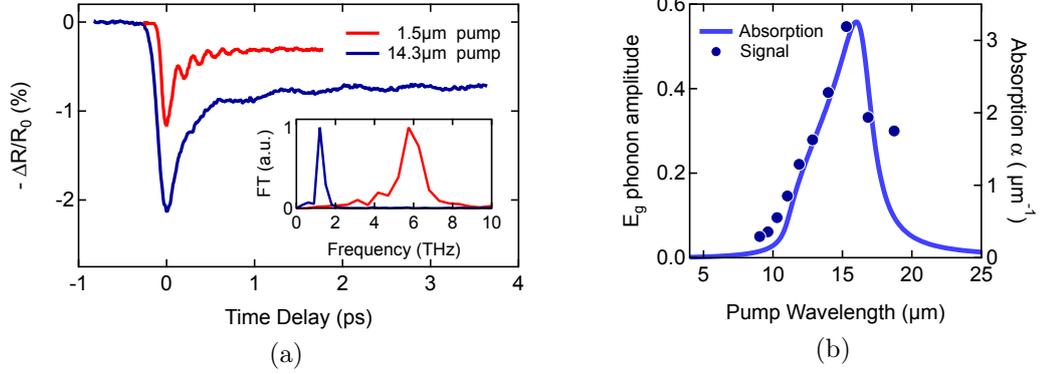
Figure 2.1.1: (a) Time-resolved reflectivity changes of $La_{0.7}Sr_{0.3}MnO_3$ at 800 nm following near-infrared excitation at 1.5 μm (red) and resonant excitation of the E_u phonon mode at 14.3 μm (dark blue). The Fourier transformation of the oscillatory signal contributions are shown in the inset. (b) The coherent E_g mode amplitude at 1.2 THz is shown for excitations with pump pulses of different wavelengths. The light blue curve is the wavelength-dependent absorption of $La_{0.7}Sr_{0.3}MnO_3$ due to the E_u phonon mode. The images are adapted from [22].

2.1.1 Generation of coherent phonons

In this experiment, the manganite $La_{0.7}Sr_{0.3}MnO_3$ ($LSMO_{0.3}$) was excited with mid-infrared pulses resonant with an infrared-active Mn-O stretching motion of E_u symmetry. Following the excitation, time-resolved changes in the reflectivity were measured with 800 nm pulses in a pump probe setup. The observed signal showed oscillatory components that could be attributed to an E_g symmetry Raman mode at 1.2 THz. Measurements with different pump wavelengths revealed that the amplitude of these coherent oscillations closely follows the resonance curve of the absorption of $LSMO_{0.3}$ due to the infrared-active E_u mode and peaks at the resonance frequency of the infrared-active mode at 14.3 μm as shown in Figure 2.1.1 (adapted from [22]). Thus, anharmonic coupling between the oscillatory motion of an infrared-active phonon mode to a Raman mode has been demonstrated. The observation can be explained in the framework of nonlinear phononics as third order coupling of the excited E_u mode to the E_g mode. The studied material, $La_{0.7}Sr_{0.3}MnO_3$, crystallizes in a centrosymmetric structure of the

point group $R\bar{3}c$ or D_{3d}^6, for which the E_g irreducible representation is part of the direct product of the E_u mode with itself ($E_g \subset E_u \otimes E_u$). The coupling is thus symmetry allowed. While a lattice displacement is expected for all coupled modes, the impulsive excitation to coherent phonon oscillations only occurs for modes with a period T long compared to the driving pulse duration Δ. The E_g mode period was about 5 times larger than the duration of the pump pulses used in the experiment, allowing for an impulsive excitation mechanism. In summary, the frequency and the symmetry of coherent Raman oscillations impulsively driven by ionic stimulated Raman scattering could be extracted from these optical probe experiments. However, the key phenomenon of a displacive force that drives the crystal structure into a new transient structure could not be proven.

2.1.2   Modification of the crystal structure

From optical data alone, it is not possible to uniquely identify, whether the oscillations occur around the atomic positions of the ground state or a displaced structure. Following the model of nonlinear phononics, the phase of the oscillations can however serve as an indicator. In the impulsive limit, in which the atomic displacements decay fast compared to the oscillation period, the functional form of the oscillations is $Q_R \sim \sin(\omega t)$. In the opposite limit of a long lived force displacing the atoms, the oscillations are given by $Q_R \sim (1 - \cos(\omega t))$ as discussed in section 1.1.3. Due to the symmetry of the E_g mode, the change in reflectivity from the atomic motions has opposite signs for orthogonal probe pulse polarizations. Assuming a similar electronic contribution for the two polarizations, the signal from the atomic motions can be extracted by subtracting the measured signals for s- and p-polarized probe pulses. The data is shown in Figure 2.1.2 together with a fit function assuming a displacive limit. While no quantitative information can be obtained from this procedure, the close agreement between fit and data supports the picture of excited lattice vibrations that oscillate around a transient structure with a long-lived displacive component.

(a) (b)
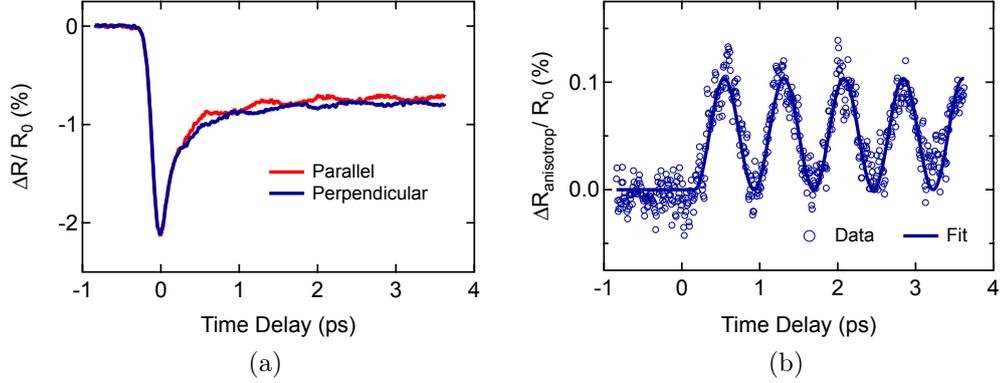
Figure 2.1.2: Time resolved changes in the reflectivity following resonant excitation of the E_u mode in $La_{0.7}Sr_{0.3}MnO_3$ at 14.3 μm [26]. (a) While the electronic contribution to the signal is independent of the 800nm polarization, the lattice contribution changes sign due to the symmetry of the E_g mode. (b) By subtracting the signal obtained from the orthogonal probe polarizations, the contribution from the lattice dynamics can be extracted. A fit assuming a displacive excitation of the E_g mode is shown as solid blue line. The images are adapted from [26].

Ultrafast x-ray diffraction

In order to test this hypothesis and to determine the absolute atomic motions, we combined vibrational pump with diffraction using femtosecond hard x-ray pulses from the Linac Coherent Light Source (LCLS) free electron laser [26]. Atomic motions along phonon coordinates result in a change of the structure factors of Bragg peaks and modulate the diffracted intensity. As shown in Figure 2.1.3, the E_g Raman mode corresponds to counter-directional rotations of adjacent MnO_6 octahedra around an axis (red arrow) perpendicular to the rhombohedral and pseudo-cubic $(111)_{pc,r}$ direction (blue arrow). The direction of this rotational axis in the plane can be defined by the relative amplitudes of the two degenerate E_g modes. Their motions only involve displacements of oxygen atoms, which have a much smaller scattering efficiency than the larger manganese or Lanthanum atoms. Thus, Bragg peaks with scattering contributions from the Mn and La/Sr sub-lattices show very small relative changes in their scattering intensity.

(a)   (b)
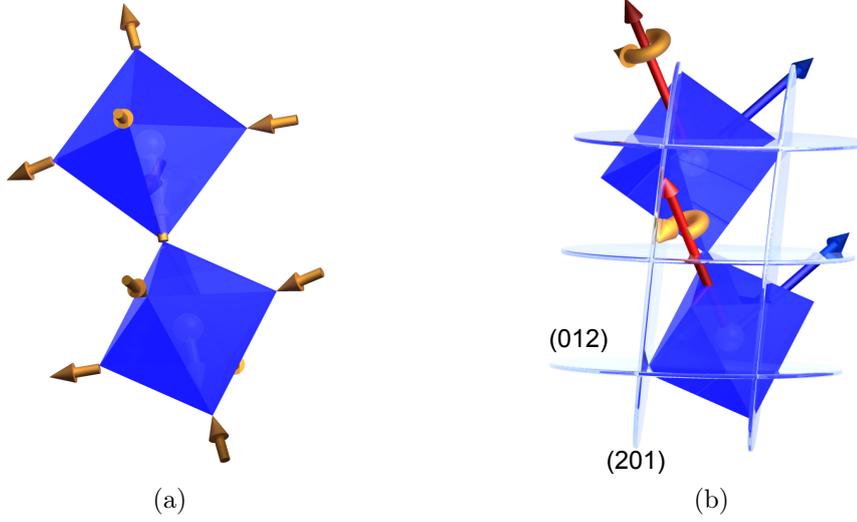
Figure 2.1.3: (a) The E_u mode at 14.3 μm consists of Mn-O stretching motions with a polarization vector in the plane perpendicular to the rhombohedral and pseudo-cubic $(111)_{pc,r}$ direction (blue arrow). (b) The E_g Raman mode corresponds to counter-directional rotations of adjacent MnO_6 octahedra around an axis (red arrow) lying in the same plane. The direction of this rotational axis in the plane can be defined by the relative amplitudes of the two degenerate E_g modes. The light blue planes show the (012) and (201) diffraction planes. The images are taken from [26].

The change in diffraction intensity $\triangle I_{hkl}/I_{hkl}$ of Bragg peaks due to atomic motions can be calculated by comparing their structure factors in the equilibrium $F_{hkl}(\boldsymbol{r})$ and displaced $F_{hkl}(\boldsymbol{r}')$ structure:

$$\frac{\triangle I_{hkl}}{I_{hkl}} = \frac{|F_{hkl}(\boldsymbol{r})|^2 - |F_{hkl}(\boldsymbol{r}')|^2}{|F_{hkl}(\boldsymbol{r})|^2}.$$

In $La_{0.7}Sr_{0.3}MnO_3$, the (201) family of reflections is forbidden for the Mn and La/Sr sub-lattices, making them solely sensitive to motions of oxygen atoms. As a consequence, they are especially sensitive to motions along the E_g coordinate but also very weak and the only femtosecond x-ray source with sufficient flux to observe them is a free electron laser.
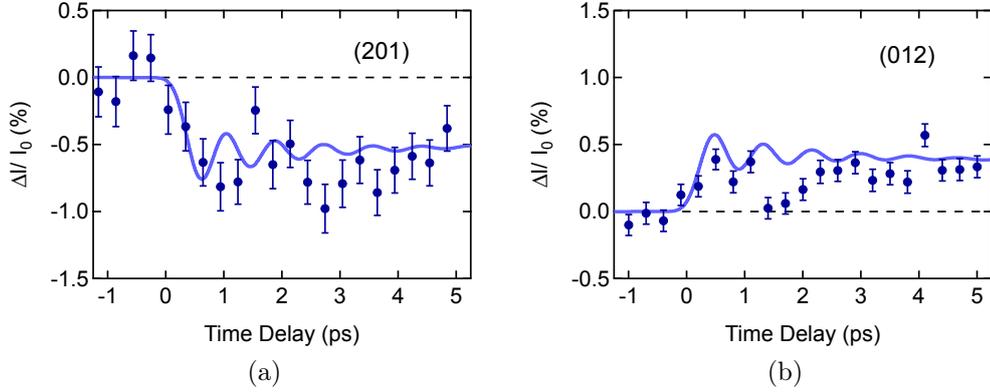
Figure 2.1.4: Time-resolved changes in scattered intensity from the (201) and (012) lattice reflections in $La_{0.7}Sr_{0.3}MnO_3$, following resonant excitation of the Mn–O stretching vibration [26]. The functional form and relative amplitudes of the two fits are given by the solution Q_R of the coupled differential equations and multiplied by the coefficients for the respective lattice reflections. The anharmonic coupling constant is the only parameter that has been varied to fit the calculations to the experimental data. The images are adapted from [26].

As mentioned above, the femtosecond x-ray diffraction experiments discussed here were performed at the X-ray Pump-Probe (XPP) beamline of the LCLS free electron laser [50]. The crystal was excited by 220 fs midinfrared pulses at 15 μm wavelength. The incident excitation fluence was 1.2 mJ/cm². 70 fs x-ray probe pulses were generated by the free electron laser. The experiment was carried out at a repetition rate of 120 Hz. A silicon (111) monochromator was used to select the 6 keV probe pulse energy. Non-coplanar time dependent diffraction from the (201) and (012) lattice reflections was measured at an incidence angle of 5°, chosen to match the x-ray penetration depth to that of the mid-infrared pump pulses. Shot-to-shot normalization to the x-ray pulse energy after the monochromator corrected the detected signals for intensity and wavelength fluctuations from the free electron laser. The time resolution of the experiment was 300 fs, as limited by the timing jitter between the mid-infrared and x-ray pulses. More details on the experimental setup and the measurement technique can be found in Appendix C.

The relative changes in scattered intensity of the (201) and (012) lattice reflections after resonant excitation of the Mn-O stretching vibration are shown in Figure 2.1.4. They show an intensity change in opposite directions at a timescale of 300 fs, limited by the time resolution of the experiment, followed by a long lived state. Best fits to the data with error functions yield relative intensity changes $\triangle I / I_0$ of $(0.28 \pm 0.02)\,\%$ and $(-0.66 \pm 0.05)\,\%$, respectively. To deduce the atomic displacement from the changes in scattered intensity, the orientation of the E_g rotation axis has to be calculated from the polarization of the directly excited E_u mode.

Analysis

The E_u mode is polarized in the plane perpendicular to the $(111)_{pc,r}$ threefold rotational axis and two orthonormal vectors in this plane can serve as a basis for the E_u mode. We define the vector $\vec{E}_{u1}$ to lie in the glide plane along the x-axis and a second orthogonal vector $\vec{E}_{u2}$ along the y-axis: $\vec{E}_{u1} = (1,0,0)$, $\vec{E}_{u2} = (0,1,0)$ (see Figure 2.1.5). There are two Raman tensors for the twofold degenerate E_g mode in the D_{3d}^6 point group:

$$
\chi_1 = \begin{pmatrix} c & 0 & 0 \\ 0 & -c & d \\ 0 & d & 0 \end{pmatrix}
$$

and

$$
\chi_2 = \begin{pmatrix} 0 & -c & -d \\ -c & 0 & 0 \\ -d & 0 & 0 \end{pmatrix}.
$$

Consider now an excitation of the E_u mode only along $\vec{E}_{u1}$. As this motion conserves the glide plane, the coupled rotational motion of the E_g mode must conserve the same symmetry. This is only true for rotations around an axis lying in the glide plane as well, i.e. the x-axis.

(a)

(b)
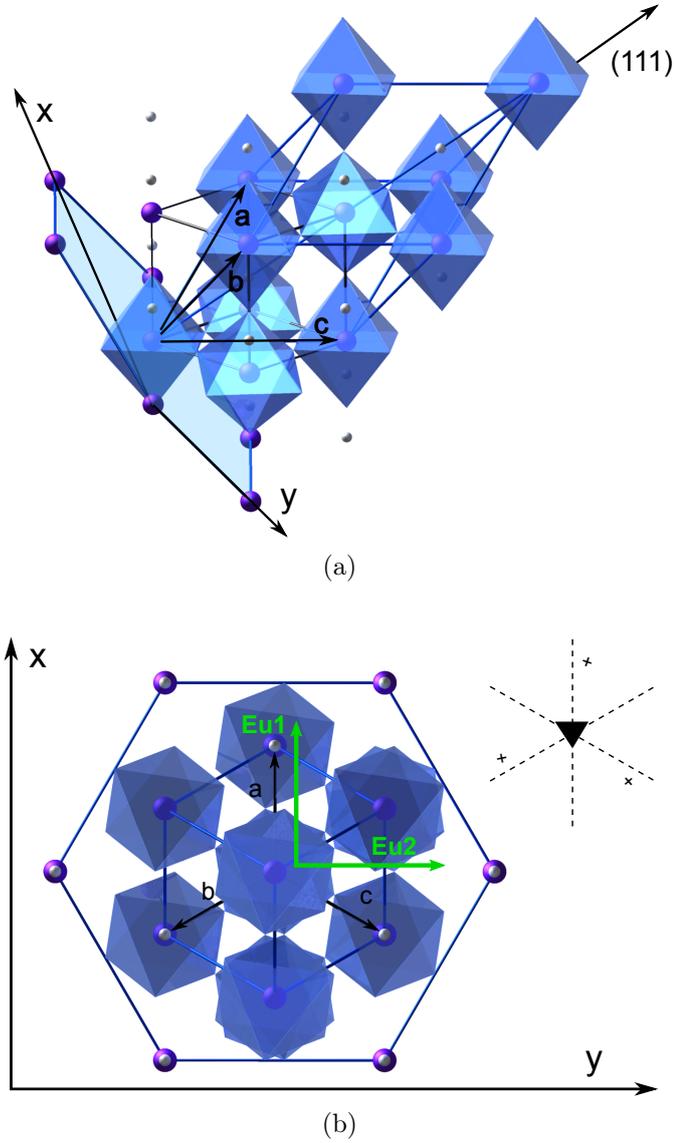
Figure 2.1.5: (a) La$_{0.7}$Sr$_{0.3}$MnO$_3$ crystallizes in a perovskite structure with a rhombohedral distortion. The pseudocubic unit cell of the parent perovskite structure is shown together with the hexagonal and rhombohedral unit cells of the LSMO structure. **a**, **b** and **c** denote the rhombohedral lattice vectors. (b) The degenerate E_u mode is polarized in the x-y plane perpendicular to the threefold rotational axis, which is the pseudocubic and rhombohedral $(111)_{pc,r}$ direction. We can thus define a basis for this mode by the two orthonormal vectors $\vec{E}_{u1}$ along x, lying in one of the glide planes and $\vec{E}_{u2}$ along y. The $\vec{E}_{u1}$ vector is collinear with the rhombohedral lattice vector **a** projected onto the x-y plane.

The product of $\vec{E}_{u1}$ with the two Raman tensors yields c for χ_1 and 0 for χ_2, respectively. The Raman tensor χ_1 must thus be associated with an E_g mode rotation around the x-axis and the χ_2 tensor with an orthogonal rotational axis. Using the ionic Raman tensors for the E_g mode of the D_{3d}^6 point group, the E_g mode can thus be written as:

$$\vec{E}_g = f_1 \begin{pmatrix} 1 \\ 0 \\ 0 \end{pmatrix} + f_2 \begin{pmatrix} 0 \\ 1 \\ 0 \end{pmatrix},$$

with

$$f_1 = \begin{pmatrix} E_{u1} \\ E_{u2} \\ 0 \end{pmatrix}^T \begin{pmatrix} c & 0 & 0 \\ 0 & -c & d \\ 0 & d & 0 \end{pmatrix} \begin{pmatrix} E_{u1} \\ E_{u2} \\ 0 \end{pmatrix},$$

$$f_2 = \begin{pmatrix} E_{u1} \\ E_{u2} \\ 0 \end{pmatrix}^T \begin{pmatrix} 0 & -c & -d \\ -c & 0 & 0 \\ -d & 0 & 0 \end{pmatrix} \begin{pmatrix} E_{u1} \\ E_{u2} \\ 0 \end{pmatrix}.$$

The components of the E_u mode E_{u1} and E_{u2} are given by the polarization of the electric pump field. Using the equations above, the angle between x-axis and the E_g mode rotational axis can be calculated to be 156° and 157° for the (201) and (012) Bragg reflections, respectively. With the knowledge of the orientation of the E_g mode, the structure factors of both diffraction peaks can be evaluated for the equilibrium and displaced crystal structure. For small deviations from the equilibrium structure, the change in diffraction intensity is linear with the atomic motions Q_R and a conversion factor can be calculated for both peaks. The relative change in scattering intensity $(\Delta I/I)/Q_R$ is -0.057 pm^{-1} and +0.043 pm^{-1} for the (201) and (012) Bragg peaks, respectively. By dividing the measured $\Delta I/I$ by the coefficients above and average over the results of the two peaks, we extract displacement along the phonon eigenvector of $Q_R = 0.09 pm$, which is equivalent to rotations of the oxygen octahedra of 0.035°.

With the knowledge of the mid-infrared pump pulse parameters and the amplitude of the excited E_g Raman mode, the numerical solution to the differential equations for cubic coupling (Eq. 1.1.1 and 1.1.2) can directly be compared with the experimental data. The model calculations are shown as solid line in Figure 2.1.4. The signal to noise ratio was too low to observe the coherent oscillations of the E_g phonon, previously measured in the optical experiment.

2.1.3 Summary

In summary, the femtosecond x-ray diffraction study demonstrates the displacive response of the $La_{0.7}Sr_{0.3}MnO_3$ crystal lattice to mid-infrared excitation. We found a conversion of the resonantly excited infrared-active E_u mode vibration into a directional rotation of the oxygen octahedra by 0.035° with no observed decay within 5ps. While the displacive response seems small, pump fluences up to 30 times higher than the 1.2 mJ/cm^2 used in this study can easily be achieved in labs, allowing for rotations of 1° or more.

2.2 Driving phase transitions

The study further shows how nonlinear phononics can be used to optically control rotations of the oxygen octahedra, which opens interesting possibilities for the control of collective electronic properties of manganites. In this section, first the electronic and magnetic properties of manganites are introduced, followed by a discussion of the effects of structural distortions accessible to optical control on these properties.

2.2.1 Collective electronic and magnetic properties

The electronic and magnetic properties of manganites are mainly determined by the crystal lattice distortions and the occupation of the manganese $3d$ orbitals. The octahedral coordination of the surrounding oxygen ligands results in a splitting of the five d orbitals into two e_g orbitals with higher energy, that are pointing towards the oxygen atoms and three remaining t_{2g} orbitals with lower energy. The undoped parent compound $LaMnO_3$ is an antiferromagnetic insulator and crystallizes in an orthorhombic structure, which can be derived from the cubic prevoskite structure by two lattice distortions. First, the oxygen octahedra are rotated, which decreases the Mn-O-Mn bond angle from the 180° of the cubic lattice. Further, the twofold degeneracy of the e_g orbitals is lifted by the Jahn-Teller effect, an elongation of the oxygen octahedra along one axis. In $LaMnO_3$, this Jahn-Teller distortion occurs in the a-b plane, alternately along the crystallographic a and b axis.

The manganese atoms are triply ionized in a $3d^4$ high-spin configuration ($S = 2$), in which all of the three t_{2g} orbitals and the energetically favored e_g orbital are half filled. The electrons occupying the t_{2g} orbitals are localized due to their small overlap with the surrounding oxygen p orbitals and can be treated as a core spin of $3/2$. While the half filling of the remaining e_g orbital normally points towards a metallic ground state, a strong onsite Coulomb repulsion prevents hopping between adjacent manganese sites. The competition between hopping H_t and localization due to Coulomb repulsion H_U can be qualitatively described by the Hubbard model, in which the electronic

Hamiltonian is given by $H = H_t + H_U$. The first term describes the kinetic energy

$$H_t = -t \sum_{\langle ij \rangle, \sigma} c_{i\sigma}^+ c_{j\sigma},$$

where $c_{i\sigma}^+$ and $c_{i\sigma}$ are the creation and annihilation operators for electrons at site i with spin σ and t is the effective hopping amplitude between neighboring manganese sites across the oxygen p orbital. This effective hopping amplitude can be expressed as $t = t_{pd}^2/\Delta_{ct}$, with t_{pd} denoting the hopping amplitude and Δ_{ct} the energy difference between the energetically lower oxygen p and the manganese d orbitals. The sum runs over neighboring sites only. The second term

$$H_U = U \sum_i n_{i\uparrow} n_{i\downarrow}$$

accounts for the Coulomb repulsion U of two electrons with opposite spins occupying the same e_g orbital, the operator $n_{i\sigma}$ counts the electrons at site i with spin σ. For $U \ll t$, the Hamiltonian describes a metallic state, in which the electrons of the e_g orbitals are delocalized. For the opposite case $U \gg t$, the electrons are localized and the material forms an insulating state with two bands separated by a band gap of $U - t$. Depending on the relative sizes of U and Δ_{ct}, the energetically lowest electronic excitation is either an electron transfer from one manganese d orbital to the next ($\Delta_{ct} > U$) or an electron transfer from the oxygen p orbital to the neighboring manganese d orbital ($\Delta_{ct} < U$). These different insulating states are called Mott-Hubbard and charge transfer insulators, respectively. In Mott-Hubbard insulators, the two separated bands originating from the manganese d orbitals are called lower and upper Hubbard bands.

The magnetic structure is determined by the orbital occupation and ordering of adjacent manganese ions. As mentioned above, the structural Jahn-Teller distortion lifts the degeneracy of the two e_g orbitals, lowering the energy of the orbital along the elongated bond direction. As a result, the orbital occupation and with it the magnetic structure are strongly coupled to these lattice distortions. In $LaMnO_3$, the MnO_6 octahedra are alter-
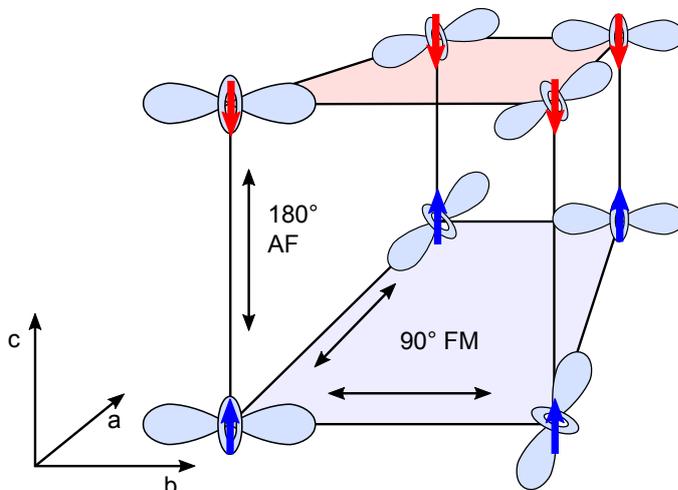
Figure 2.2.1: Magnetic and orbital structure of LaMnO$_3$. For simplicity, only the energetically lower eg orbitals are shown. According to the GKA rules, the 90° exchange of occupied orbitals in the a-b planes leads to a ferromagnetic (FM) alignment of the spins, while the 180° exchange results in antiferromagnetic (AF) order along the c axis.

nately elongated along the a and b crystallographic axis. As all manganese ions are triply ionized, all energetically lower e_g orbitals are filled. In the ab planes, the angle between neighboring e_g orbitals is 90°, along the c axis 180°. The magnetic structure of such ordering is described by the Goodenough-Kanamori-Anderson (GKA) rules, according to which 90° exchange between filled orbitals is weak and ferromagnetic and filled or empty orbitals with a 180° angle strong and antiferromagnetic [51]. The ordering of the Mn^{3+} spins is thus ferromagnetic in the planes and antiferromagnetic along the c-axis as shown in Figure 2.2.1.

Effect of structural distortions

The rotational distortion most strongly affects the hopping amplitude t, which can be understood as follows. With increasing deviations of the Mn-O-Mn bond angle from the ideal 180°, the overlap between e_g and oxygen p orbitals decreases as sketched in Figure 2.2.2. Thus, the probability of electrons being in the overlapped region and with it the hopping amplitude across the oxygen orbital reduces. In the picture of the band structure, the decrease
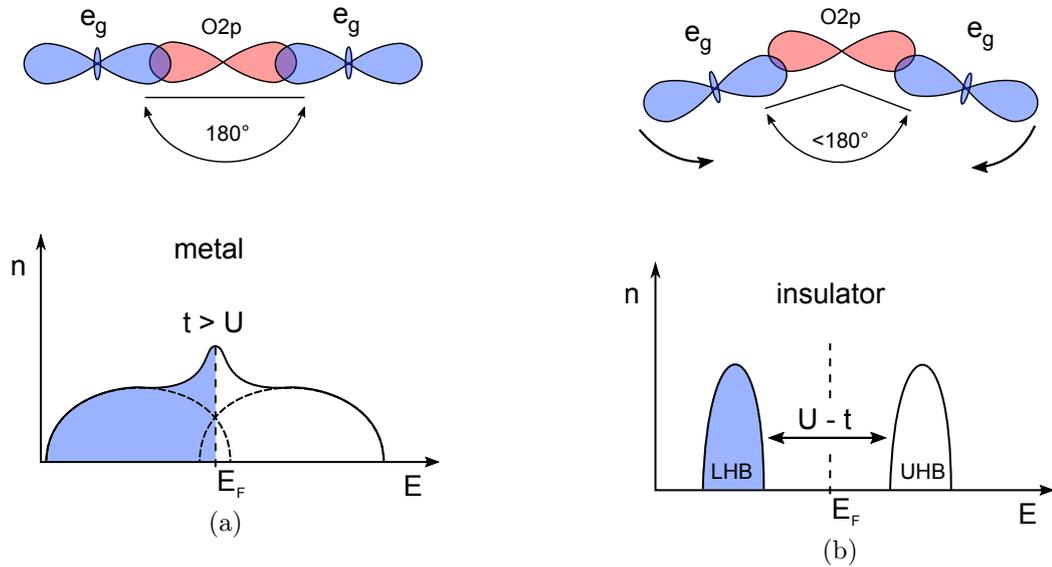
Figure 2.2.2: Effect of the MnO_6 octahedra rotations. With increasing rotational distortion, the overlap between the manganese e_g orbitals (blue) and the oxygen p orbitals (red) reduces. As a result, the effective hopping amplitude t and the bandwidth of the manganese e_g bands decrease. The narrowing of the bands leads to a transition (a) from a metallic state in the cubic structure, in which the bands overlap (b) to a Mott insulating state with two bands separated by a band gap of $\Delta E = U - t$.

in overlap results in manganese e_g and the oxygen p bands with decreased hybridization and bandwidth. Starting from a metallic cubic structure, in which the upper and lower Hubbard bands overlap due to their large bandwidth, they narrow until they split and form a gap of U-t as the rotational distortion increases as shown in the lower panel of Figure 2.2.2.

As already mentioned above, Jahn-Teller distortions lift the degeneracy of the e_g orbitals, which strongly impacts the transfer and magnetic properties. Systems with degenerate e_g orbitals tend to form a metallic ferromagnetic phase, while distorted materials often show antiferromagnetic insulating behavior with a magnetic structure, which depends on the details of the orbital ordering as shown for $LaMnO_3$ in Figure 2.2.1. Gaining access to optical control of rotational and Jahn-Teller degrees of freedom thus opens interesting possibilities for the modification of collective electronic and magnetic properties of manganites.

(a)
(b)
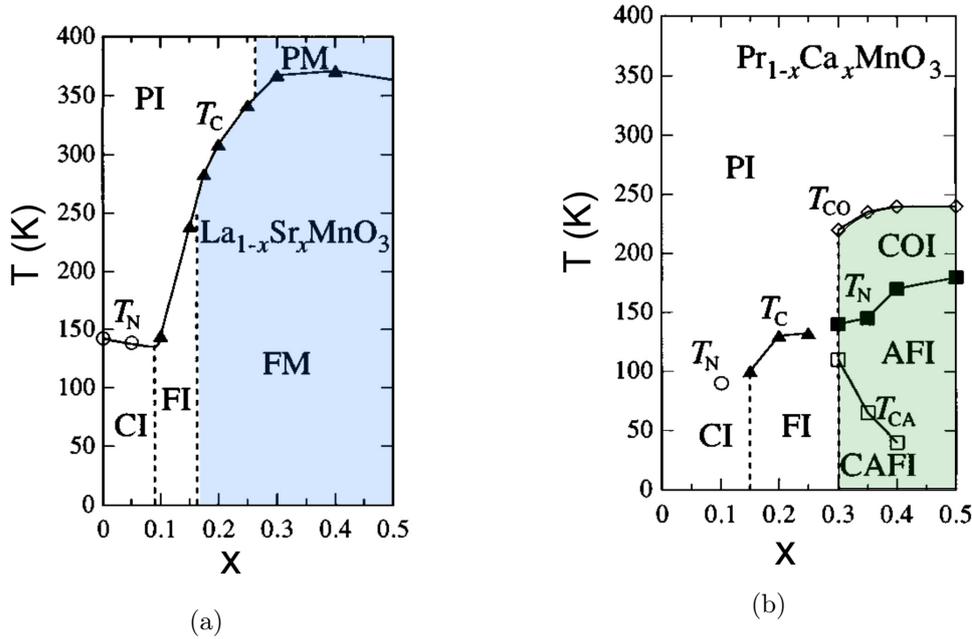
Figure 2.2.3: (a) Doping dependent diagram showing the electronic and magnetic phases of $La_xSr_{1-x}MnO_3$ [52]. The circles and triangles denote Néel T_N and Curie T_C temperatures (transitions from canted antiferromagnetic (C) and ferromagnetic (F) to paramagnetic (P) phases), respectively. The blue region shows metallic phases. (b) Doping dependent diagram showing the magnetic phases of $Pr_xCa_{1-x}MnO_3$, which is insulating over the whole doping and temperature range [53]. The diamonds denote the temperature below which charge order is found (T_{CO}). The green region shows the doping range, in which an externally applied magnetic field induces a metallic phase. In the green region, T_{CA} denotes the temperature below which the spins arrange in a canted antiferromagnetic order. The images are adapted from [53].

2.2.2   Insulator to metal transition in PCMO

Statically, the amount of rotational distortion can be controlled by chemical substitution. Replacing the A-site cations and dopants of the $AMnO_3$ system by atoms with smaller ionic radii increases the rotational distortion and favors charge localization and insulating states. While $La_xSr_{1-x}MnO_3$ shows ferromagnetic metallic behavior for $x > 0.15$, $Pr_xCa_{1-x}MnO_3$ (PCMO) has no metallic phase at any temperature or doping as shown in the electronic and magnetic phase diagrams in Figure 2.2.3 [53]. This is remarkable as most
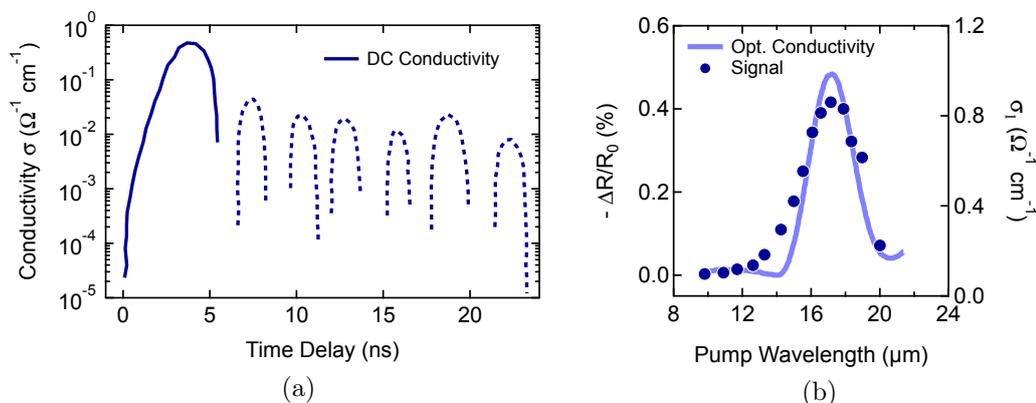
Figure 2.2.4: (a) Transient conductivity of the PCMO sample after resonant excitation of the infrared active B_{1u} Mn-O stretching mode. The conductivity increases by several orders of magnitude within the experimental resolution of 4 ns. The metallic state relaxes within few tens of ns. The dropping of the conductivity to zero is a result of ringing in the measurement circuit. (b) Wavelength dependence of the decrease in reflectivity of 800 nm pulses at +1ps time delay due to the induced metallicity. $\Delta R/R_0$ closely follows the peak in the optical conductivity due to the infrared B_{1u} mode. The images are adapted from [9].

other manganites exhibit ferromagnetic metallic behavior in certain doping ranges. If the formation of a metallic state in PCMO is however only prevented by the structural distortions, any external parameter disfavoring these distortions could potentially induce a metallic state. Indeed, an insulator to metal transition has been induced by photocarrier injection and the application of pressure[54, 55, 56, 20]. Exposing the PCMO to magnetic fields has been shown to induce a drop in resistivity by several orders of magnitude in the doping range $0.3 \leq x \leq 0.5$ [53].

This motivated Rini et al. in 2007 to perform a pump probe experiment, in which the Mn-O stretching B_{1u} mode at 17.5 μm of $Pr_{0.7}Ca_{0.3}MnO_3$ was resonantly excited and the transient sample conductivity determined by measuring the time resolved voltage drop across a 50Ω resistor. As shown in Figure 2.2.4, the sample conductivity was found to increase by more than four orders of magnitude within the measurement resolution of 4 ns and relax within several tens of nanoseconds. Optical mid-infrared pump, 800nm
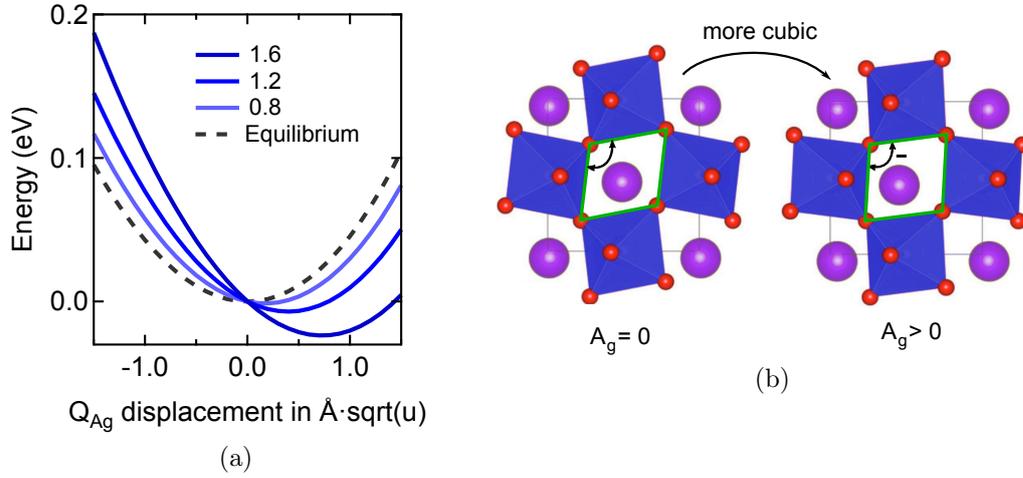
Figure 2.2.5: (a) Results of Density Functional Theory calculations. The energy potential curves of the rotational A_g symmetry Raman mode shift with increasing frozen Q_{B1u} amplitudes, in agreement with the cubic coupling discussed in section 1.1. (b) Motions in the positive direction of the A_g eigenvector Q_{Ag} describe a reduction in the rotational distortion of the MnO_6 octahedra, relaxing the orthorhombic lattice distortions. The crystal lattice becomes more cubic. The images are adapted from [41].

probe experiments show a drop in reflectivity with a rise time of 300fs, indicating a prompt formation of the metallic state. Figure 2.2.4 shows the pump wavelength dependence of this reflectivity drop across the resonance of the Mn-O stretching mode at 17.5 μm. The magnitude of $\Delta R/R$ follows the optical conductivity and peaks at the phonon resonance, a clear signature for a phonon driven phase transition.

A microscopic explanation for this ultrafast vibrationally driven insulator metal transition was proposed by Subedi et al. in 2014. Calculations combining Density Functional Theory within local density approximation and dynamic mean field theory (LDA + DMFT) of the parent compound $PrMnO_3$ have shown anharmonic coupling of the same resonantly excited Mn-O stretching motion of B_{1u} symmetry to a rotational A_g symmetry Raman mode [41]. Figure 2.2.5 shows the energy potential of the A_g Raman mode calculated for different frozen amplitudes of the infrared active B_{1u} mode. In agreement with the cubic coupling discussed in section 1.1 of the
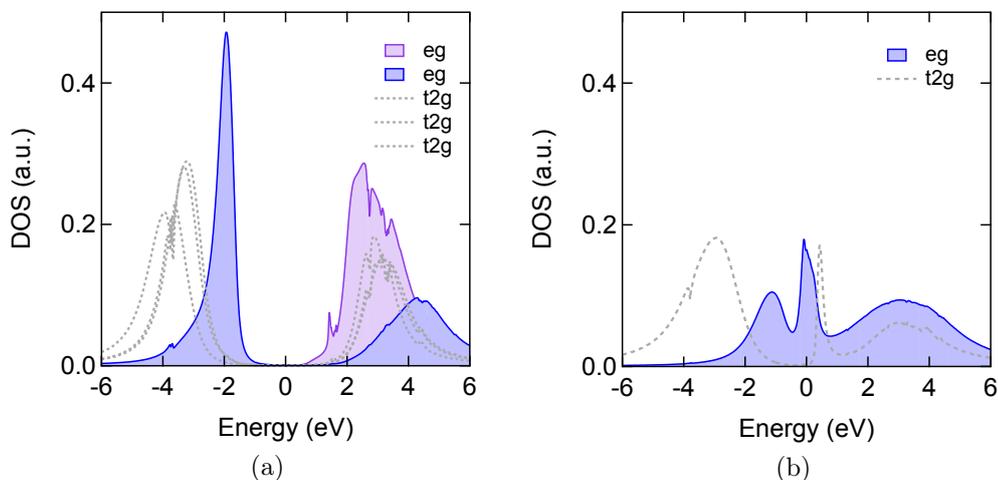
Figure 2.2.6: Shown is the calculated density of states of the e_g and t_{2g} Mn orbitals in the equilibrium orthorhombic structure (a) and the transient cubic structure (b). The increase in overlap due to the reduced octahedra rotations leads to a large increase in bandwidth of the e_g bands. The lower and upper Hubbard bands overlap in the cubic structure, forming a metallic state. The images are adapted from [41].

previous chapter, the energy potential shifts, while its slope, i.e. the mode frequency, is not affected. Importantly, the direction of this shift is positive in the A_g eigenvector mode Q_{Ag} independent of the sign of the frozen infrared mode displacements. According to the model of nonlinear phononics, the shift of the energy potential implies a directional force on the atoms along the A_g Raman mode in positive direction. Motions along positive Q_{Ag} describe a reduction in the rotational distortion of the MnO_6 octahedra. As a result, the crystal structure becomes more cubic as sketched in panel b) of Figure 2.2.5 and the overlap of the Mn e_g and oxygen p orbitals increases. As discussed above, the cubic structure favors metallic states as the bandwidth or hopping t increases. Indeed, calculations using the distorted transient cubic structure predict a metallic state due to a large increase in bandwidth of the e_g orbitals as shown in the lower panel of Figure 2.2.6.

2.2.3   Melting of Magnetic order in LSMO

The previous sections demonstrate how the optical control of octahedra rotations can be used to modify the collective electronic properties. Further strong interaction occurs between the structural Jahn-Teller distortions and the magnetic phase of manganites as exemplary shown for $LaMnO_3$ in Figure 2.2.1. The related compound $La_{0.5}Sr_{1.5}MnO_4$ is an antiferromagnetic insulator at temperatures below $T_N = 110K$. Charge and orbital ordering set in at $T_{CO/OO} = 220K$. Först et al. studied the response of the magnetic and orbital order to resonant lattice excitation of a Mn-O stretching vibration by resonant x-ray diffraction [11]. The sample was held at 25 K, well in the antiferromagnetic, charge and orbital ordered state, and excited with 130 fs, $1.2mJ/cm^2$ mid-infrared pulses at 13.5 μm and 4.5 μm bandwidth, covering the phonon resonance at 16 μm. Interestingly, both the orbital and the charge order react slowly to the fast excitation process, with a partial melting within 6.3 ps and 12.2 ps for the orbital and magnetic order, respectively, as shown in Figure 2.2.7.

An interpretation of the result can be given in the framework of nonlinear phononics. The excited infrared active mode is of B_{2u} symmetry and can to lowest (cubic) order couple to A_g modes. Among others, the Raman active Jahn-Teller mode at 15 THz is of A_g symmetry. As the frequency is too high for an impulsive excitation, no coherent oscillations are expected but a reduction or increase in the Jahn-Teller distortions is well possible. As both the orbital and magnetic order are reduced, a reduction in the Jahn-Teller distortions is a more likely scenario. This structural deformation would displace the free energy potential of both orbital and spin order at a timescale limited by the 130 fs duration of the mid-infrared pulses. Following the rapid excitation, the orbital and spin degrees of freedom will relax towards their new position of the energy minimum. The orbital order only involves an on-site redistribution of the e_g electrons of the Mn ions, whereas melting of magnetic order requires spin flips of the e_g electron and the three electrons of the t_{2g} orbitals, which could explain why the orbital order reacts faster to the excitation.
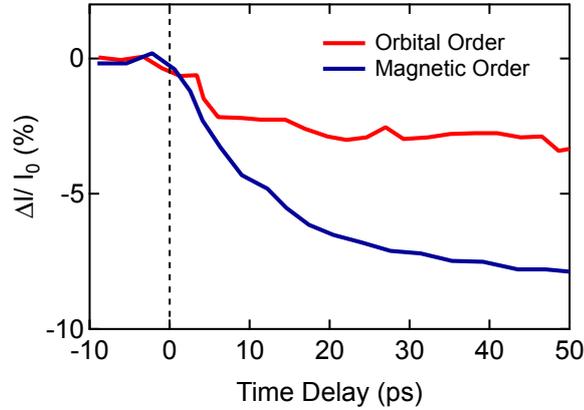
Figure 2.2.7: Shown is the time resolved relative change in intensity of the $\left(\frac{1}{4}, \frac{1}{4}, 0\right)$ (red) and $\left(\frac{1}{4}, \frac{1}{4}, \frac{1}{2}\right)$ (dark blue) diffraction peaks, which are sensitive to the orbital and magnetic order, respectively. Both, orbital and magnetic order peak intensity, reduce exponentially with timescales of 6.3 ps and 12.2 ps, respectively. The images are adapted from [11].

2.2.4 Summary

The presented studies show, how the Raman rotational and Jahn-Teller structural distortions can be optically controlled through anharmonic coupling to resonantly excited infrared-active modes. These Raman lattice modes couple strongly to the collective electronic and magnetic degrees of freedom. Previous measurements of ultrafast insulator to metal transitions and melting of orbital and magnetic order in manganites have been presented and interpreted in the framework of nonlinear phononics of Chapter 1.

Chapter 3

Light induced superconductivity in YBa$_2$Cu$_3$O$_{6+x}$

An especially intriguing transition following direct lattice excitation was found in 2014 in the high-temperature superconductor YBa$_2$Cu$_3$O$_{6+x}$ (YBCO). YBCO is a high temperature superconductor, which comprises bilayers of CuO$_2$ planes, separated by insulating layers. The superconducting state is characterized by coherent tunneling of Cooper pairs between neighboring CuO$_2$ planes both through the intrabilayer as well as the interbilayer regions. Above the transition temperature, the coupling through the interbilayer region is lost, preventing coherent tunneling, while signatures of coherent tunneling processes through the intrabilayer region are found up to temperatures far above T$_c$ [57]. In comparison of different cuprate compounds and investigations of YBCO under pressure, a connection between the distance of planar copper and the apical oxygen atoms of the interbilayer region and the transition temperature T$_c$ was found[29, 30, 31, 32, 58]. These findings were the motivation for a study set out to stabilize the interbilayer coupling by resonantly exciting an infrared-active mode comprising motions of these apical oxygen atoms between bilayers [7, 8].

The excitation of this lattice vibration has been shown to enhance the superfluid density below T$_c$ and induce coherent interlayer tunneling at temperatures above T$_c$ up to room temperature. This light-induced state, which

shows important similarities with the equilibrium superconductor, will in the following be referred to as superconducting-like. The search for the microscopic origin of this highly interesting state led us to investigate the excitation mechanism itself, the lattice dynamics. In the following sections, high temperature superconductors are introduced and the optical experiments showing the enhancement of interlayer coupling are summarized. The measurements of the underlying lattice dynamics and their effect on the superconducting phase are discussed in the next two chapters 4 and 5.

3.1 High temperature superconductors

The first superconductor was discovered by the group of Heike Kamerlingh Onnes in 1911. When they cooled mercury to a temperature below 4.2 K, they observed a sudden drop in the dc resistivity to zero. This state of perfect conductance was named superconductivity. In 1933, it was discovered that superconductors expel magnetic fields not only when the field is applied while the material is in its superconducting state but also, when the field is applied before the metal-superconductor transition. This second important property of superconductors was named Meißner-Ochsenfeld effect [59]. Following the discovery of superconductivity in mercury, a superconducting phase was found in many other metals. The transition temperature could however not be increased above 23K within 75 years. In 1986, Bednorz and Müller discovered a superconducting state in the ceramic perovskite $La_{2-x}Ba_xCuO_4$ of the cuprate family with a transition temperature T_c of 35 K [5], for which they were awarded the nobel prize in physics one year later. With their discovery, they found superconductivity in a completely new class of materials, which triggered the search for structurally similar materials with higher critical temperatures. Only one year after their discovery, $YBa_2Cu_3O_{6+x}$ was found to have a transition temperature of 93 K, above the cooling temperature of liquid nitrogen [60]. Since then, other materials were found with higher transition temperatures, superconductivity at temperatures close to room temperature could however never be achieved (see Figure 3.1.1).
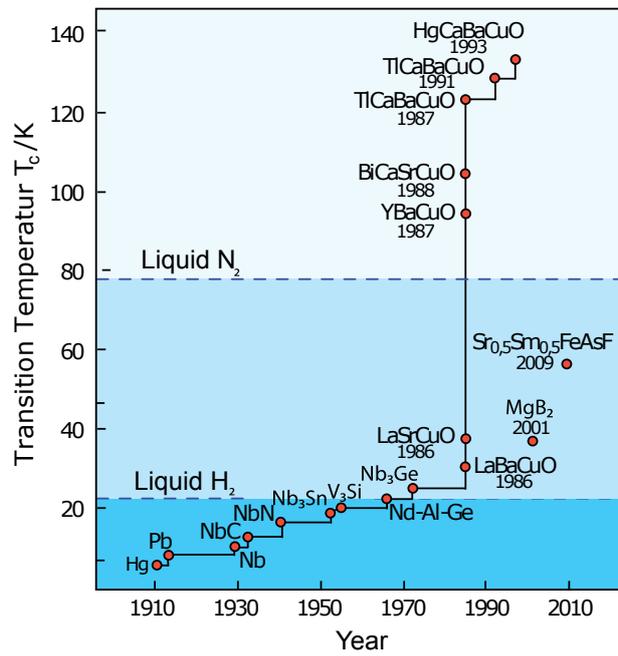
Figure 3.1.1: Transition temperature T_c records. Only one year after the discovery of the first high temperature superconductor $La_{2-x}Ba_xCuO_4$ in 1986, $YBa_2Cu_3O_{6+x}$ was found to have a transition temperature of 90K, above the cooling temperature of liquid nitrogen and five times the record T_c of metallic superconductors at that time. The image was taken from [61].
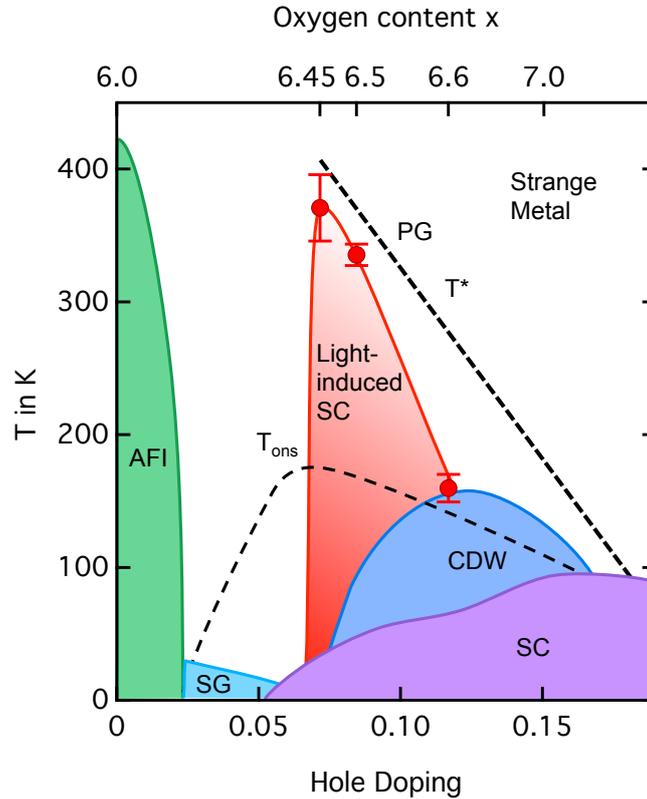
Figure 3.1.2: Hole-doping dependent phase diagram of $YBa_2Cu_3O_{6+x}$. The parent compound $YBa_2Cu_3O_6$ is an antiferromagnetic insulator (AFI). With increasing hole doping, the long range antiferromagnetic order breaks down and the system becomes metallic, with a spin glass (SG) phase at very low temperatures. The superconducting phase (SC) is suppressed at $1/8^{th}$ doping, at which charge density wave (CDW) order is observed [62, 63]. The pseudogap (PG, T*) and the onset temperature of precursor superconductivity (T_{ons}) appear on the underdoped side of the phase diagram far above T_c [57, 64]. Following resonant lattice excitation signatures of the light-induced superconducting-like state have been found throughout the red region of the phase diagram [7].

Phase Diagram

All high temperature superconductors of the cuprate family share the same structural components. Their electronic properties are determined by two dimensional CuO$_2$ planes, separated by an insulating spacing layer, which serves as charge reservoir for the CuO$_2$ planes. Depending on the material, there can be one or more of these layers per unit cell. The material investigated in this work, YBa$_2$Cu$_3$O$_{6+x}$, features two CuO$_2$ planes, separated by a thin insulating region that form a bilayer. Holes are introduced in these planes by increasing the oxygen content in the insulating region separating neighboring bilayers. The doping-dependent phase diagram is shown in Figure 3.1.2.

Antiferromagnetic Insulator (AFI)

The undoped parent compound $YBa_2Cu_3O_6$ is an antiferromagnetic insulator, in which the planar copper ions are ionized twice in a $3d^9$ configuration (Cu^{2+}). Hence, one electron is missing in the energetically highest $d_{x^2-y^2}$ orbital, which is oriented towards the p-orbitals of the four surrounding oxygen atoms in the plane. While half filled orbitals normally point towards a metallic ground state, the charges are localized due to a strong onsite Coulomb repulsion U that prevents hopping between different Cu sites (U is the energy needed to remove an electron from one copper ion $3d^9 \rightarrow 3d^8$ and add it to its nearest neighbor $3d^9 \rightarrow 3d^{10}$). $YBa_2Cu_3O_6$ is a charge transfer insulator with the lowest electronic excitation being a charge transfer from the oxygen p- to the copper d-Orbitals, as discussed in Chapter 2. The superexchange interaction of the localized charges leads to an antiferromagnetic arrangement of the spins, similar to the mechanism in manganites. Small hole doping levels of 2% lead to a transition into a metallic state, accompanied by the breakdown of long range antiferromagnetic order, which is replaced by a spin-glass phase at temperatures below 30 K.

The removal of electrons from the planes allows hopping processes to empty d orbitals of nearest neighbor sites. Thus, few empty sites suffice to create conducting channels through the material. While diagonal hopping
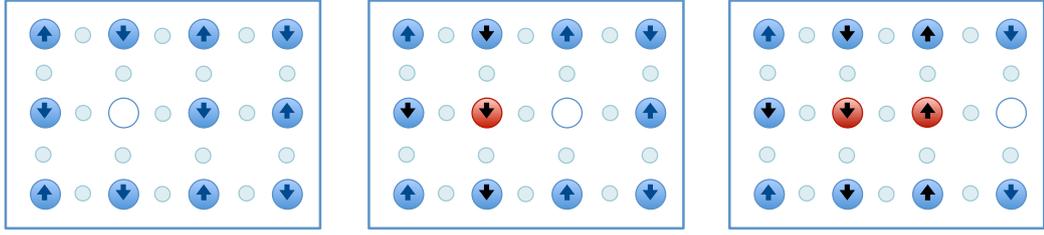
Figure 3.1.3: Antiferromagnetic order in the CuO_2 plane. Cu atoms are shown in solid blue, oxygen atoms in light blue. Motions of electrons to empty sites of nearest copper atoms involve a spin flip and leave a path of frustrated antiferromagnetic order.

does not disrupt the antiferromagnetic order, motions of electrons to the nearest copper atoms involve a spin flip and frustrate antiferromagnetic long-range order as shown in Figure 3.1.3 [65].

Superconductivity (SC)

As the oxygen content is further increased, a superconducting phase in the shape of a dome develops with the highest transition temperature of 93 K at optimal doping of x $\approx$ 6.9. The electrons with energies close to the Fermi level that form Cooper pairs are due to the bands of the planar copper atoms with strong $d_{x^2-y^2}$ character. Angle resolved photoemission measurements show the development of a gap with $d_{x^2-y^2}$ symmetry of $\sim$ 30 meV at optimal doping, which increases towards lower hole doping levels [66, 64, 67].

Pseudogap (PG, T)

At the underdoped side of the phase diagram, an additional gap was found to persist up to temperatures of 400 K, far above the transition temperature T_c. The nature of this so called pseudogap is still debated. The symmetry of the pseudogap is very close to the symmetry of the superconducting gap and evolves smoothly across T_c, which is why it has been proposed to originate from preformed incoherent Cooper pairs. However, competing orders such as charge correlations could also cause the opening of a gap and the pseudogap could well be a combination of superconducting pairing and competing orders [64].

Charge density wave order (CDW)

The superconducting phase shows a suppression at $1/8^{th}$ doping. In recent resonant elastic x-ray scattering experiments, incommensurate charge density wave (CDW) order was found at this doping level in YBa$_2$Cu$_3$O$_{6+x}$ [68]. The intensity of the diffraction peak rises with decreasing temperature down to the transition temperature of the superconducting phase, below which it starts to reduce, suggesting a competition between superconductivity and charge order. Further experiments have shown that the suppression of charge order below T$_c$ can be reversed by applying a magnetic field, which destroys superconductivity [69]. In following studies, the doping dependence of the charge order was investigated [62, 63]. The formation of competing charge or spin orders at $1/8^{th}$ doping is a general property of cuprates and is most strongly pronounced in $La_{2-x}Ba_xCuO_4$, in which the superconducting state is completely suppressed, while spins and charges order in stripes.

Precursors of superconductivity (T$_{ons}$)

The temperature-driven metal-superconductor transition in YBa$_2$Cu$_3$O$_{6+x}$ is accompanied by large changes in the phonon spectrum due to the coherent tunneling of Cooper pairs through the thin barrier within bilayers. These changes have been found to persist up to 150 K in YBa$_2$Cu$_3$O$_{6.5}$ and have been proposed to be a signature of the existence of Cooper pairs far above T$_c$. At these temperatures, coherent tunneling through the larger region separating different bilayers is prevented by large phase fluctuations. The doping dependence of the temperature T$_{ons}$, up to which these signatures of coherent intrabilayer tunneling are found, defines a possible precursor phase of superconductivity [57].

Light-induced superconductivity

The first superconducting state induced by resonant lattice excitation with mid-infrared pulses was found in 2011 by Fausti et al. [6]. The investigated material was $La_{1.8-x}Eu_{0.2}Sr_xCuO_4$ at x = 1/8 doping, in which the superconducting phase is fully suppressed by a strong ordering of the spins and charges

in stripes, which are pinned by a structural lattice distortion that sets in at higher temperatures. Following the excitation of an infrared-active phonon mode, signatures of superconducting tunneling were found up to temperatures of $\sim$20 K. Further resonant x-ray diffraction studies have shown that the charge order melts at the same timescale as superconductivity appears, which led to the interpretation that the resonant lattice excitation restores the superconducting state by selectively melting the competing charge order [28]. This interpretation also explains the maximum temperature of 20 K up to which the superconducting state could be restored. The following discussion will be focused again on light induced superconductivity in $YBa_2Cu_3O_{6+x}$.

As described above, signatures of Cooper pairs and coherent tunneling processes within bilayers have been found at temperatures far above T_c. The coupling between the bilayers is however too small to allow coherent tunneling of Cooper pairs between different bilayers and the formation of the superconducting phase at higher temperatures. The experiments mentioned in the introduction have shown that the resonant excitation of the infrared-active phonon mode comprising apical oxygen vibrations between the bilayers induces coherent interbilayer tunneling above T_c [7, 8]. Signatures of interbilayer coupling have been found up to temperatures of 300 K as shown in the phase diagram.

In the following sections, the superconducting phase and its precursor state will be explained in more detail, followed by a summary of the experiments on the observed superconducting-like state following resonant lattice excitation. The investigation of the lattice dynamics are presented in the next chapter 4 and 5.

3.1.1   The superconducting state $\mathbf{T} < \mathbf{T_c}$

All high temperature superconductors of the cuprate family share the same structural components. Their electronic properties are determined by 2-dimensional CuO$_2$ planes, which are separated by an insulating spacing layer. During the temperature-driven metal-insulator transition, Cooper pairs are formed in these planes.

Josephson tunneling across CuO$_2$ layers

This structure is very similar to the macroscopic Josephson junction, which describes a heterostructure of two superconductors separated by a thin, non-superconducting region. Originally, the probability for tunneling of two electrons forming a Cooper pair through this barrier was believed to be orders of magnitude smaller than the probability for quantum tunneling of a single electron and thus impossible to observe experimentally. In his original publication, Josephson proposed that the pairs can tunnel coherently through this barrier [70] with the same tunneling probability as a single electron.

The superconducting electrons in each superconducting layer have the same phase $\theta\left(\mathbf{r}, t\right) = \mathbf{k}\mathbf{r} - \omega t$ and form a condensate, which can be described by a macroscopic wave function $\psi = \sqrt{n_s}e^{i\theta}$, where $n_{si}\left(\mathbf{r}, t\right) = \left|\psi\left(\mathbf{r}, t\right)\right|^2$ denotes the density of the Cooper pairs. While the Cooper pairs in each superconductor have the same phase, there can be a phase difference between the two superconductors of the junction. The supercurrent flowing through the barrier depends on their relative phase φ and is given by the first Josephson equation

$$I_s = I_c \sin \varphi \tag{3.1.1}$$

for the simple case of a lumped Josephson junction with a constant phase relationship and critical current across the junction area. Here, I_c denotes the critical current of the junction. As evident from equation 3.1.1, I_c is an upper limit for the supercurrent flowing through the junction. The second Josephson equation can be written as

$$\frac{d\varphi}{dt} = \frac{2\pi}{\Phi_0}V, \tag{3.1.2}$$

with ϕ_0 denoting the magnetic flux quantum. The relation between current and voltage can be derived by taking the time derivative of the first equation:

$$\frac{dI_s}{dt} = I_c \cos\varphi \frac{d\varphi}{dt} = \frac{2}{\Phi_0}I_c \cos\varphi V = L^{-1}V.$$

The Josephson junction can thus be described by an inductance L. Van der Marel proposed a very elegant model for the optical properties of the superconducting state in cuprates by describing each microscopic junction by an equivalent circuit, consisting of an induction parallel with a capacitance to account for displacement currents [71]. The structure of cuprates can be thought of as a stack of these microscopic Josephson junctions. Equivalent to the two fluid model, the quasi-particle current due to charge carriers that are not paired is incorporated by shunting each junction with an ohmic resistor in series with an induction. The complex impedance for the junction m of Figure 3.1.4a can be expressed as

$$\frac{1}{Z_m} = \frac{1}{R_{m,S} - i\omega L_{m,S}} - \frac{1}{i\omega L_m} - i\omega C_m,$$

with $R_{m,S}$ and $L_{m,S}$ being the resistance and induction of the shunt and C_m, L_m the capacitance and induction of the Josephson junction. The total impedance is composed of the impedance of the single junctions in series: $Z = \sum_m Z_m$.

Optical Properties of the superconducting state

The optical conductivity and permittivity directly follow from $\sigma = D(AZ)^{-1}$ and $\varepsilon = 4\pi i\sigma\omega^{-1}$, with A and D denoting the junction area and the thickness of the crystal. They can be expressed by a sum over the permittivity of the microscopic junctions, weighted by a factor $w_m = d_m/D$, proportional to the distance between the superconducting layers of the junction d_m (see Appendix A.3 for the derivation of the following equations):

$$\sigma = \left(\sum_m \frac{w_m}{\sigma_m} \right)^{-1}, \text{ with } \sigma_m = \left(\sigma_{m,S} + \frac{\omega}{4\pi i} \varepsilon_r \left(1 - \frac{\omega_m^2}{\omega^2} \right) \right), \quad (3.1.3)$$

$$\varepsilon = \left(\sum_m \frac{w_m}{\varepsilon_m} \right)^{-1}, \text{ with } \varepsilon_m = \left(\frac{4\pi i}{\omega} \sigma_{m,S} + \varepsilon_r \left(1 - \frac{\omega_m^2}{\omega^2} \right) \right). \quad (3.1.4)$$

The reflectivity at normal incidence is then given by

$$R = \left| \frac{1 - \sqrt{\varepsilon}}{1 + \sqrt{\varepsilon}} \right|. \quad (3.1.5)$$

In addition to the $1/\omega$ divergence in σ_2, which is a property of every superconductor due to the delta peak in the conductivity σ_1 at $\omega = 0$ (zero dc resistivity), the model predicts that for n CuO_2 layers per unit cell there are $(n-1)$ transverse modes and n longitudinal modes at finite frequencies that appear as edges in the reflectivity and peaks in the loss function. The material investigated in this work, $YBa_2Cu_3O_{6+x}$, comprises bilayers of two CuO_2 planes per unit cell, separated by a thin insulating layer. In the superconducting state, Cooper pairs tunnel coherently both through the thin intrabilayer region as well as through the large and weakly coupled interbilayer region. These two tunneling regions are shown in Figure 3.1.4b. Their plasma frequencies are given by $\omega_m = 4\pi\Phi_0^{-1}\varepsilon_r^{-1}d_m J_m$, where J_m denotes the Josephson coupling.

Figure 3.1.5 shows a comparison of experimental data of $YBa_2Cu_3O_{6.5}$[35] with model calculations. The main features of the superconducting state are well reproduced by the model. The two Josephson plasma resonances of the interbilayer junction at $\omega_{p1} = 29$ cm^{-1} and the bilayer junction at $\omega_{p1} = 475$ cm^{-1} have clear signatures in the loss function and the reflectivity. The transverse mode at $\omega_0 = 400$ cm^{-1} wavenumbers is visible in the real part of the optical conductivity σ_1. The remaining peaks in the experimental data are due to infrared-active phonons that are not included in the model.
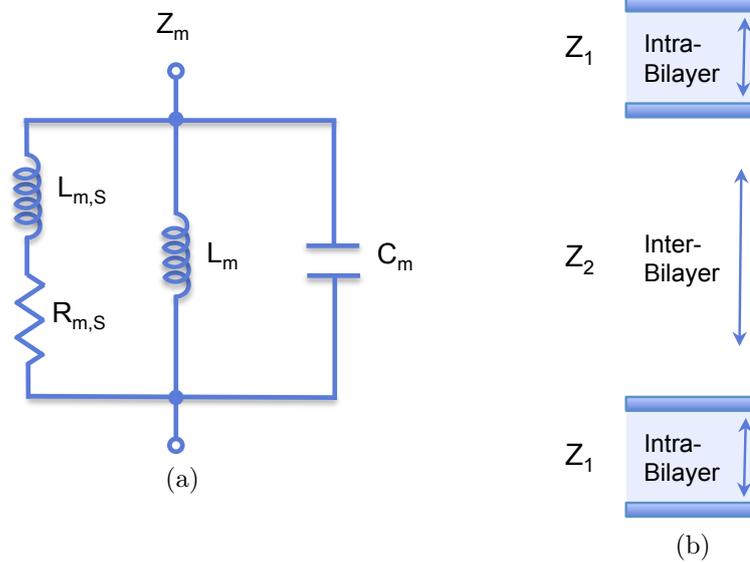
Figure 3.1.4: (a) The optical properties of a Josephson junction at $\mathbf{k} = 0$ can be described by an equivalent LC circuit. Quasi-particle currents are introduced by a shunting the circuit with a resistance $R_{m,S}$ in series with an inductance $L_{m,S}$ [71]. (b) YBa$_2$Cu$_3$O$_{6+x}$ is a bilayer superconductor, comprising two Josephson junctions per unit cell with impedances Z_1 and Z_2. Panel (b) is taken from [33].
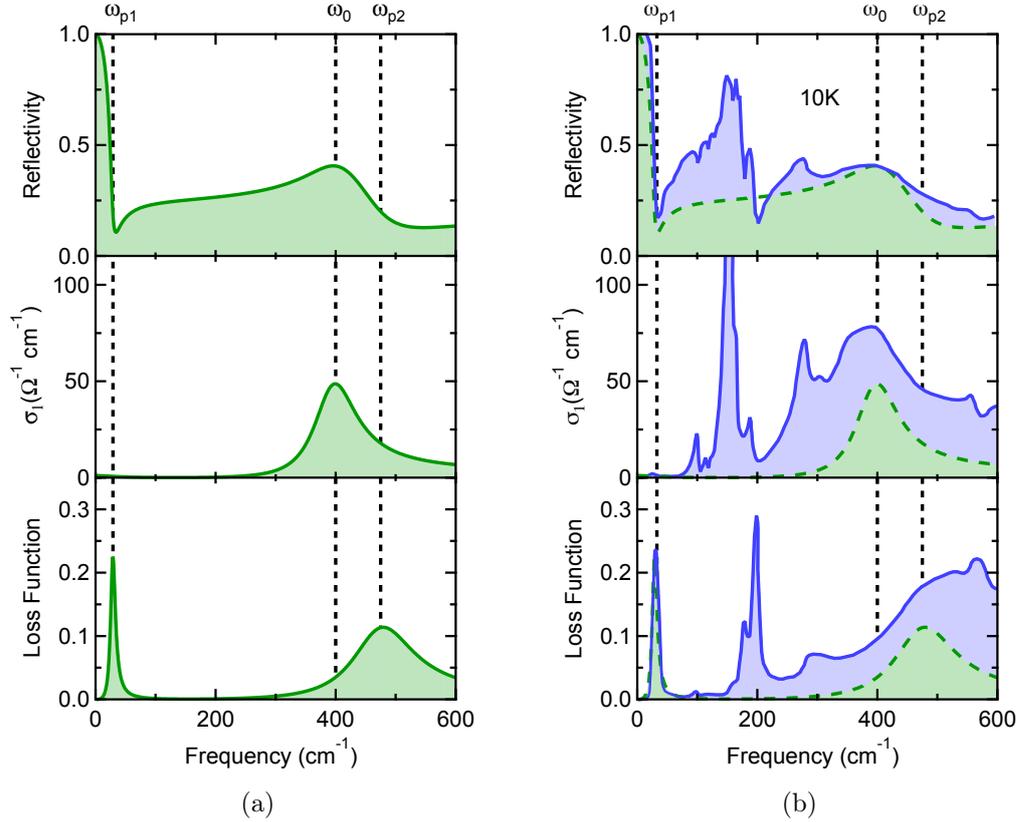
Figure 3.1.5: Optical properties of $YBa_2Cu_3O_{6.5}$ in its superconducting state. (a) Simulations according to Equations (3.1.3-3.1.5), showing the reflectivity, real part of the optical conductivity and the loss function. Coherent tunneling through the intrabilayer and interbilayer junctions gives rise to two longitudinal modes, which appear as edges in the reflectivity and peaks in the loss function at ω_{p1} and ω_{p2}, and a transverse mode showing up as a peak in σ_1 at ω_0. (b) Comparison with experimental data (blue) taken at 10 K. The data has been reproduced from [35]. Deviations are due to infrared-active phonon modes, which are not included in the simulation.

3.1.2 Precursors of superconductivity at $T > T_c$

The model discussed above describes the most important optical signatures of the superconducting state in the cuprates. It fails however to explain their temperature dependence. As shown in Figure 3.1.6a, the emergence of the transverse mode is accompanied by a phonon reshaping in the spectral range of 200 cm^{-1}-700 cm^{-1}, which is strongest for the Cu-O bending mode at 320 cm^{-1}. The transverse mode gains spectral weight from this phonon mode. Munzar et al. extended the original model by including local fields acting on the ions of the infrared-active phonon modes [72]. The phonon anomalies can be explained by changes in these local electric fields due to the transition in the superconducting state. The only varied parameter in the model calculations shown in Figure 3.1.6b is the damping rate γ of the transverse mode.

This phonon reshaping persists up to 150 K, far above the transition temperature of $T_c \approx 59K$ and has been proposed to be the signature of a precursor state of superconductivity [57]. During the cooling process, Cooper pairs are formed in the CuO$_2$ planes and Josephson coupling develops within the strongly coupled bilayers. While this process sets in above the transition temperature, large phase fluctuations prevent coherent tunneling between the superconducting condensates of adjacent bilayers. Indeed, the Josephson plasma edge associated with the weakly coupled interbilayer junction disappears above T_c as shown in Figure 3.1.6c.
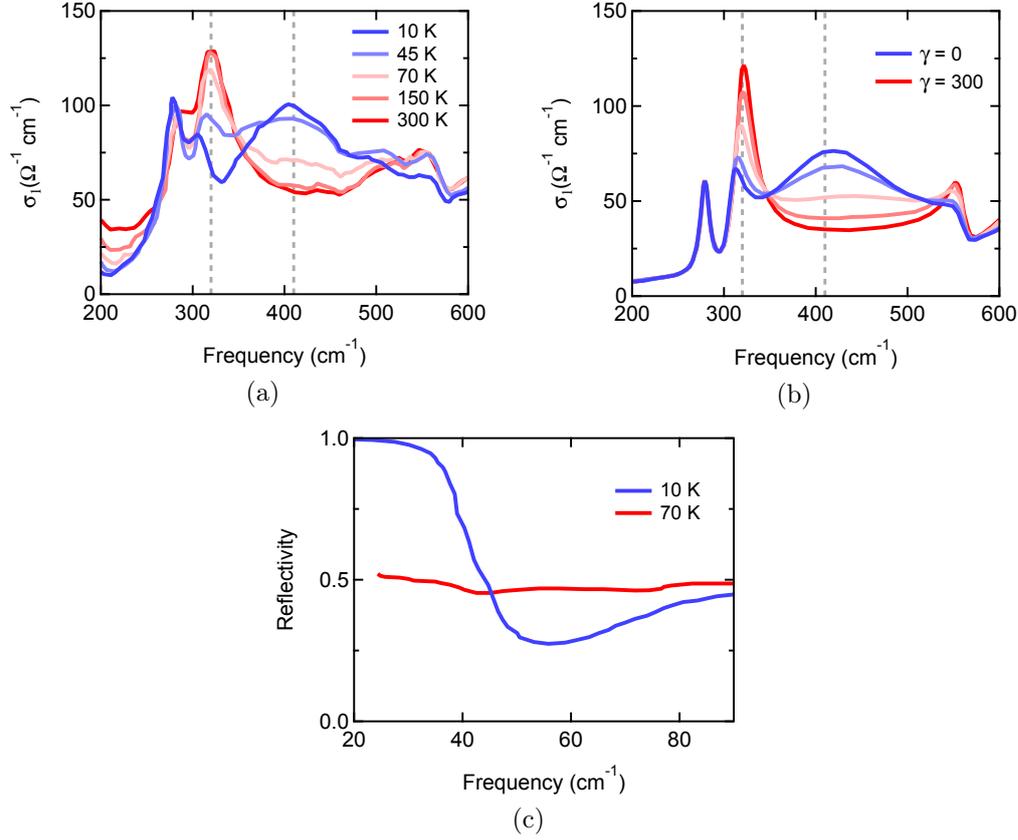
Figure 3.1.6: Temperature-dependent optical conductivity of YBa$_2$Cu$_3$O$_{6.6}$. (a) The experimental data shows a transfer of spectral weight from the 320 cm^{-1} phonon mode to the transverse plasma mode at 410 cm^{-1} that sets in at 150 K, far above T$_c$ $\sim$ 59 K. (b) The phonon anomaly can be modeled by extending the two Josephson junctions by local field effects according to the model of Munzar et al. [72]. In the simulations shown, the only parameter varied is the damping rate γ of the transverse mode. (c) In contrast to the emergence of the transverse mode, the low-frequency Josephson plasma edge of the interbilayer junction disappears rapidly above T$_c$. The figure was adapted using the data and model calculations taken from [73, 74].

3.2 Optically induced superconductivity

Following the discussion above, there is evidence for the existence of Cooper pairs at temperatures far above the transition temperature into the superconducting state. While coherent intrabilayer tunneling might exist up to 150 K in $YBa_2Cu_3O_{6.5}$, the transition temperature of $T_c = 50$ K is limited by the weak coupling of the interbilayer junction. In this section, the experiments mentioned in the introduction are summarized. The transient superconducting-like state was induced by resonant excitation of an infrared-active mode comprising c-axis apical oxygen motions between the bilayers with mid-infrared pulses at 15 µm wavelength and a fluence of 4 mJ/cm². Following the excitation, changes in the THz optical properties of YBCO were probed below and above the transition temperature T_c by measuring the electric field of reflected THz pulses, generated by ZnTe with spectral content from 20-85 cm^{-1}, by electro-optic sampling [7]. In a second experiment, broad band pulses with spectral content up to 500 cm^{-1} generated by gas ionization were used to gain information on the intrabilayer coupling and the transverse mode in addition to the interbilayer coupling [8].

Below T_c

1. At 10 K, part of the Josephson plasma resonance of the interbilayer junction blue shifts. The original peak in the loss function reduces in intensity, while a second peak appears at ~ 60 cm^{-1}, suggesting an inhomogeneous light-induced state. See panel (a) of Figure 3.2.1.

2. This effect is accompanied by a red shift of the intrabilayer plasma resonance and the transverse mode. Recalling the formula for the plasma frequency $\omega_m = 1/\sqrt{C_m L_m} \sim \sqrt{I_c}$, an increase in frequency can be explained by an increase in critical current I_c. The observed signatures can thus be understood as an increase in coupling strength of the interbilayer junction at the expense of intrabilayer coupling strength. Interestingly, the total coherent spectral weight, which is the spectral weight associated to superconducting carriers, is conserved. The coherent spectral weight is defined as the integral of $\sigma_1(\omega)$ over ω and is proportional to the number of superconducting carriers [75]. With $\omega_p^2 = (2/\pi\epsilon_0) \int \sigma_1 d\omega$, the total coherent spectral weight scales with $\omega_{p1}^2 + \omega_{p2}^2$ and the signatures can also be interpreted as an increase in the interbilayer plasma frequency ω_{p1} from zero accompanied by a decrease in the intrabilayer plasma frequency ω_{p2} with the sum of their squares being conserved. See panels (c, d) of Figure 3.2.1.

3. A strong increase in the slope of σ_2 was observed, suggesting an enhancement of the superfluid density, which is proportional to $\omega\sigma_2|_{\omega\to 0}$ in equilibrium. See panel (b) of Figure 3.2.1.
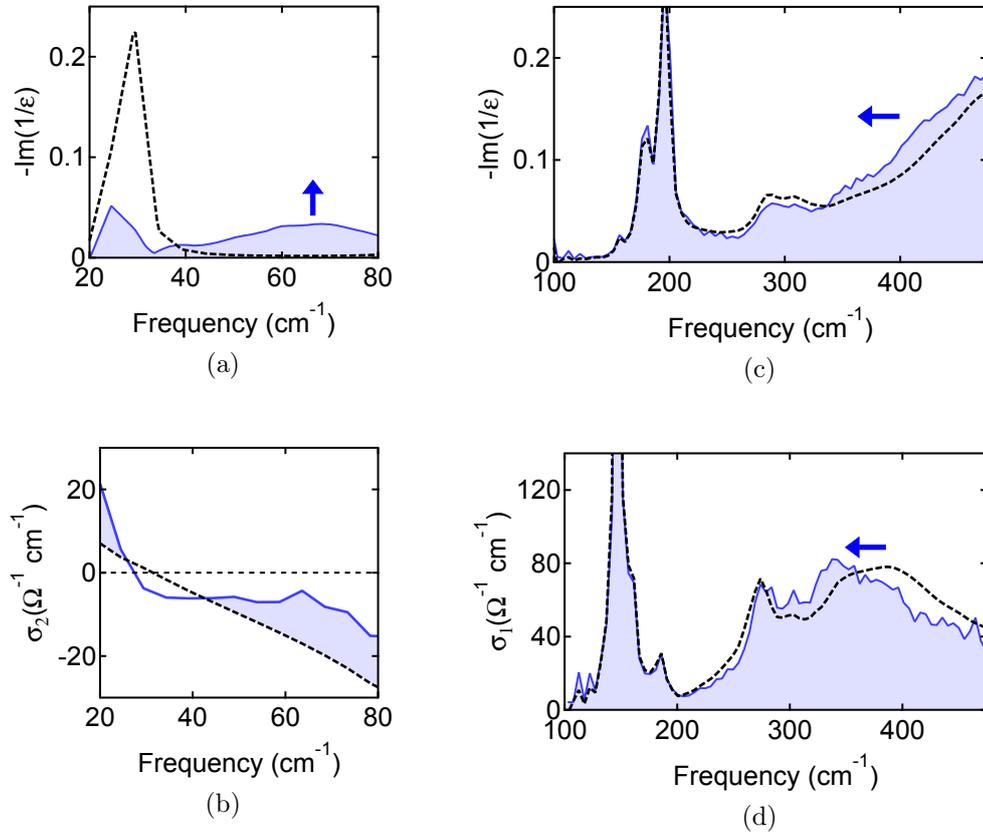
Figure 3.2.1: Equilibrium (dashed black line) and transient (blue line) optical properties of $YBa_2Cu_3O_{6.5}$ $\sim$0.5 ps after resonant lattice excitation at 10 K, below T_c. (a) The loss function peak of the interbilayer plasma resonance splits into two peaks, one of which is blue shifted to 60 cm^{-1}. (b) The slope of σ_2 increases towards low frequencies. (c, d) Both the loss function peak of the intrabilayer junction and the 400 cm^{-1} peak in σ_1 due to the transverse mode shift to lower frequencies. The images are adapted from [8].

Above T$_c$

1. At 60 K immediately above T$_c$, there is no low-frequency peak in the loss function in equilibrium. Following the excitation, a broad peak appears at ~ 50 cm^{-1}, which can be attributed to Josephson coupling of the interbilayer junction. See panel (a) of Figure 3.2.1.

2. Similar to the response below T$_c$, this effect is accompanied by a red shift of the intrabilayer junction and the transverse mode. Notably, the total coherent weight is conserved, i.e. the increase in coupling strength of the interbilayer junction is compensated by the decrease of coupling strength of the strongly coupled intrabilayer region. See panels (c, d) of Figure 3.2.1.

3. An enhancement in σ_2 was observed, which increases at low frequencies, suggesting an enhancement of the superfluid density. See panel (b) of Figure 3.2.1.

The resonant lattice excitation thus strengthens the superconducting state by increasing the interbilayer coupling strength, effectively curing the weak spot of superconductivity in YBa$_2$Cu$_3$O$_{6+x}$. These light-induced signatures of superconductivity persist up to room temperature as shown in the phase diagram of Figure 3.1.2. With increasing temperature, the size of the signature decreases however, which corresponds in an effective medium picture to a decrease in the superconducting area from 20% to only a few %. The lifetime of the state decreases with temperature from 7 ps at 10 K to 2 ps at 300 K.
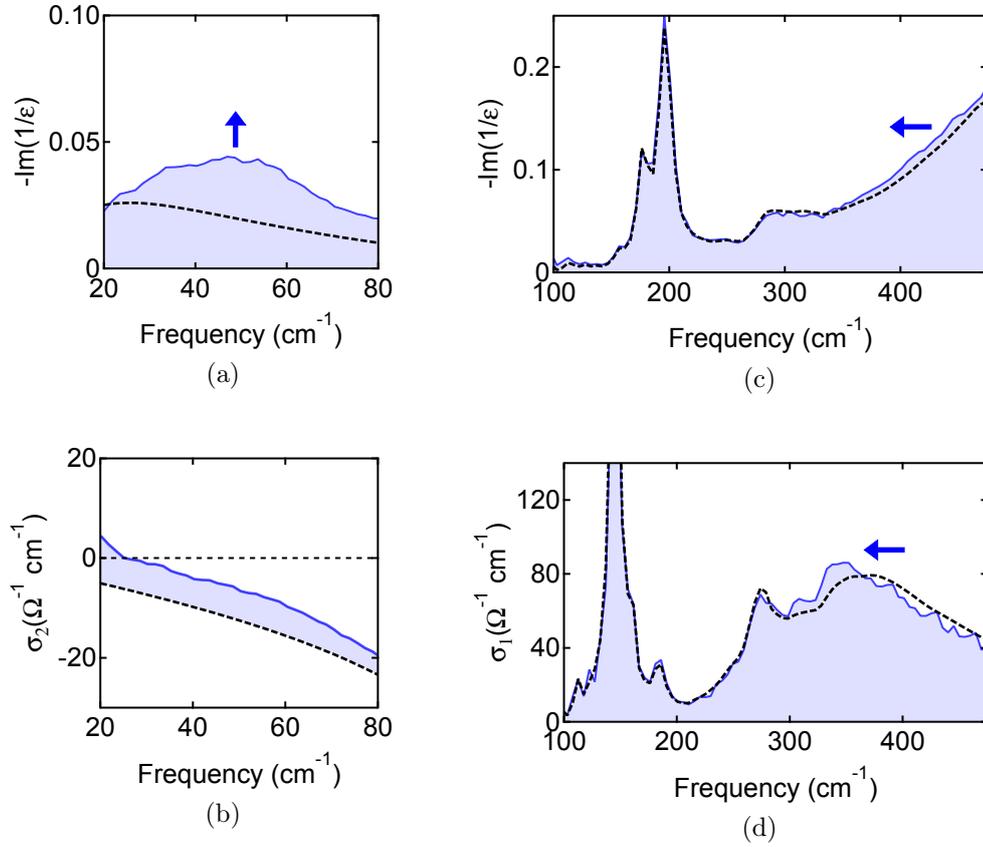
Figure 3.2.2: Equilibrium (dashed black line) and transient (blue line) optical properties of YBa$_2$Cu$_3$O$_{6.5}$ ~0.5 ps after resonant lattice excitation at 60 K, above T$_c$. (a) A peak in the loss function appears at 50 cm^{-1}, which can be attributed to the interbilayer plasma resonance. (b) The slope of σ_2 increases towards low frequencies. (c, d) Both the loss function peak of the intrabilayer junction and the 400 cm^{-1} peak in σ_1 due to the transverse mode shift to lower frequencies. The images are adapted from [8].

3.3 Summary

We conclude that 3-dimensional superconductivity in YBa$_2$Cu$_3$O$_{6.5}$ is characterized by coherent tunneling of cooper pairs across the inter- and intrabilayer junctions. While intrabilayer coupling can persist up to higher temperatures, the interbilayer coupling and its plasma resonance are lost above T$_c$. Thus, the weak coupling of the bilayers might be the only obstacle preventing superconductivity at higher temperatures. The temperature-driven transition in the superconducting state of YBa$_2$Cu$_3$O$_{6+x}$ is accompanied by large changes in the THz optical properties. A large reshaping of the phonon spectrum has been observed alongside the development of a transverse plasma mode due to Josephson coupling of the CuO$_2$ planes. The onset temperature T$_{ons}$ of these phonon anomalies was shown to be significantly higher than the transition temperature in the superconducting state T$_c$. The emergence of the transverse mode has been proposed to be due to the formation of superconducting pairs in the CuO$_2$ planes, while large phase fluctuations prohibit coherent tunneling between them [57].

Below T$_c$, the resonant excitation of an infrared-active phonon mode comprising apical oxygen movements between bilayers enhances the superfluid density and increases interbilayer coupling, which strengthens the superconducting state. The same excitation induces coherent tunneling through the interbilayer junction above T$_c$ up to room temperature, creating a short lived state with all optical signatures of the superconducting state.

Chapter 4

Lattice displacements as basis for induced superconductivity

Understanding the physics and chemistry that enhances superconductivity and supports coherent tunneling of cooper pairs at temperatures above 300 K might be a major step towards the design of equilibrium room temperature superconductors. A natural starting point to investigate this emergent phase is the excitation mechanism itself. To derive the response of the lattice, the atomic motions in $YBa_2Cu_3O_{6.5}$ ($YBCO_{6.5}$) were traced using time-resolved hard x-ray diffraction following the same vibrational excitation of the previous experiments presented in Chapter 3. The lattice excitation of normal-state $YBCO_{6.5}$ at 100 K was found to cause an atomic rearrangement into a transient structure, which occurs and decays on the same timescales as the signatures of superconductivity measured previously [7, 8]. The combination of the experimental results with Density Functional Theory (DFT) calculations of the anharmonic phonon coupling strengths allowed us to quantify these atomic motions. Their role in the enhancement of superconductivity is assessed by comparing DFT calculations of the electronic properties using the equilibrium and transient crystal structures. Parts of this chapter are taken from Ref. [33].

77
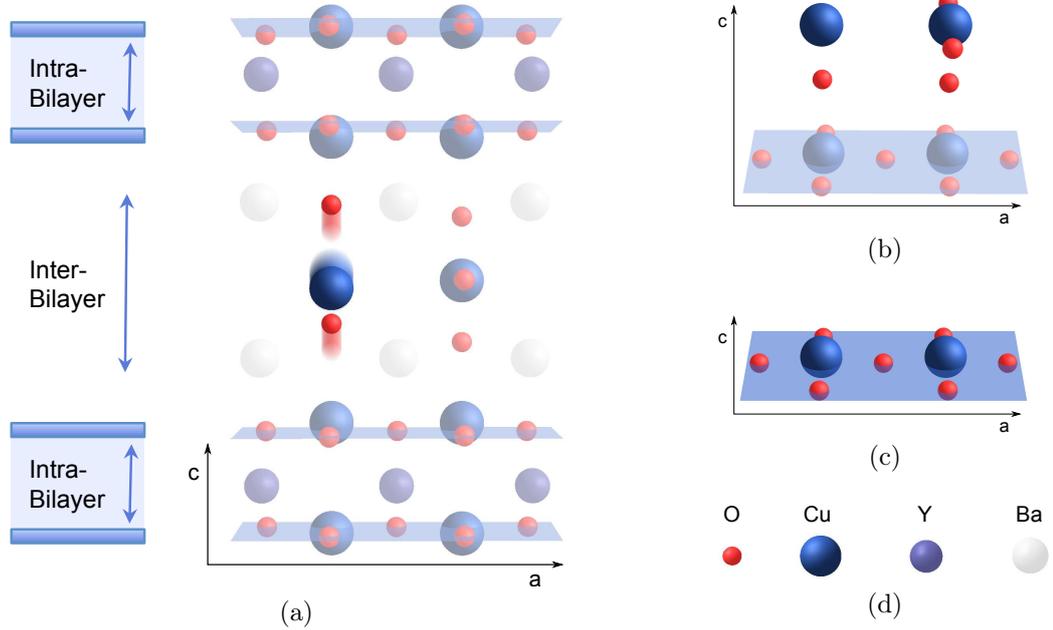
Figure 4.1.1: (a) Structure of orthorhombic $YBa_2Cu_3O_{6.5}$ and motions of the optically excited B_{1u} mode, composed of oxygen and copper c-axis motions at empty chain sites [35]. The sketch on the left shows the two tunneling regions respectively within and between the bilayers. (b) Cu–O chains, which are either filled (Cu on right) or empty (Cu on left) in the ortho-II structure. (c) Superconducting CuO_2 planes (blue). The images are taken from [33].

4.1 Transient crystal structure

The investigated material, $YBa_2Cu_3O_{6.5}$, is a bilayer superconductor, which crystallizes in a centrosymmetric orthorhombic unit cell with D_{2h} symmetry, comprising bilayers of CuO_2 planes separated by an insulating layer containing Yttrium atoms. The two tunneling regions within and between these bilayers are sketched in Figure 4.1.1a. The interbilayer region contains Cu-O chains that serve as charge reservoir and control the hole doping of the planes. With increasing oxygen content, the hole doping of the planes increases as a larger fraction of the electrons is attracted by the chains. As the chains become consecutively filled, they form different superstructures [76]. The $YBCO_{6.5}$ sample contained both oxygen rich and oxygen deficient chains, and exhibited short-range Ortho-II ordering of the vacancies, in which

adjacent chains are alternately filled or empty as shown in panel b) of Figure 4.1.1. This oxygen Ortho-II superstructure leads to a doubling of the unit cell along the crystallographic **a** direction. The in-plane O-Cu-O bonds are buckled, as shown in panel c) of Figure 4.1.1.

The lattice was excited with mid-infrared pump pulses of ∼300 fs duration, which were focused to a maximum fluence of 4 mJ/cm² and a peak electric field of 3 MV/cm. These pulses were polarized along the c axis of YBCO$_{6.5}$ and tuned to resonance with the same 670 cm^{-1} frequency (15 μm, 83 meV) B_{1u} infrared-active mode that was previously shown by means of time-resolved THz spectroscopy to induce interlayer superconducting coupling as summarized in section 3.2. More details on the experimental setup and the measurement technique can be found in Appendix C.

4.1.1 Cubic order coupling

In this section, the lattice modifications due to lowest order (cubic) anharmonic coupling are discussed. The derivation of the transient lattice structure from the ultrafast hard x-ray experiment is presented.

According to the selection rules derived in section 1.1, the cubic term $Q^2_{B1u}Q_R$ is non zero only if Q_R is of A_g symmetry, because the square of the irreducible representation of B_{1u} is A_g. Thus, to lowest order, only A_g modes can couple to the optically driven B_{1u} motion shown in Figure 4.1.1a. YBa$_2$Cu$_3$O$_{6.5}$ has 72 optical phonon modes, of which 33 are Raman active. These can be further divided into 22 B_g modes, which break in-plane symmetry, and 11 A_g modes, which preserve the symmetry of the unit cell. The geometries of these 11 A_g modes and their coupling strength to the driven B_{1u} mode were computed using first principles DFT calculations within local density approximation. At 3 MV/cm field strength of the mid-infrared pump pulse, a peak amplitude for the B_{1u} motion corresponding to ∼2.2 pm increase in apical oxygen-Cu distance is estimated. Figure 4.1.2a shows the energy potentials of the A_g modes calculated for a frozen B_{1u} distortion of this magnitude.
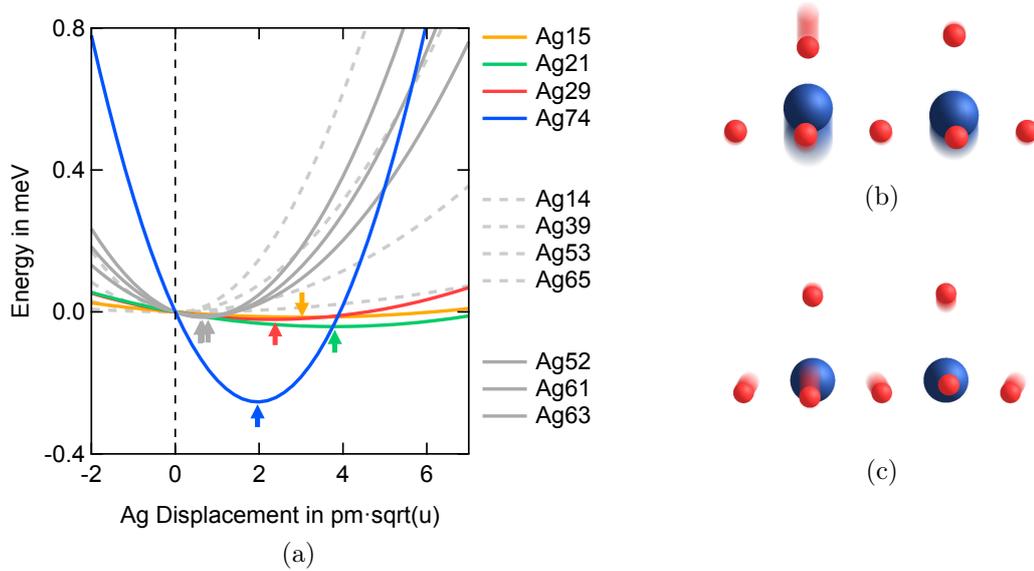
Figure 4.1.2: First-principles calculations of cubic coupling between 11 A_g modes and the driven B_{1u} mode. (a) Energy potentials of all A_g modes for a frozen B_{1u} displacement of 0.14 Å$\sqrt{u}$ (u, atomic mass unit), corresponding to a change in apical O–Cu distance of 2.2 pm. The x axis is the amplitude of the A_g eigenvector. Arrows indicate the potential minima. (b) There is strong coupling to the $A_g(15, 21, 29, 74)$ modes, which involves a decrease in the apical O–Cu distance and an increase in in-plane buckling. (c) The $A_g(52, 61, 63)$ modes are weakly coupled and govern a breathing motion of the oxygen atoms in the CuO_2 plane. The image is taken from [33].

Recalling the discussion in section 1.1, finite cubic coupling results in a shift of the Raman mode energy potential for static displacements of the infrared active mode. The coupling strength is given by the size of the shift away from equilibrium, the slope of the energy potential is defined by the frequency of the respective Raman mode, which is not changed by cubic coupling effects. The calculated displacements of the coupled Raman modes for a B_{1u} excitation amplitude of 0.14 Å$\sqrt{u}$, which corresponds to a change in apical O-Cu distance of 2.2 pm, are given in table 4.1a.

The mode displacements are given in terms of the amplitude Q_i of the dimensionless eigenvectors of the mode and have units of Å$\sqrt{u}$, where u is the atomic mass unit. The atomic displacements due to an amplitude Q_i of a mode are given by $\mathbf{U}_j = \left(Q_i/\sqrt{m_j}\right)\mathbf{e}_{ij}$, where $\mathbf{U}_j$ is the displacement of the jth atom, m_j is the mass of this atom and $\mathbf{e}_{ij}$ is the corresponding component of the normal-mode vector, which is normalized and dimensionless.

Only four phonon modes $A_g(15, 21, 29, 74)$ were found to strongly couple to the driven B_{1u} mode, all involving a concerted distortion of the apical oxygen atoms towards the CuO$_2$ plane and an increase in Cu-O buckling (Figure 4.1.2b). The calculations also predict weak coupling to three further modes $A_g(52, 53, 61)$, consisting of breathing motion of the oxygen atoms in the plane (Fig. 4.1.2c). The remaining four modes $A_g(14, 39, 53, 65)$ do not couple to the B_{1u} mode.

Determination of the transient Lattice Structure

To experimentally determine the absolute amplitude of these displacements in the conditions relevant for enhanced superconductivity [7, 8], we measured time resolved x-ray diffraction using 50 fs, 6.7 keV pulses from the Linac Coherent Light Source (LCLS) free electron laser, which was synchronized to the optical laser that generated the mid-infrared pump pulses (see Appendix C for details on the experimental setup and the analysis of the data). Changes in diffraction intensity were recorded for four Bragg peaks at a base temperature of 100 K, above the equilibrium transition temperature $T_c = 52$ K.
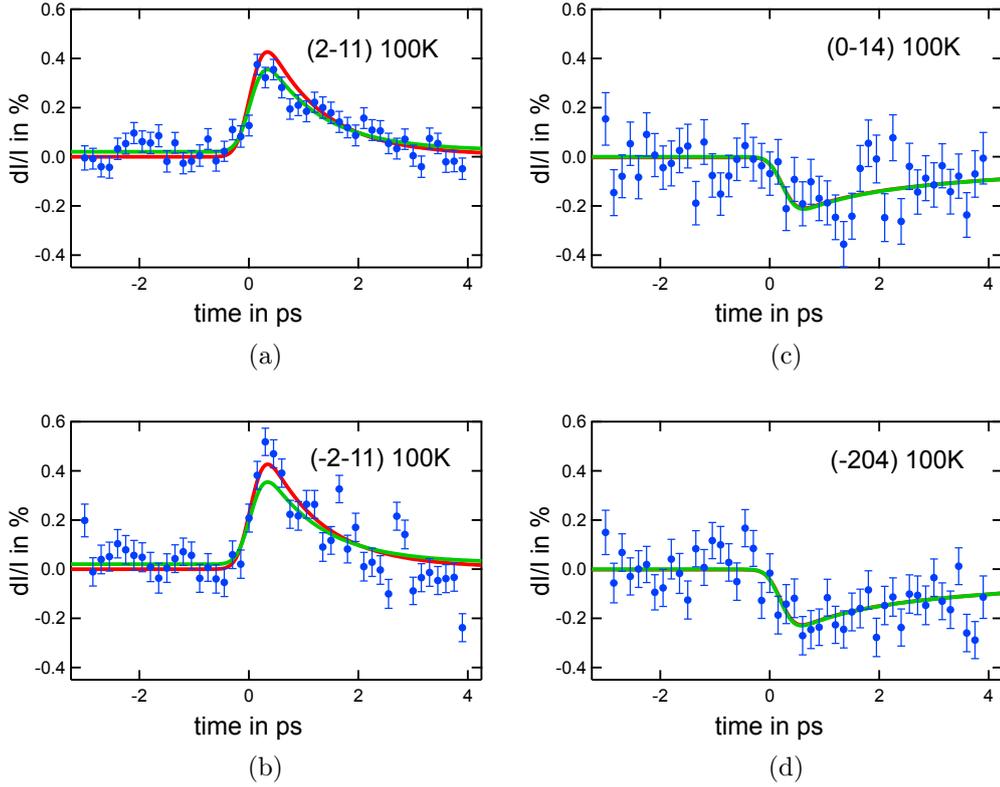
Figure 4.1.3: Time-dependent changes in diffracted peak intensity $\Delta I/I$ for four Bragg reflections. A displacive lattice distortion is observed. The experimental data are fitted (solid curves) by adjusting the B_{1u} amplitude and the relative strength of the two relaxation channels ($\tau_1 = 1$ ps, $\tau_2 = 7$ ps) extracted from the optical experiments of refs [7, 8]. The relative amplitudes and signs of the curves are determined from the calculated structure using only the four most strongly coupled modes (green) or all Ag modes (red). The error bars are extracted from the measurements as 1-σ (67% confidence interval). The Figure is taken from [33].

Mode	Q_0 Positions (Å$\sqrt{u}$)	(0-14)	(-204)	(-2-11)	(-211)
Ag14	-0.002	-0.8	-0.9	1.8	1.8
Ag15	**0.031**	-20.0	-21.8	25.4	25.4
Ag21	**-0.038**	-13.2	-14.4	9.4	9.4
Ag29	**-0.023**	1.6	1.6	-3.4	-3.4
Ag39	0.000	-0.2	-0.3	0.7	0.7
Ag52	0.007	0.9	0.9	0.0	0.0
Ag53	0.000	-1.3	1.1	0.7	0.7
Ag61	-0.007	3.0	3.3	-7.8	-7.8
Ag63	0.007	3.2	3.6	7.8	7.8
Ag65	-0.001	2.2	2.5	3.8	3.8
Ag74	**0.020**	-3.9	-4.3	-7.1	-7.1
(a)			(b)		

Table 4.1: (a) Positions of the A_g mode energy potential minima Q_0 as obtained from DFT calculations for a frozen displacement of the B_{1u} mode of 0.14 Å$\sqrt{u}$ (b) Calculated changes in diffraction intensity for A_g mode displacements of 1 Å$\sqrt{u}$ given in percent (for details see Appendix C.1.1)

These peaks were observed to either increase or decrease promptly after excitation (see Figure 4.1.3) and to relax within the same timescale as the changes in the THz optical properties [7, 8]. As shown in Appendix C.2, the intensity decreases homogeneously across the Bragg peak, excluding a shift of the peak as cause for the intensity change. For each Bragg reflection, changes in diffraction were calculated as function of B_{1u} amplitude considering a displacement of only the four dominant Raman modes A_g(15, 21, 29, 74) or all 11 modes of Figure 4.1.2a, taking into account the relative coupling strengths. To first order, changes in the structure factor are linear in the displacement amplitude A_g. Table 4.1b holds the changes in diffraction intensity due to A_g displacements of 1 Å$\sqrt{u}$. The four experimental diffraction curves were simultaneously fitted using only two free parameters: the amplitude of the directly driven B_{1u} motion and the relative contributions of two exponential relaxation components ($\tau_1 = 1$ ps, $\tau_2 = 7$ ps) extracted from the THz measurements [7, 8]. Very similar results were found when considering only the four dominant modes or all modes (see green and red fitting curves in Figure 4.1.3).
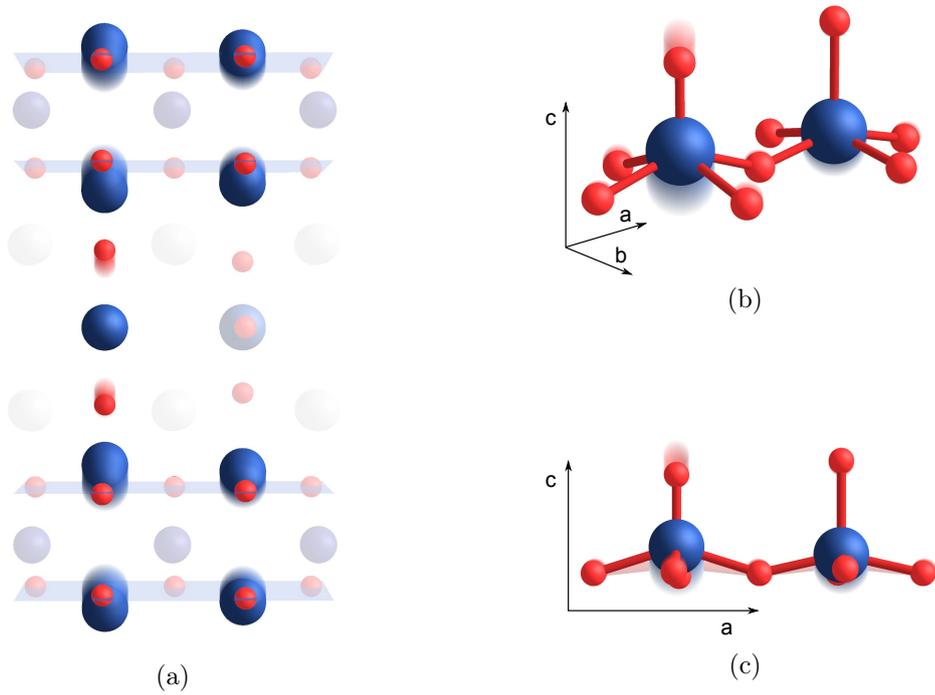
Figure 4.1.4: (a) Transient lattice structure of $YBa_2Cu_3O_{6.5}$ at peak amplitude of the lattice displacements. The displacive lattice distortion involves a decrease in the apical O–Cu distances by 2.4 pm at O-deficient sites and an increase in O–Cu–O buckling (b, c). The images are taken from [33].
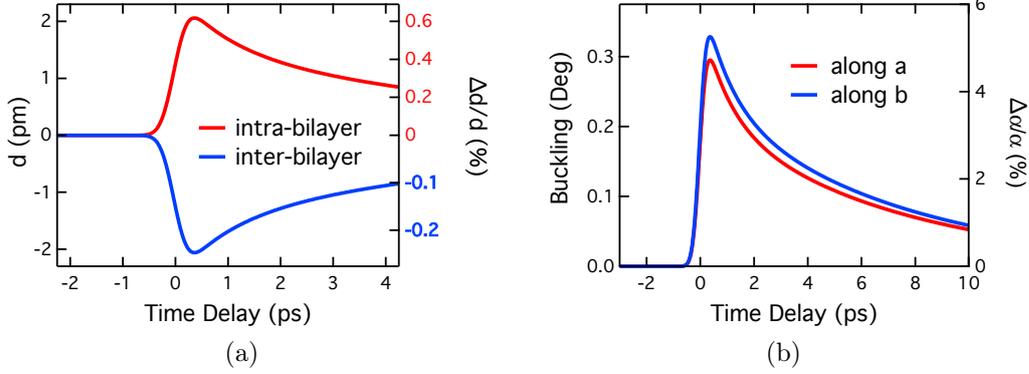
Figure 4.1.5: (a) The intrabilayer distance increases and the interbilayer distance decreases. Here, the copper atoms of the planes at O-deficient chain sites (left side in Figure 4.1.4a) are used to define the positions of the planes. (b) The in-plane buckling angle α of the O–Cu–O bond increases by 5% along both crystallographic **a** and **b** directions at oxygen-deficient sites. The images are taken from [33].

The transient lattice structure determined from these fits involves the following elements. Firstly, a decrease in the distance between the apical oxygen and the copper atoms of the superconducting planes is found (Figure 4.1.4). This motion is far smaller and opposite in sign than the difference in the static apical oxygen positions between La- and Hg-based cuprates, for which T_c increases at equilibrium. Therefore, the transient enhancement of super-conducting transport cannot be explained by this analogy. More suggestively, the copper atoms are driven away from one another within the bilayers and toward one another between different bilayers. This staggered motion is of approximately 0.63% (see Figure 4.1.5) and qualitatively follows the decrease in intrabilayer tunneling and the enhancement of interbilayer tunneling [7, 8]. Finally, an anisotropic 0.32° increase in the in-plane O-Cu-O buckling, which is larger at oxygen deficient sites, is observed.

4.1.2   Quartic order coupling

To verify that the nonlinear phonon coupling is dominated by the third-order contribution, we checked for signals at the next (fourth) order, described by

the term $Q_{ir}^2 Q_{\mathbf{q},j}^2$. As noted before, when the directly driven infrared mode is of B_{1u} symmetry, the only modes to which there is non-zero third-order coupling are those of A_g symmetry. However, coupling to any mode $Q_{\mathbf{q},j}$, in particular to in-plane B_g modes, is allowed through $Q^2 Q^2$ coupling. As described in section 1.2, small-amplitude B_{1u} excitations would simply renormalize the frequency of a second mode $Q_{\mathbf{q},j}$. This can be directly deduced from the equation of motion, where the driving force is given by the coupling term $a_{22} Q_{ir}^2 Q_{\mathbf{q},j}$, which is linear in $Q_{\mathbf{q},j}$:

$$\ddot{Q}_{\mathbf{q},j} + 2\gamma_{\mathbf{q},j}\dot{Q}_{\mathbf{q},j} + \omega_{\mathbf{q},j}^2 Q_{\mathbf{q},j} = 2a_{22} Q_{ir}^2 Q_{\mathbf{q},j}.$$

On Q_{ir} displacement, the anharmonically coupled mode experiences a renormalization of its frequency $\omega'_{\mathbf{q},j} = \sqrt{\omega_{\mathbf{q},j}^2 - 2a_{22} Q_{ir}^2}$. However, above a threshold amplitude, the frequency of the second mode $Q_{\mathbf{q},j}$ becomes imaginary and the lattice becomes unstable. Importantly, such instability can take place in two directions, depending on the random instantaneous state of the system (mode amplitude $Q_{\mathbf{q},j}$ and its velocity $dQ_{\mathbf{q},j}/dt$), which manifests in a change from a parabolic to a double-well energy potential.

Hence, fourth-order effects need to be identified by analyzing the diffraction of each individual x-ray pulse, whereas the unsorted average is expected to be zero even if the quartic coupling is sizable. In the experiment, all positive and negative deviations from the average signal of all shots were sorted to obtain the $Q^2 Q^2$ response at a specific time delay. Averaging them separately and subtracting negative deviations from positive then gives the intensity changes from $Q^2 Q^2$ only (see Appendix C.1.5 for more details). Time-resolved x-ray diffraction was measured for four Bragg reflections, sensitive to A_g and to B_g displacements. The results of these experiments are shown in Figure 4.1.6. Within the resolution of the experiment, no evidence of fourth order contributions to the phonon coupling was found. The amplitude of the infrared motion is below the threshold beyond which fourth-order coupling induces lattice displacements.
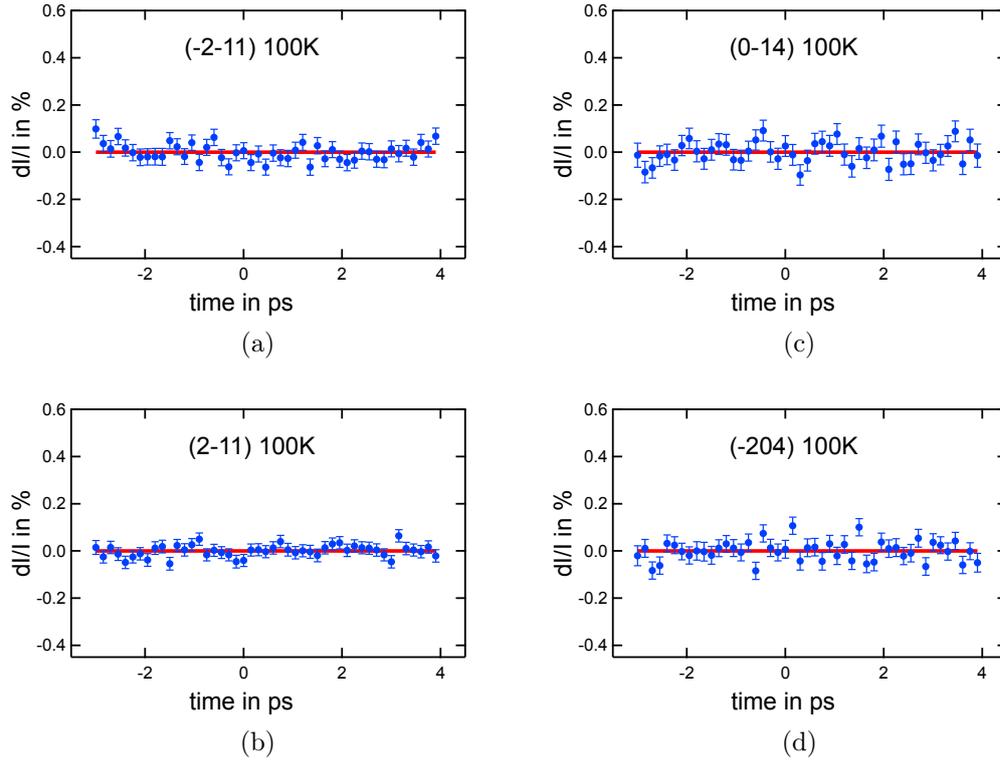
Figure 4.1.6: Time-dependent changes of diffracted peak intensity $\Delta I/I$ of specific Bragg reflections from fourth-order coupling. Within the resolution of the experiment, no evidence of fourth order contributions to the phonon coupling was found. The amplitude of the B_{1u} infrared mode is below the threshold, beyond which fourth-order effects destabilize coupled phonon modes. The error bars are extracted from the measurements as 1-σ (67% confidence interval). The Figure is taken from [33].

4.2 Transient electronic structure

As no evidence of lattice displacements due to higher order effects were found, the transient structure presented in section 4.1.1 can be used as basis for further studies. While the microscopic interactions are not fully captured by Density Functional Theory (DFT) within local density approximation, the calculated electronic band structure and fermi surfaces in the equilibrium structure show very good agreement with Angle Resolved Photoemission (ARPES) measurements. The salient effects on electronic properties can thus be assessed from DFT calculations in the transient crystal structure (see Appendix C.3 for details on the DFT calculations). Results of these calculations are presented for the equilibrium structure and the transient displaced structure for three B_{1u} amplitudes: the amplitude 0.3 Å$\sqrt{u}$ determined here, the amplitude 0.8 Å$\sqrt{u}$ estimated in references [7, 8], and a larger amplitude of 1.2 Å$\sqrt{u}$ to show trends with increasing lattice displacements. The calculated band structure and fermi surface of the equilibrium $YBa_2Cu_3O_{6.5}$ ortho-II structure, shown in Figures 4.2.1 and 4.2.2, agree well with previously published results [77, 78].

The bands near the Fermi level are derived from the $3d$ states of copper atoms from both the planes and the chains. As the 1-dimensional chains run along the crystallographic **b** direction, bands due to the chain copper atoms have almost no dispersion along k_x and k_z, which is clearly visible in the calculated band structure. The Cu d_{z^2} states of the filled chains yield a broad band with very little dispersion along the paths $\Gamma(0,0,0) \rightarrow X(0.5,0,0)$ and $S(0,5,0.5,0) \rightarrow Y(0,0.5,0)$, both involving changes only in k_x. On the opposite, very large dispersion is observed along paths that involve changes in k_y such as $X(0.5,0,0) \rightarrow S(0.5,0.5,0)$ and $Y(0,0.5,0) \rightarrow \Gamma(0,0,0)$. The oxygen-deficient chains give rise to fairly flat electronic bands with dominant Cu d_{xz} and d_{yz} character that are very close to the Fermi level at the Y-point. The electronic structure calculations predict some hybridization between these bands and the planar Cu bands, which creates an anticrossing near Y, marked by a light blue circle in Figure 4.2.1.
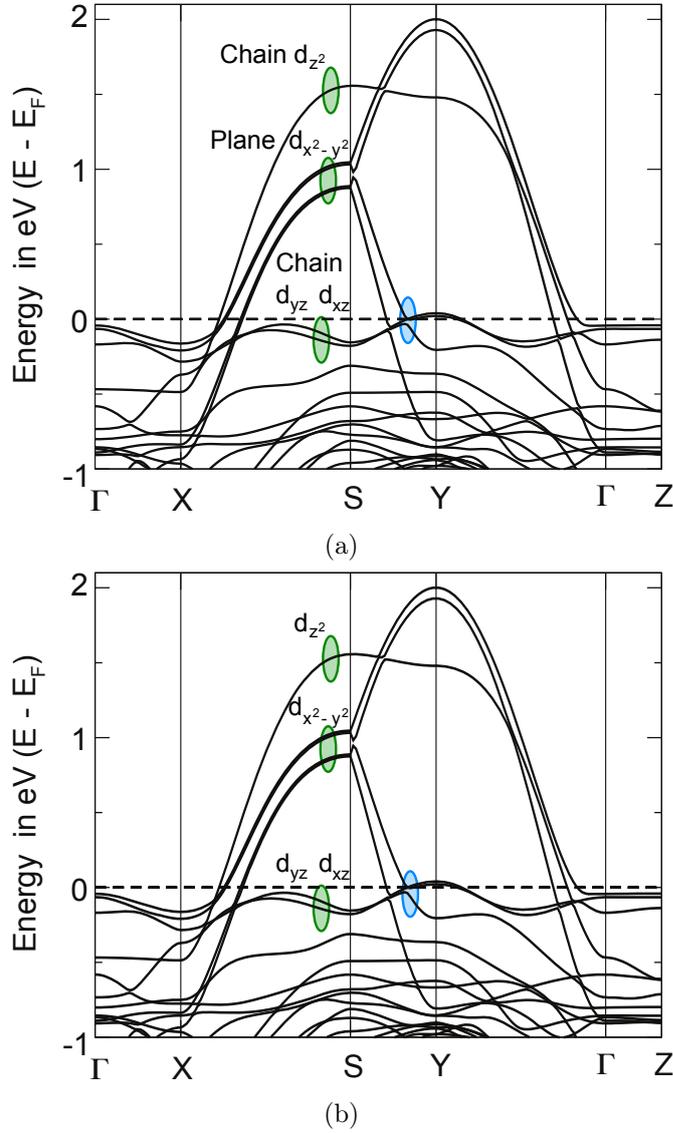
Figure 4.2.1: Band structure of the equilibrium (black line) and transient crystal structure (red dashed). The bands from the 1-dimensional chains are due to Cu d_{z^2} and Cu d_{xz}, d_{yz} states, for filled and oxygen-deficient chains respectively. The bands from planar Cu atoms are due to $d_{x^2-y^2}$ states. In the equilibrium structure, there is an anticrossing close to the Fermi level between the planar and the empty chain Cu bands marked in light blue, which shifts to lower energies with increasing lattice displacements. The band structure is plotted along $\Gamma\,(0,0,0) \rightarrow X\,(0.5,0,0) \rightarrow S\,(0,5,0.5,0) \rightarrow Y\,(0,0.5,0) \rightarrow \Gamma\,(0,0,0) \rightarrow Z\,(0,0,0.5)$ for transient displaced structures corresponding to B_{1u} amplitudes of 0.8 Å$\sqrt{u}$ (a), which is the amplitude estimated for the geometry of references [7, 8], and 1.2 Å$\sqrt{u}$ (b). The images are adapted from [33].

89
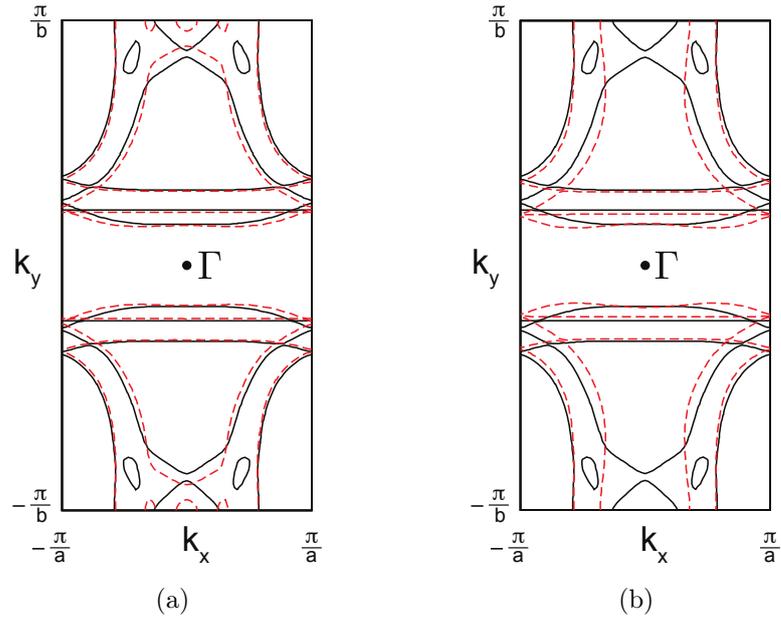
Figure 4.2.2: Cuts of the Fermi surface of the equilibrium (black line) and transient crystal structures (red dashed line) at $k_z = 0$. In the equilibrium structure, the bands of the unfilled chain copper atoms give rise to pockets in the Fermi surface. The light induced displacements shift the densities of states of these bands to lower energies, increasing the filling and reducing the pockets. Above a threshold of 0.8 Å$\sqrt{u}$, the oxygen-deficient chain bands become fully filled, the pockets close and the Fermi surface consists solely of two-dimensional planar Cu sheets and one-dimensional filled-chain states. The Fermi surface is shown in the displaced state for B_{1u} amplitudes of 0.8 Å$\sqrt{u}$ (left) and 1.2 Å$\sqrt{u}$ (right). The images are adapted from [33].

In the equilibrium structure, this anticrossing is close to the Fermi level, giving rise to pockets with unfilled-chain Cu character in the Fermi surface, consistent with Shubnikov–de Haas oscillations found in Hall measurements [78, 79]. As the band is only slightly above the Fermi level, the size of these hole pockets is highly sensitive to the energy position of the band.

The displacements due to the nonlinear couplings cause noticeable changes to the electronic structure around the Fermi level. There are three main effects.

1. The light-induced displacements reduce the width of the planar Cu bands, which leads to a narrowing and increase in the planar Cu contribution to the density of states at the Fermi level. This effect is most clearly seen in panels b and d of Figure 4.2.3.

2. The atomic displacements cause a transfer of charge from the planes to the O-deficient chains. While the unfilled Cu chain bands decrease in energy and move below the Fermi level with increasing light-induced displacements, the planar Cu states increase in energy, becoming less occupied. This charge redistribution results in an effective hole doping of the planar Cu states due to the light-induced displacements (Figure 4.2.3).

3. The changes in the relative occupations of the bands also cause a topological change in the Fermi surface shown in Figure 4.2.2. As mentioned in point 2., the oxygen-deficient chain bands decrease in energy, which reduces the size of the pockets in the Fermi surface. Above a threshold B_{1u} amplitude of 0.8 Å$\sqrt{u}$, the O-deficient chain Cu bands move below the Fermi energy and become fully filled. The Fermi surface is then solely composed of Cu d-bands from the two-dimensional CuO$_2$ planes and one-dimensional filled Cu-O chains.
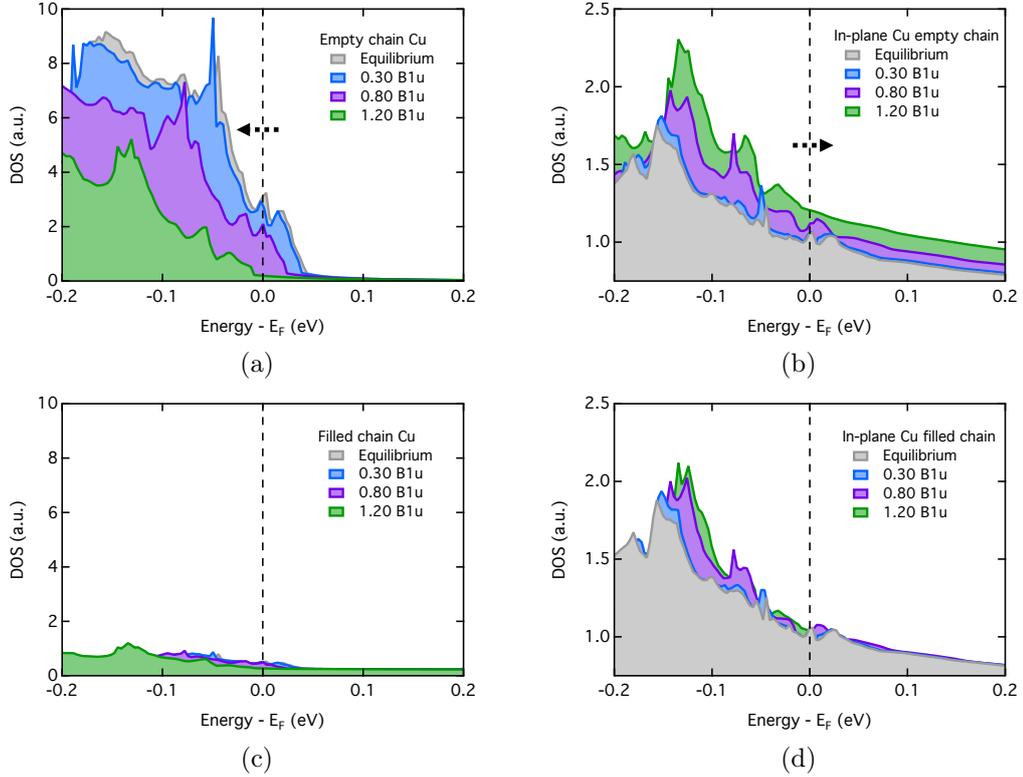
Figure 4.2.3: Changes in the density of states in the CuO_2 plane and the Cu–O chains. These are obtained from a projection of the density of states onto the copper muffin-tin spheres. (a), (b) In the light-induced state, the density of states of the O-deficient chain copper atoms lowers in energy (a), whereas the opposite effect is observed for the Cu in the plane below (b). This corresponds to charge transfer from the planes to the chains. (c), (d) The density of states of the filled chain Cu is not as strongly affected (c). The bands of the planar Cu atoms narrow, which leads to an increase in the density of states near the Fermi level both at sites with filled (d) and empty chains (b). The effect is already visible for a B_{1u} amplitude of 0.3 $\text{Å}\sqrt{u}$ (blue) but becomes more prominent for larger displacements of 0.8 $\text{Å}\sqrt{u}$ (purple) and 1.2 $\text{Å}\sqrt{u}$ (green). The Figure is taken from [33].

4.3   Summary

Following the resonant excitation of the B_{1u} infrared-active mode, atomic displacements along A_g coordinates into a transient structure take place, which relaxes back to the equilibrium structure with the same timescales found in the preceding optical experiments. The copper atoms are driven away from one another within bilayers and toward one another between different bilayers. This motion is of approximately 0.63% for a fluence of $4\mathrm{mJ/cm^2}$ and qualitatively follows the decrease in intrabilayer tunneling and the enhancement of interbilayer tunneling. This intuitive picture is supported by a recent publication, in which the effect of the structural changes presented in this work including the periodic motion of the infrared-active mode on superconductivity and charge density wave order was studied. It was found that the lattice excitation leads to an enhancement of superconductivity, increasing T_c by up to 100% and suppressing charge density wave order [34]. Partial melting of charge order has indeed been experimentally shown to follow the same lattice excitation [80].

Density functional calculations have shown that the lattice dynamics force an electron transfer from the CuO_2 planes to the Chain sites, effectively increasing the hole doping of the planes. This self-doping effect was found recently to accompany the temperature-driven metal-superconductor transition in optimally doped $YBa_2Cu_3O_{6.9}$ [81] and might emerge as a key process in the superconducting transition. The calculations further predict an energy lowering of the oxygen deficient chain bands by few tens of meV. Because at equilibrium these bands are very close to the Fermi level, this small shift strongly reduces the hybridization of the chains with the planar Cu orbitals, leading to a Fermi surface with a stronger Cu $d_{x^2-y^2}$ character, which is likely to favor superconductivity. These results are visualized in Figure 4.3.1. Future experiments could investigate the charge transfer dynamics by time-resolved x-ray absorption to verify these predictions. Further, to make a definite connection to the equilibrium charge redistribution, the temperature and magnetic field dependent charge transfer dynamics of underdoped samples have to be measured, as the study by Magnuson et al. concentrated

on an optimally doped sample. At optimal doping, all Cu-O chains are filled and the experimentally driven phonon mode at 670cm^{-1}, which is associated with apical oxygen motions at empty chain sites, does not exist [35].
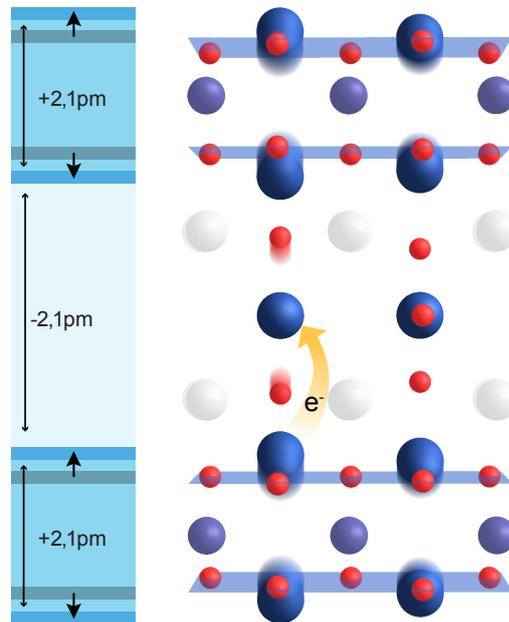

Figure 4.3.1: The light-induced lattice dynamics entail an increase in inter-bilayer coupling and an electron transfer from the CuO$_2$ planes to the chains, increasing the hole doping of the planes. The image is adapted from [40, 61].

Chapter 5

Concomitant coherent lattice dynamics

In the study presented above, we successfully determined the transient lattice structure of $YBa_2Cu_3O_{6.5}$ underlying the enhancement of superconductivity. However, due to the limited time resolution of ~ 250 fs, the coherent response of the lattice could not be resolved. As discussed in section 1.1.3, cubic anharmonicities involve a displacive force that acts onto the crystal lattice in two ways. First, a phononic analog to rectification in nonlinear optics causes a quasistatic displacement along the normal mode coordinates of all coupled Raman modes. Secondly, whenever the displacive force rises promptly compared to the period of any of the anharmonically coupled modes, coherent oscillatory motions of these modes are excited. This second effect is the stimulated equivalent of ionic Raman scattering.

In this chapter, the coherent response of $YBa_2Cu_3O_{6+x}$ is discussed. The same infrared-active apical oxygen motions of Figure 4.1.1a are driven resonantly with mid-infrared pulses at 20 THz, under the conditions for which superconducting transport is transiently enhanced [7, 8, 33]. For excitation with pulses of 140 fs duration, for which only modes with frequency < 6 THz can be driven coherently, oscillations of four Raman modes were observed, involving displacements of the copper atoms along the crystallographic **c** axis. This motion induces periodic changes in the in-plane O-Cu bond buckling and might lead to an oscillatory transfer of charges between the CuO_2 planes

and the Cu-O chains [33], modifying the doping of the planes. Parts of this Chapter are taken from Ref. [40].

5.1 Generation of coherent phonons

In the following, experiments performed on $YBa_2Cu_3O_{6.5}$ and $YBa_2Cu_3O_{6.55}$, two bilayer high-temperature superconductors with respective critical temperatures of Tc = 50 K and Tc = 61 K, are discussed. These two compounds crystallize in the orthorhombic structure of YBCO presented in the previous chapter. The samples exhibited ortho-II ordering of the oxygen atoms, corresponding to a structure for which alternate Cu-O chains are filled and empty. The $YBa_2Cu_3O_{6.5}$ sample exhibited only short-range ordered domains, whereas the $YBa_2Cu_3O_{6.55}$ samples showed long-range ordering of these chains [63]. As the resonantly excited B_{1u} symmetry mode at 20 THz of Figure 4.1.1a consists of movements of the apical oxygen atoms between bilayers at vacant chain sites only [35], the long-range ordering of the chain vacancies in the $YBa_2Cu_3O_{6.55}$ sample might influence the structural dynamics. According to the symmetry argument discussed in the previous chapter, cubic coupling is restricted to Raman modes of A_g symmetry.

Probing coherent Raman vibrations

Because atomic motions along Raman coordinates modulate the polarizability tensor, these motions become observable as changes in the reflectivity of the material. 140 fs mid-infrared pulses (15 µm, 10% bandwidth) with a fluence of 2.5 mJ/cm^2 were used to drive the sample into its transient state. Time-resolved changes in the reflectivity were probed with 35 fs pulses at 800nm wavelength. Under these conditions, modes up to $\sim$6 THz in frequency can be excited to coherent oscillations. The Raman Tensor of the A_g modes in the orthorhombic D_{2h} point group is given by

$$\chi_{Ag} = \begin{pmatrix} a & 0 & 0 \\ 0 & b & 0 \\ 0 & 0 & c \end{pmatrix}.$$

According to their Raman tensor, the A_g Raman modes are observable but have different tensor elements for probe polarizations in-plane along **a** and **b**, as well as out of plane along the **c** direction. While the phase is expected to be the same for oscillations probed with light polarized along different crystallographic axis, their amplitudes can be different. Details on the experimental setup can be found in Appendix B.

Results

The experimental results, reported for both out-of-plane and in-plane polarized probe pulses, are shown in Figure 5.1.1a for $YBa_2Cu_3O_{6.55}$. The oscillatory response was obtained by subtracting a fit to the data consisting of an error function and a triple-exponential decay (thin black line) and is shown in the inset for 10K sample temperature. While sign and size of the total response are different for the two orthogonal polarizations, there is no difference between the amplitudes and absolute phases of the oscillations. For $YBa_2Cu_3O_{6.55}$ and $YBa_2Cu_3O_{6.5}$, the oscillatory response comprises three dominant frequency components (see panels (b) and (d) of Figure 5.1.1), which can be attributed to four A_g phonon modes (A_g14, 15, 21, and 29) that are shown in Figure 5.1.2a. The numbers denote the index of the respective phonon modes, sorted according to their frequencies. We find no significant differences in the response to the excitation between the two samples.

The same oscillatory modes were also observed in $YBa_2Cu_3O_{6.9}$ after excitation with 2 eV pulses [82, 83, 84]. In these experiments, large changes were found in the relative amplitudes of these modes and relaxation dynamics when crossing the critical temperature T_c, as the excitation mechanism relied on optical transitions between electronic states that strongly change through the superconducting transition. Here, we only find a continuous increase in both phonon amplitudes and non-oscillatory components upon decreasing temperature, as only small changes in the equilibrium infrared phonon spectrum of the excited B_{1u} mode take place at T_c. This observation shows the fundamental difference between the ionic and electronic Raman scattering process.
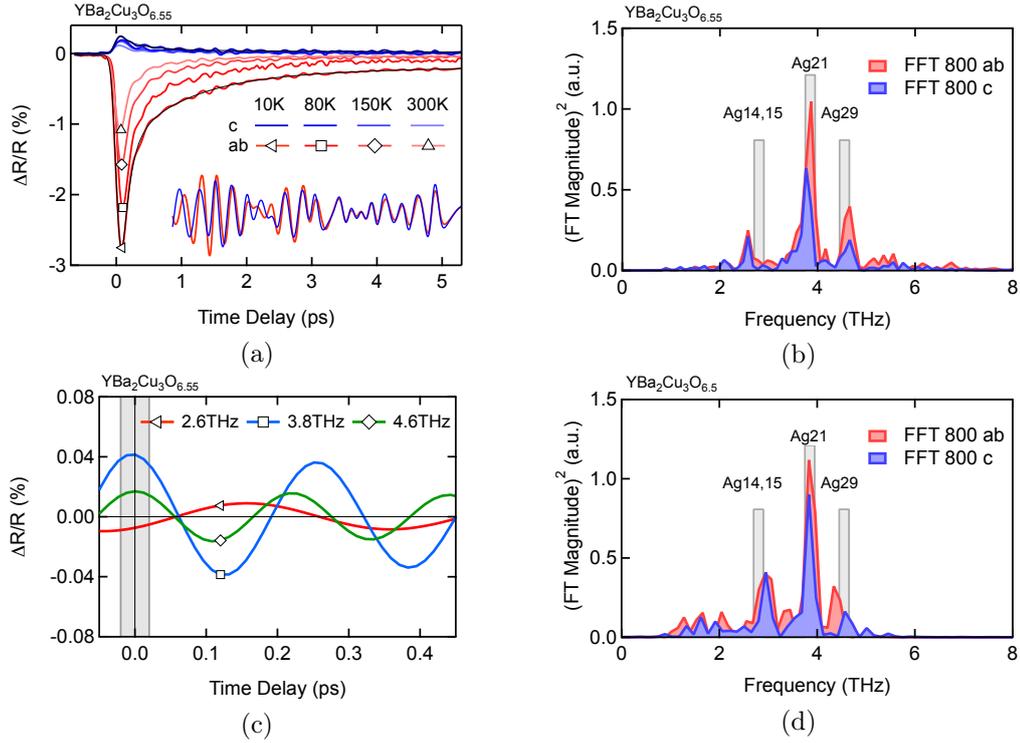
Figure 5.1.1: (a) Time-resolved reflectivity changes at 800 nm following resonant excitation of the B_{1u} infrared mode in $YBa_2Cu_3O_{6.55}$. Changes for probe polarizations out of plane and in plane are shown in blue and red, respectively. The inset shows the oscillatory signal at 10 K sample temperature, obtained by subtracting a fit to the data (thin black line). (b) The Fourier transformations of these oscillations, showing spectral weight at four frequencies coinciding with Ag phonon modes. (d) Same as panel (b) for $YBa_2Cu_3O_{6.5}$. (c) Zoom into the individual oscillatory components in $YBa_2Cu_3O_{6.55}$ (10 K, in plane), extracted from fitting the oscillations shown in panel (a). The phase of the oscillatory components at time zero is cosine-like. The Figure is taken from [40].
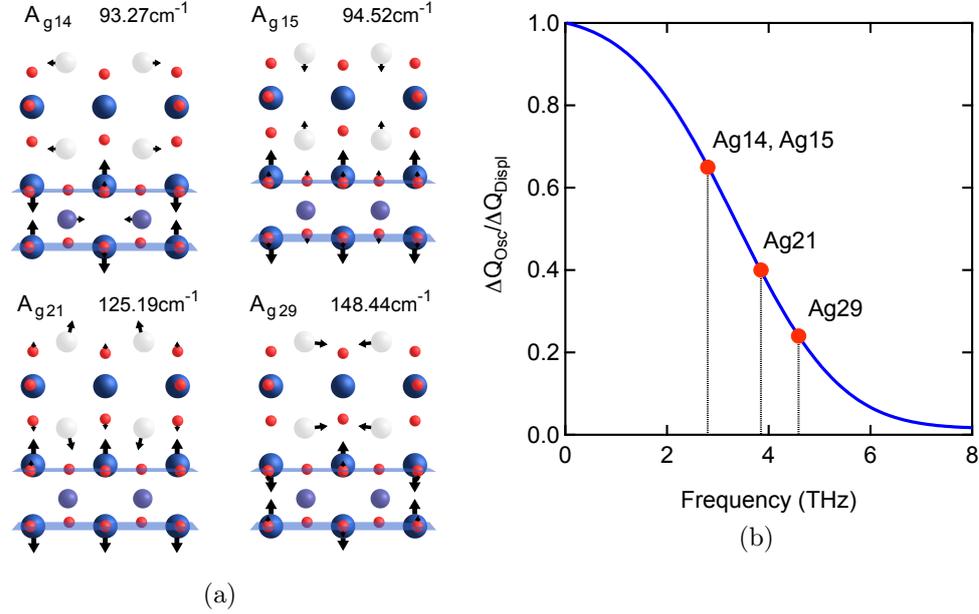
Figure 5.1.2: (a) Four lowest frequency Ag modes of the ortho-II ordered $YBa_2Cu_3O_{6+x}$ structure [33]. (b) Calculated ratio between oscillation and displacement amplitudes of these modes after excitation of the B_{1u} infrared mode with 140 fs mid-infrared pulses. The Figure is taken from [40].

The observed oscillations at 2.6, 3.8, and 4.6 THz in $YBa_2Cu_3O_{6.55}$ are shown in Figure 5.1.1c, displaying a clear cosine phase at time zero (black line; gray area is the uncertainty), indicative of a displacive rather than an impulsive mechanism ($T_R \ll \tau_{ir}$). This result can be validated by estimating the relaxation time of the IR mode τ_{ir} from the decay time of the atomic displacements τ_D which has been measured by x-ray diffraction [33] (see previous chapter), using the relation $\tau_{ir} = 2\tau_D$. This estimation yields a relaxation time of $\tau_{ir} = 2.4$ ps, which is larger by factors of 11, 9, and 6 compared to the periods of the observed oscillations at 2.6, 3.8, and 4.6 THz, respectively, consistent with a displacive excitation. We can attribute these oscillations to the four lowest frequency Ag modes of the ortho-II ordered $YBa_2Cu_3O_{6+x}$ structure. From the presented data alone, the amplitudes of the atomic motions cannot be quantified as the changes in the electronic polarizability at 800 nm may be different for each mode and are not known here [43].

5.2   Estimation of real-space amplitudes

A qualitative estimate of the real-space amplitudes can however be obtained by starting from the measurements of the underlying rectified displacement by ultrafast hard x-ray diffraction of the previous chapter. For the 140 fs mid-infrared pulses used to drive the odd apical oxygen mode, the relative amplitude of oscillatory and displacive responses only depends on the Raman mode frequency and can be calculated from the coupled differential equations (Equations 1.1.1 and 1.1.2). The relative amplitudes of oscillatory and displacive responses of the four A_g modes are shown in Figure 5.1.2b. From these calculations and the displacement amplitudes $\Delta d_{\mathrm{Displ}}$ of the four A_g modes we estimate the oscillatory amplitudes Δd_{Osc} of the respective vibrations for the same fluence of references [7, 8, 33] of $4\mathrm{mJ/cm}^2$ by $\Delta d_{\mathrm{Osc}} = \Delta d_{\mathrm{Displ}}\left(\Delta Q_{\mathrm{Osc}}/\Delta Q_{\mathrm{Displ}}\right)$ (see Table 5.1). The atomic motions of these modes are dominated by a change in distance between Cu atoms of neighboring CuO_2 planes along the crystallographic c axis (see Figure 5.2.1c). We estimate oscillation amplitudes in these distances of $\sim$0.9 and $\sim$0.5 pm at vacant (d_1) and filled (d_2) chain sites, relaxing with a decay time of 3 ps, as shown in Figure 5.2.1a.

mode	$\Delta d_{1,\mathrm{Displ}}$ (pm)	$\Delta d_{1,\mathrm{Displ}}$ (pm)	Frequency (THz)	$\Delta Q_{\mathrm{Osc}}/\Delta Q_{\mathrm{Displ}}$
A_g 14	0.29	-0.30	2.80	0.64
A_g 15	0.81	0.76	2.83	0.64
A_g 21	0.73	0.63	3.85	0.40
A_g 29	0.24	-0.34	4.59	0.24

Table 5.1: Numbers used for the estimation of the real-space amplitudes of the A_g modes oscillatory motion given in the distances d_1 and d_2 (see Figure 5.2.1c). The frequencies and displacement amplitudes $\Delta d_{\mathrm{Displ}}$ of the A_g modes are taken from the density functional theory calculations for $YBa_2Cu_3O_{6.5}$ described in the previous chapter. The relative amplitudes of oscillatory and displacive components $\Delta Q_{\mathrm{Osc}}/\Delta Q_{\mathrm{Displ}}$, are calculated from Eqs. (1.1.1) and (1.1.2) for 140 fs pump pulses.
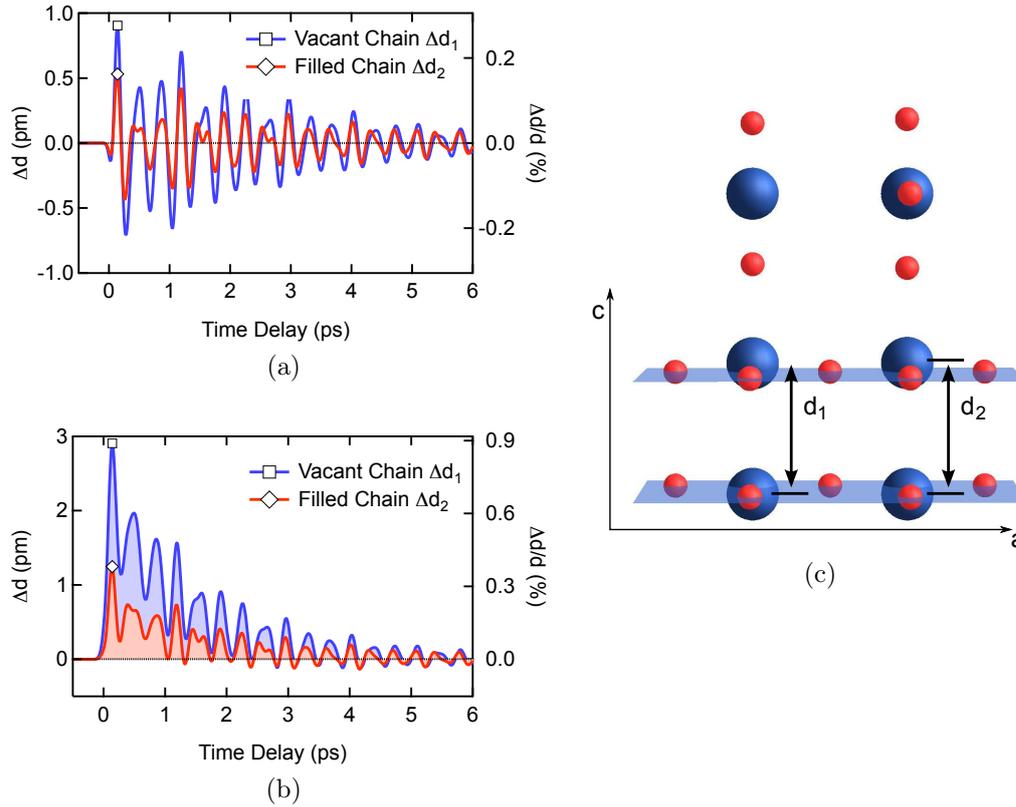
Figure 5.2.1: (a) The combined atomic motions of the A_g modes primarily involve c-axis movement of the planar Cu atoms. To describe the structural dynamics, we define d_1 and d_2 as the distances between Cu atoms (large blue spheres) of neighboring CuO_2 planes at vacant and filled chain sites, respectively. (b) Changes in these distances due to excitation of the Ag phonon modes. The estimation described in the text yields oscillation amplitudes of 0.9 and 0.5 pm in d_1 and d_2 with a relaxation time of 3 ps. (c) The full dynamics including the displacive response involve an increase in both d_1 and d_2 accompanied by oscillations. The Figure is taken from [40].

Figure 5.2.1b shows the full lattice dynamics underlying the light induced enhancement of interlayer coupling, including both oscillatory and displacive response. As presented in the previous chapter, the displacive motion likely increases the interlayer coupling at the expense of intrabilayer coupling and forces a charge transfer from the CuO_2 planes to the Cu-O chains, effectively increasing the hole doping of the planes. The connection of the oscillatory motions to the light induced enhancement of superconductivity can be discussed assuming a similar effect on the physical properties, that is a periodic modulation of Josephson coupling and the planar hole doping. In a recent theoretical paper, it was discussed how the periodic modulation of the interlayer coupling may cause a reduction and parametric cooling of phase fluctuations [85]. This effect was found to be strongest for modulations of the coupling at half the difference frequency ω_d between the Josephson plasma frequencies of the intra- and interbilayer junctions, which in $YBa_2Cu_3O_{6.5}$ are $\sim$13 THz and $\sim$1 THz, respectively. While the optimal modulation frequency is $\omega_d \approx 12$ THz, the oscillatory motions were found here to be strongest at $\sim$4 THz with an approximate amplitude three times smaller than the displacive response. Thus, strong effects on the enhancement of superconductivity are unlikely and no clear connection can be established. Yet, it cannot be excluded that the coherently driven modes may cause a dynamical stabilization of interlayer coupling by other mechanisms, which may include the periodic modulation of electronic properties [86].

5.3 Summary

In the experiment discussed in the previous chapter, the resonant excitation of the B_{1u} infrared-active mode in $YBa_2Cu_3O_{6.5}$, which has been shown in the past to enhance the interlayer superconducting coupling, was found to be accompanied by atomic displacements along A_g coordinates into a transient crystal structure. According to the model of nonlinear phononics, a subset of these A_g modes with eigenperiods long compared to the mid-infrared pulse duration are excited to coherent oscillations by impulsive stimulated ionic Raman scattering. In the optical experiments presented here, coherent os-

cillations that can be attributed to the four lowest frequency A_g modes were observed with phases consistent with a displacive excitation mechanism. The periodic motions associated with these modes involve c-axis movements of the planar Cu atoms to estimated amplitudes of 0.9pm, which is one third of the displacive response. No direct connection between the coherently excited phonons and the enhancement of superconductivity can be established. However, a dynamical stabilization of interbilayer coupling or the cooling of phase fluctuations through periodic modulations of electronic properties such as the hole doping of the CuO_2 planes cannot be excluded. With the results presented in this and the previous chapter, the full structural dynamics underlying the light-induced enhancement of superconductivity have been determined and quantified. They can serve as basis for future theoretical studies to investigate their effect on superconductivity.

Conclusion

Resonant excitation of infrared-active vibrational modes with light pulses at THz frequencies is a valuable tool for the phase control of strongly correlated materials. Insulator-metal transitions, melting of magnetic order and even induced superconducting behavior had been found to follow this direct lattice excitation [9, 11, 6, 7, 8, 10]. An understanding of the microscopic mechanism, by which these transitions are driven, had however been missing. The aim of this work was to uncover this process by investigating the nonlinear lattice dynamics induced by the excitation and to elucidate their contribution to the modulation of collective properties of strongly correlated materials.

The first signature of nonlinear lattice dynamics was reported in the observation of coherent phonon oscillations of a Raman active mode following excitation of $La_{0.7}Sr_{0.3}MnO_3$ with mid-infrared light pulses [22]. The amplitude of these oscillations peaked, when the mid-infrared pulses were tuned to resonance with an infrared-active phonon mode. This oscillatory response can be explained by a model involving nonlinear phonon coupling, which further predicts a displacive response of the atoms along the coupled phonon mode. The transformation of vibrational atomic motions into directional changes of the crystal structure *on average* might be the cause for the previously observed phase transitions.

We verified this directional response and quantified the anharmonic coupling constant by tracing the atomic motions in a time-resolved hard x-ray diffraction experiment with sub-picometer spatial and femtosecond temporal resolution [26]. This experiment has further shown that the vibrational excitation of infrared-active modes in manganites can be transformed into directional changes of the MnO_6 octahedra rotations and possibly also into

105

motions along the Jahn-Teller mode, structural degrees of freedom, which determine the equilibrium electronic and magnetic ground state of manganites. Nonlinear coupling to these distortions was proposed to cause the insulator-metal transition and the melting of magnetic order observed to follow resonant lattice excitation of $Pr_{0.7}Ca_{0.3}MnO_3$ and $La_{0.5}Sr_{1.5}MnO_4$ [9, 41, 11].

The demonstration of nonlinear lattice dynamics in LSMO motivated us to investigate their role in the resonant lattice excitation of the high temperature superconductor $YBa_2Cu_3O_{6+x}$ (YBCO), which had been shown to enhance the superfluid density below the transition temperature T_c and induce interlayer Josephson tunneling far above T_c, creating a transient state with all optical properties of the equilibrium superconducting state [7, 8]. By combining ultrafast time-resolved x-ray diffraction with density functional theory (DFT) calculations, we determined the transient crystal structure of YBCO. In a subsequent study, we measured the coherent lattice dynamics underlying this transition [33, 40].

We found a change in distance of the CuO_2 planes, consistent with the previously observed redistribution of interlayer coherence. DFT calculations of the electronic properties associated with the transient structure further predict a charge redistribution from these planes to the Cu-O chains. Such charge redistribution has recently been found to accompany the temperature driven metal-superconductor transition and might thus be beneficial for superconductivity [81]. In fact, in earlier studies the application of pressure had been shown to induce similar structural changes, which are also accompanied by charge transfer and increase the transition temperature of underdoped YBCO above the value of optimally doped samples [29, 30, 31]. Moreover, positive effects of the lattice rearrangement on superconductivity have been found in a theoretical study by an external group, which predicts an increase of T_c by up to 100% [34]. The results of these studies show that the lattice rearrangements we found might explain the observed emergence of transient superconductivity at room temperature.

We proposed further studies to experimentally verify the predicted charge redistribution following the resonant lattice excitation. The impact of the excitation on the pseudogap, which is likely to be connected to the super-

conducting phase, should also be investigated for a more complete picture of the transition.

Another important result of our experiment is the excellent agreement between the ab-initio DFT calculations of the nonlinear phonon coupling strengths and the time-resolved x-ray diffraction measurements. On these grounds, DFT can be used in the future to predict the nonlinear phonon coupling in other materials. The combination of this theory with the dynamical model of nonlinear phonon coupling presented in Chapter 1 constitutes a toolset for simulating the nonlinear lattice dynamics induced by resonant lattice excitation of specific infrared-active modes of a material. The work presented in this thesis thus paves the way for designing experiments which make use of advanced structural control schemes, as necessary for example for the reversible control of phase states using multiple light pulses.

Author contributions

Parts of the experiments presented in this thesis were done at the Linac Coherent Light Source (LCLS) x-ray Free Electron Laser and involved large collaborations. In the following, my contributions to the experiments presented in this thesis are summarized and the corresponding publications cited.

Chapter 1

The theoretical framework of Nonlinear Phononics as presented in this thesis is the result of discussions with all colleagues of my group and external collaborators. I especially want to thank Alaska Subedi, Michael Först, Antoine Georges, Roberto Merlin and Andrea Cavalleri for stimulating discussions.

Chapter 2

The first measurement of directional atomic displacements along a Raman phonon coordinate due to anharmonic coupling to a resonantly excited infrared-active phonon mode involved measurements at the LCLS in a large collaboration. For the preparation of the experiment, I did structure factor calculations with the help of S. Johnson and characterized, cut and polished the sample for the beamtime. I helped M. Först in leading the experiment and analyzed the data. I further characterized the domain structure of the sample after the beamtime. The samples were provided by Y. Tomioka and Y. Tokura. [26]

Chapter 3

Chapter 4 is an introduction to the following two chapters on the measurements of structural dynamics in YBCO and summarizes work performed by others.

Chapter 4

The determination of the transient lattice structure of YBCO following resonant lattice excitation involved measurements at the LCLS in a large collaboration. Ahead of this experiment, I performed structure factor calculations using the theoretical predictions for nonlinear phonon coupling by Michael Fechner and N. Spaldin and proposed the experiment at the LCLS. Further, I characterized the samples. I led the experiment and analyzed the data in close collaboration with A. Subedi, who provided the results of Density Functional Theory calculations, which were fundamental for the interpretation of the work. The samples were provided by T. Loew and B. Keimer. [33]

Chapter 5

The work presented in Chapter 6 has been done in the laser lab. I prepared the samples, took the measurements and analyzed the data. The samples were provided by T. Loew, J. Porras and B. Keimer. [40]

List of publications

Structural Control of Cuprates

[1] **Mankowsky, R.**, Subedi, A., Först, M., Mariager, S. O., Chollet, M., Lemke, H. T., Robinson, J. S., Glownia, J. M., Minitti, M. P., Frano, A., Fechner, M., Spaldin, N. A., Loew, T., Keimer, B., Georges, A., and Cavalleri, A. Nonlinear lattice dynamics as a basis for enhanced superconductivity in $YBa_2Cu_3O_{6.5}$. *Nature* **516**, 71 (2014).

[2] **Mankowsky, R.**, Först, M., Loew, T., Porras, J., Keimer, B., and Cavalleri, A. Coherent modulation of the $YBa_2Cu_3O_{6+x}$ atomic structure by displacive stimulated ionic Raman scattering. *Physical Review B* **91**, 094308 (2015).

[3] **Mankowsky, R.** Supraleitung bei Raumtemperatur. *Physik in unserer Zeit* **46**, 238 (2015).

[4] Först, M., Frano, A., Kaiser, S., **Mankowsky, R.**, Hunt, C. R., Turner, J. J., Dakovski, G. L., Minitti, M. P., Robinson, J., Loew, T., Le Tacon, M., Keimer, B., Hill, J. P., Cavalleri, A., and Dhesi, S. S. Femtosecond x rays link melting of charge-density wave correlations and light-enhanced coherent transport in $YBa_2Cu_3O_{6.6}$. *Physical Review B* **90**, 184514 (2014).

Structural control of Manganites

[5] Först, M., **Mankowsky, R.**, Bromberger, H., Fritz, D. M., Lemke, H., Zhu, D., Chollet, M., Tomioka, Y., Tokura, Y., Merlin, R., Hill, J. P., Johnson, S. L., and Cavalleri, A. Displacive lattice excitation through nonlinear phononics viewed by femtosecond X-ray diffraction. *Solid State Communications* **169**, 24 (2013).

[6] Först, M., **Mankowsky, R.**, and Cavalleri, A. Mode-Selective Control of the Crystal Lattice. *Accounts of Chemical Research* **48**, 380 (2015).

[7] Beyerlein, K. R., Jooss, C., Barty, A., Bean, R., Boutet, S., Dhesi, S. S., Doak, R. B., Först, M., Galli, L., Kirian, R. A., Kozak, J., Lang, M., **Mankowsky, R.**, Messerschmidt, M., Spence, J. C. H., Wang, D., Weierstall, U., White, T. A., Williams, G. J., Yefanov, O., Zatsepin, N. A., Cavalleri, A., and Chapman, H. N. Trace phase detection and strain characterization from serial X-ray free-electron laser crystallography of a $Pr_{0.5}Ca_{0.5}MnO_3$ powder. *Powder Diffraction* **30**(S1), S25 (2015).

Structural Control of Nickelates

[8] Först, M., Caviglia, A. D., Scherwitzl, R., **Mankowsky, R.**, Zubko, P., Khanna, V., Bromberger, H., Wilkins, S. B., Chuang, Y.-D., Lee, W. S., Schlotter, W. F., Turner, J. J., Dakovski, G. L., Minitti, M. P., Robinson, J., Clark, S. R., Jaksch, D., Triscone, J.-M., Hill, J. P., Dhesi, S. S., and Cavalleri, A. Spatially resolved ultrafast magnetic dynamics initiated at a complex oxide heterointerface. *Nature Materials* **14**, 883–888 (2015).

[9] Caviglia, A. D., Först, M., Scherwitzl, R., Khanna, V., Bromberger, H., **Mankowsky, R.**, Singla, R., Chuang, Y. D., Lee, W. S., Krupin, O., Schlotter, W. F., Turner, J. J., Dakovski, G. L., Minitti, M. P., Robinson, J., Scagnoli, V., Wilkins, S. B., Cavill, S. A., Gibert, M., Gariglio, S., Zubko, P., Triscone, J. M., Hill, J. P., Dhesi, S. S., and Cavalleri, A. Photoinduced melting of magnetic order in the correlated electron insulator $NdNiO_3$. *Physical Review B* **88**, 220401 (2013).

Appendix A

Various

A.1   Pump-probe spectroscopy

Pump-probe spectroscopy allows for measuring the evolution of physical properties during the transition into an excited state and the subsequent relaxation back to equilibrium. Typically, a laser pulse is split into two, of which one is used to drive the sample into an excited state and the second pulse is used to probe a certain property of the sample, such as its reflectivity. By varying the relative arrival time between pump and probe pulse at the sample position, the evolution of this property in time can be mapped out (see Figure A.1.1). The wavelengths of both pump and probe pulses can span several orders of magnitude from mid-infrared to excite and probe low energy excitations of the material up to hard x-rays to probe its structural properties. Lab-based laser systems usually operate either at MHz repetition rate with low pulse energies or at kHz repetition rate, if amplifier systems are used, which provide laser pulses of higher energy. In the experiments presented in this thesis, laser pulses were used to resonantly excite vibrational modes of materials. The energy scales of these excitation is in the range of 10-100 meV. The generation of pump pulses in this energy range requires down-conversion of higher energy photons, which inevitably involves losses (see section A.2). Therefore, amplifier systems were used as basis to generate the pump pulses, limiting the repetition rate of the experiments involving

113
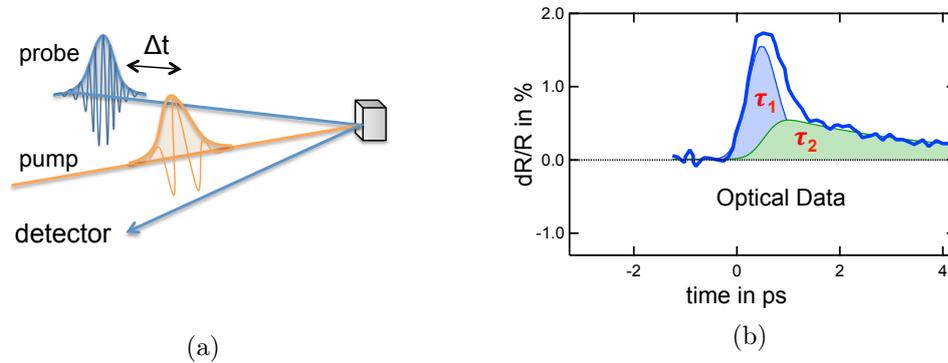
Figure A.1.1: a) In pump-probe experiments, light pulses from a laser are split in two pulses of which one is used to drive the sample in an excited state and the second pulse is used to measure a certain property of the sample, such as its reflectivity. b) Typical signal, showing the relative change in reflectivity due to the excitation with a rise time of ~ 300 fs and two decay times.

laser-based pump and probe pulses to 1kHz. The experiments based on x-ray probe pulses were done at 120Hz repetition rate, limited by the free electron laser, which is further described in Appendix C.

In order to increase the signal to noise ratio, the pump pulses are usually chopped and the signals from the probe pulses measured with a lock-in amplifier. By setting the lock-in to detect signals at the chopped frequency, only the changes induced by the pump pulse are measured. Typical integration times of the lock-in amplifiers are ~ 300 ms. Thus, the average signal from many individual pulses is detected and only directional changes can be measured. Signals with random signs for each excitation, such as the lattice displacements due to fourth order coupling, are averaged to zero. A deeper understanding of equilibrium interactions between different subsystems can be gained by probing their response to specific excitations. The interaction of different subsystems to the excitation, such as electronic properties, charge order, magnetism and structural changes, may be disentangled by their respective response and recovery times τ or by using probe pulses, which are selectively sensitive to certain properties of the material. Further information lies in their recovery time. Panel b) of Figure A.1.1 shows a typical signal

with a rise time of ~ 300 fs and two decay times. If coherent excitations are generated by the pump pulse, they may be observed as oscillations at characteristic frequencies, which depend on their energy scales.

A.2   Generation of high field mid-infrared pulses

Optical parametric amplification

The mid-infrared pulses used for resonant excitation of infrared-active phonon modes are generated by optical parametric amplification and difference frequency generation from femtosecond 800 nm pulses. Optical parametric generation (OPG) describes the conversion of one photon of the pump pulse (here at 800 nm) into one signal and one idler photon in a nonlinear active medium with $\omega_i < \omega_s < \omega_p$, where ω_i, ω_s and ω_p denote the angular frequencies of pump, signal and idler photons, respectively. Energy and momentum conservation require $\omega_i + \omega_s = \omega_p$ and $\mathbf{k}_i + \mathbf{k}_s = \mathbf{k}_p$. The energies of signal and idler pulses can range from $\omega_p/2$ in the degenerate case to ω_p and 0, respectively. Optical parametric amplification (OPA) describes the same process with a second light pulse at the signal wavelength stimulating the process and fixing ω_i and ω_p. OPG is a second order $(\chi^{(2)})$ nonlinear process, in which the generated signal intensity I_s depends on the effective nonlinear coefficient d_{eff} of the generation crystal, the intensity of the pump pulse I_p and the signal and idler wavelengths λ_s, λ_i as $I_s \sim I_{s0} \exp\left(\Gamma L\right)$, with $\Gamma \sim I_p d_{eff}/\sqrt{n_i n_s n_p \lambda_i \lambda_s}$. The generated signal intensity thus grows exponentially with the crystal thickness L, assuming no walk-off of the beams due to group velocity mismatch. More details can be found in Ref. [87].

Phase matching

Phase matching, which is the requirement to prevent walk-off between pump and signal / idler pulses, can be expressed as $\mathbf{k}_i + \mathbf{k}_s = \mathbf{k}_p$ or

$$n_p = \frac{n_i \omega_i + n_s \omega_s}{\omega_p}.$$

This condition can only be achieved in birefringent materials with different dispersion relations $n(\omega)$ along distinct optical axis. The commonly used crystals for OPAs are negative uniaxial crystals with one extraordinary optical axis along which the refractive index is smaller ($n_e < n_o$). The pump pulses are polarized along the extraordinary axis. Phase matching is distinguished into type I, in which both signal and idler are polarized along the ordinary axis and type II, in which either signal or idler have the same polarization as the pump pulse. Type I and type II phase matching can be achieved by rotating the crystal around the extraordinary axis, which modifies the refractive index of the pump pulse and, for type II phase matching, the signal or idler pulse with the same polarization.

Generation Setup

The setup used to generate the mid-infrared pulses is shown in Figure A.2.2. Two signal pulses generated from the same white light in two symmetrical arms are used for the mid-infrared generation by difference frequency generation. The OPAs are pumped with 35 fs pulses with 1.5 mJ pulse energy and 800 nm wavelength at 1kHz, which are split by a 50/50 beam splitter for the two paths. The white light continuum, which is used as seed for the first OPA stages, is generated by a small fraction of the pump light, focussed in sapphire. The pump pulses are s-polarized and type-II phase matching in Beta Barium Borate (β-BBO) is used to select the signal wavelengths of 1238 nm and 1350 nm for amplification from the continuum. Pumped with 110 µJ pulses focused to peak intensities of 55 GW/cm^2, signals with energies of around 4 µJ are generated, which are then used to seed the next amplification stages. Here, 630 µJ pump pulses with peak intensities of 55 GW/cm^2 are used to amplify the signals to 160 µJ at 1350 nm and 200 µJ at 1238 nm. The pulses are focused onto the gallium selenide (GaSe) crystal almost collinear with an angle of only a few degrees to generate the mid-infrared pulses, yielding 3-4 µJ pulse energy at 15 µm. The overall efficiency of the conversion is thus approximately 0.2%.
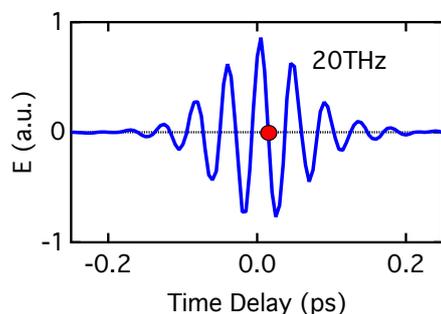
Figure A.2.1: The active stabilization of the mid-infrared pulse CEP is done in the time domain by electrooptic sampling. By setting the delay between 800 nm probe and mid-infrared pulses to the zero crossing of the field (red circle), changes of the CEP can be detected as positive or negative signals.

Carrier envelope phase stabilization

The carrier envelope phase (CEP) of the 800nm pulses from the amplifier varies from shot to shot. The CEP of the white light φ_0 generated from these pulses is thus also not stable. As the phase of the seed determines the phase of the signal generated in the OPA and the same white light pulses are used in the two arms, the signals generated in the first stages have the same phase variations. Following the same argument, also the amplified signals have the same carrier envelope phase variations. The phase of the mid-infrared pulses generated in the DFG process is given by the difference between the phases of the two signals it is generated from and thus stable.

Although the generated pulses are intrinsically phase stable, there are long term drifts in the phase due to temperature fluctuations. To compensate for these drifts, an active stabilization scheme was employed, which is shown in Figure A.2.3. For the stabilization, $\sim$10% of the mid-infrared light is reflected by a pellicle. The CEP of these split pulses is measured by electrooptic sampling in a 100 μm GaSe crystal. By setting the delay between 800 nm probe and mid-infrared pulses to the zero crossing of the field between maximum and minimum values (red circle in Figure A.2.1), the CEP can be stabilized by actively compensating positive and negative deviations with two glass wedges, of which one is moved in or out of the path of one of the NIR beams.

117
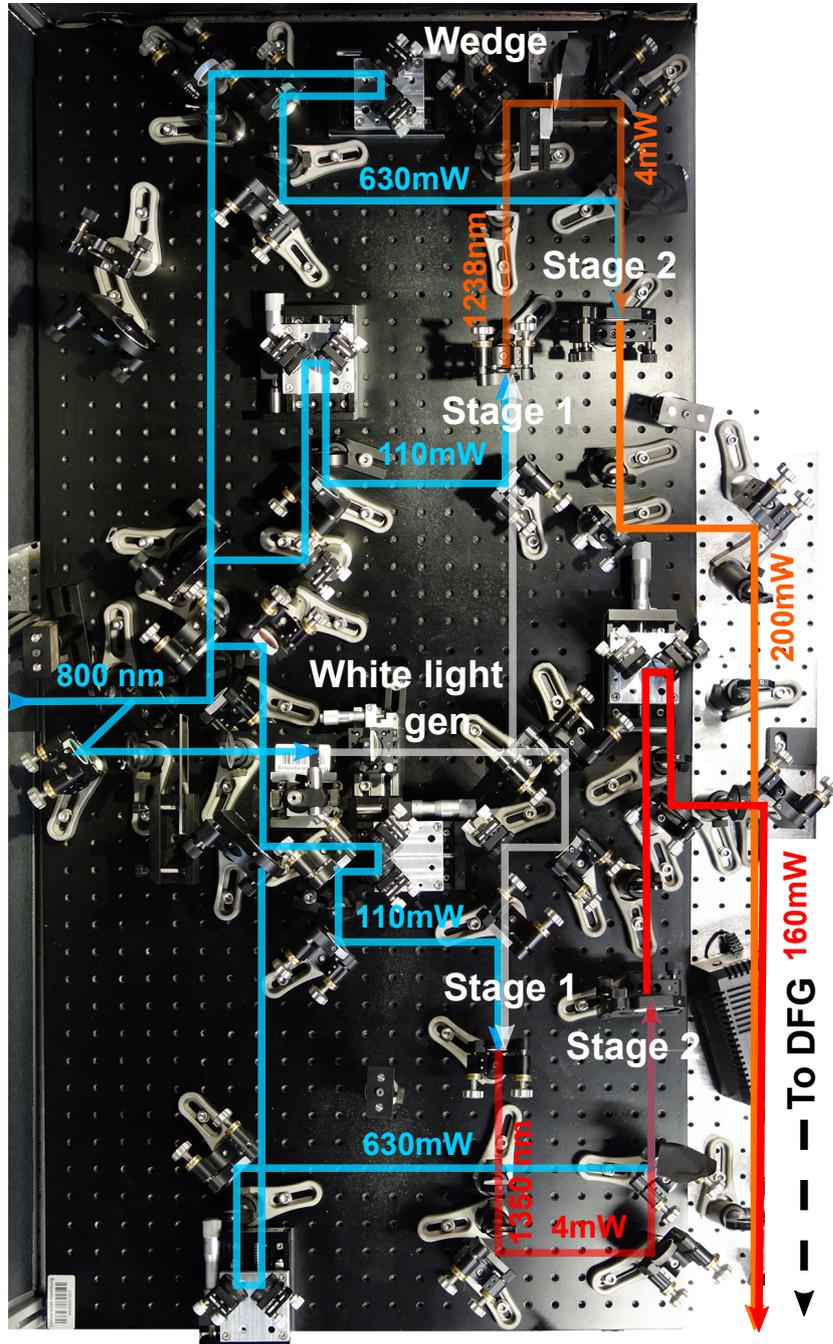
Figure A.2.2: Setup for the generation of tunable near infrared pulses by optical parametric amplification. The OPA stages are followed by a difference frequency generation stage to generate mid-infrared pulses show, which is shown in Figure A.2.3.
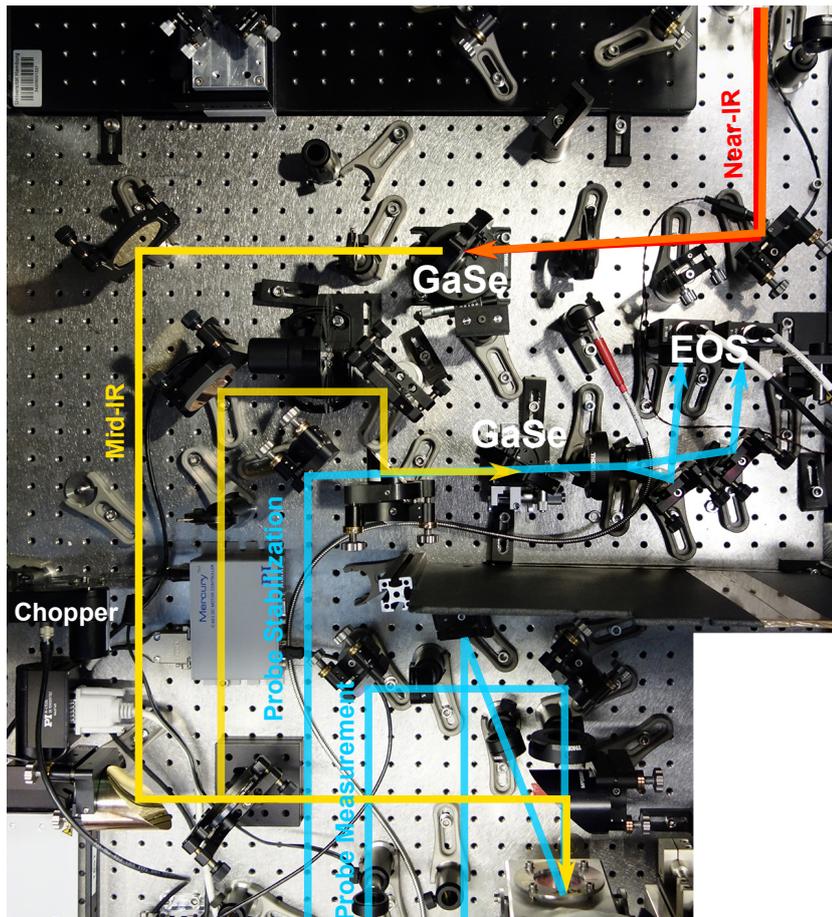
Figure A.2.3: Setup for difference frequency generation of mid-infrared pulses. Further shown is the active stabilization of the mid-infrared carrier envelope phase and the experimental setup for the measurement of 800nm probe pulses in reflection geometry.

A.3 Equivalent Circuit
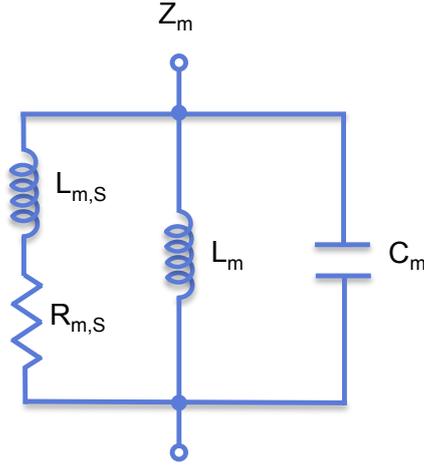
Figure A.3.1: The optical properties of a Josephson junction at $\mathbf{k} = 0$ can be described by an equivalent LC circuit. Quasi-particle currents are introduced by shunting the circuit with a resistance $R_{m,S}$ in series with an inductance $L_{m,S}$ [71].

In the following derivation, the common convention for optics, in which the electric field is defined as $E \sim \exp\left(-i\omega t\right)$, is used. The complex permittivity and index of refraction are defined as $\varepsilon = \varepsilon_1 + i\varepsilon_2$, $N = n + ik$ and the impedances of ohmic resistance, capacitance and induction can be written as R, $-\left(i\omega C\right)^{-1}$ and $-i\omega L$, respectively. The complex impedance for the junction m of Figure A.3.1 is then:

$$\frac{1}{Z_m} = \frac{1}{R_{m,S} - i\omega L_{m,S}} - \frac{1}{i\omega L_m} - i\omega C_m,$$

with $R_{m,S}$ and $L_{m,S}$ being the resistance and induction of the shunt and C_m and L_m the capacitance and induction of the Josephson junction. Using $\tau_m = \frac{L_{m,S}}{R_{m,S}}$ and assuming a capacitance of $C_m = \frac{\varepsilon_r A}{4\pi d_m}$ in Gaussian units, with A being the area of the junction and d_m the distance between the two superconducting layers, the formula can be written as:

$$\frac{1}{Z_m} = \frac{\omega}{4\pi i}\frac{A}{d_m}\left(\frac{4\pi i}{\omega}\frac{d_m}{AR_{m,S}}\cdot\frac{1}{1-i\omega\tau_m}+\varepsilon_r\left(1-\frac{1}{\omega^2 C_m L_m}\right)\right),$$

which can be further simplified to

$$\frac{1}{Z_m} = \frac{\omega}{4\pi i}\frac{A}{d_m}\left(\frac{4\pi i}{\omega}\sigma_{m,S}+\varepsilon_r\left(1-\frac{\omega_m^2}{\omega^2}\right)\right).$$

Here, we introduced the resonance frequency of the circuit $\omega_m = 1/\sqrt{C_m L_m}$ and defined the total conductance of the shunt as

$$\sigma_{m,S} = \frac{d_m}{AR_m}\frac{1}{1-i\omega\tau_{m,S}} = \frac{\sigma_{m,0}}{1-i\omega\tau_{m,S}}.$$

The total impedance is composed of the impedance of the single junctions in series: $Z = \sum_m Z_m$. The optical conductivity and permittivity directly follow from $\sigma = D\left(AZ\right)^{-1}$ and $\varepsilon = 4\pi i\sigma\omega^{-1}$. They can be expressed by a sum over the permittivity of the microscopic junctions, weighted by a factor $w_m = d_m/D$, proportional to the distance between the superconducting layers of the junction.

$$\sigma = \left(\sum_m \frac{w_m}{\sigma_m}\right)^{-1}, \text{ with } \sigma_m = \left(\sigma_{m,S}+\frac{\omega}{4\pi i}\varepsilon_r\left(1-\frac{\omega_m^2}{\omega^2}\right)\right), \qquad (A.3.1)$$

$$\varepsilon = \left(\sum_m \frac{w_m}{\varepsilon_m}\right)^{-1}, \text{ with } \varepsilon_m = \left(\frac{4\pi i}{\omega}\sigma_{m,S}+\varepsilon_r\left(1-\frac{\omega_m^2}{\omega^2}\right)\right). \qquad (A.3.2)$$

A.4   Phonon squeezing

To simplify the formulas in the derivation of the equation of motion of the variance $\sigma_{\mathbf{q},\mathrm{j}}^2 = \left\langle Q_{\mathbf{q},\mathrm{j}}^2 \right\rangle$, we omit the indices of the coupled mode and write $P = P_{\mathbf{q},\mathrm{j}}$ and $Q = Q_{\mathbf{q},\mathrm{j}}$. From the lattice Hamiltonian

$$H = \frac{1}{2}\left(P_{\mathrm{ir}}^2 + \omega_{\mathrm{ir}}^2 Q_{\mathrm{ir}}^2\right) + \frac{1}{2}\left(P^2 + \omega^2 Q^2\right) - a_{22} Q_{\mathrm{ir}}^2 Q^2,$$

the time derivatives of momentum and position coordinates follow as $\dot{Q} = P$ and $\dot{P} = -Q\left(\omega^2 - a_{22}Q_{\mathrm{ir}}^2\right)$. The time derivatives of P^2 and Q^2 can be written as

$$\frac{d}{dt}Q^2 = 2QP, \tag{A.4.1}$$

$$\frac{d}{dt}P^2 = -2QP\left(\omega^2 - a_{22}Q_{\mathrm{ir}}^2\right) \overset{(A.4.1)}{=} -\left(\omega^2 - a_{22}Q_{\mathrm{ir}}^2\right)\frac{d}{dt}Q^2. \tag{A.4.2}$$

The second and third derivatives in time of the variance then read

$$\frac{d^2}{dt^2}Q^2 = 2\dot{Q}P + 2Q\dot{P} = 2P^2 - 2Q^2\left(\omega^2 - a_{22}Q_{\mathrm{ir}}^2\right),$$

$$\frac{d^3}{dt^3}Q^2 = 2\frac{d}{dt}P^2 - 2\left(\omega^2 - a_{22}Q_{\mathrm{ir}}^2\right)\frac{d}{dt}Q^2 + 2Q^2\left(a_{22}\frac{d}{dt}Q_{\mathrm{ir}}^2\right)$$

$$\overset{(A.4.2)}{=} -2\left(\omega^2 - a_{22}Q_{\mathrm{ir}}^2\right)\frac{d}{dt}Q^2 - 2\frac{d}{dt}Q^2\left(\omega^2 - a_{22}Q_{\mathrm{ir}}^2\right) + 2Q^2\left(a_{22}\frac{d}{dt}Q_{\mathrm{ir}}^2\right).$$

Sorting the terms yields the equation of motion:

$$\frac{d^3\left\langle Q_{\mathbf{q},\mathrm{j}}^2\right\rangle}{dt^3} + 4\left[\omega_{\mathbf{q},\mathrm{j}}^2 - a_{22}Q_{\mathrm{ir}}^2(t)\right]\frac{d\left\langle Q_{\mathbf{q},\mathrm{j}}^2\right\rangle}{dt} = 2\left\langle Q_{\mathbf{q},\mathrm{j}}^2\right\rangle\left(a_{22}\frac{d}{dt}Q_{\mathrm{ir}}^2\right).$$

Appendix B

Basics of optical probe experiments

B.1 Interaction of light with phonon fields

When the electric field of a light pulse enters a material, it induces a polarization. For small field strengths, the polarization depends linearly on the electric field according to $P(t) = \varepsilon_0 \chi^{(1)} E(t)$. The frequency-dependent proportionality constant $\chi^{(1)}$ is known as the linear or the first order susceptibility. For higher field strengths, nonlinear optical effects become significant. The response of the material can often be described by expressing the susceptibility as a power series in the electric field strength [88]:

$$ P(t) = \varepsilon_0 \left(\chi^{(1)} E(t) + \chi^{(2)} E^2(t) + \chi^{(3)} E^3(t) + ... \right). $$

The quantities $\chi^{(2)}$ and $\chi^{(3)}$ are the second and third order susceptibilities. The quadratic and cubic terms in the electric field describe polarizations that vary at different frequencies and act as source terms for emitted radiation at these frequencies. Lattice dynamics such as coherent phonons and other excitations can modulate this polarization. The interaction can thus be described by expanding the susceptibility χ in the coordinates of the electric field E and the phonon normal coordinates Q_i, with the index $i = (n, \mathbf{q})$ holding both the mode n as well as wave vector $\mathbf{q}$ as

$$P(t) = \varepsilon_0 \left(\chi E(t) + \frac{\partial \chi}{\partial E} E^2(t) + \frac{\partial^2 \chi}{\partial E^2} E^3(t) + \ldots + \sum_i \frac{\partial \chi}{\partial Q_i} Q_i(t) E(t) + \right.$$
$$\left. + \sum_{i,j} \frac{\partial^2 \chi}{\partial Q_i \partial Q_j} Q_i(t) Q_j(t) E(t) + \sum_i \frac{\partial^2 \chi}{\partial E \partial Q_i} Q_i(t) E^2(t) + \ldots \right),$$

$$(\text{B.1.1})$$

where the coefficients $\partial^n \chi / \partial E^n$ correspond to the nonlinear susceptibilities $\chi^{(n)}$. The interaction terms can be sorted by their order in the electric field. The first term

$$\frac{\partial \chi}{\partial Q_i} Q_i(t) E(t)$$

describes a direct modulation of the reflectivity of a material due to the motion of the atoms along the coordinate $Q_{(i=n,\mathbf{q})}$. The lattice dynamics induced by nonlinear phononics involve to lowest order the coherent excitation of optical Raman phonons (with $\mathbf{q} \approx 0$) as well as a displacive response along the same coordinate. Both these effects can be observed as a modulation of the reflectivity, described by this term. While the oscillatory component can easily be distinguished from any other pump induced effect by its frequency, the displacive response has a similar signature as electronic excitations, consisting of a rise followed by an exponential decay. It can thus only be measured in special cases by optical methods. The second term

$$\frac{\partial^2 \chi}{\partial Q_i \partial Q_j} Q_i(t) Q_j(t) E(t)$$

describes either a squeezed phonon or the modulation of the reflectivity by a combined motion of two different phonon modes at their sum or difference frequency. In the case of squeezing, the modes can be generated through quartic coupling at any pair of wave vectors that sum up to zero. Thus, in most cases no sharp frequency component appears but a broad continuum with maxima coinciding with frequencies at which the phonon density of states is large. The last term

124

$$\frac{\partial^2 \chi}{\partial E \partial Q_i} Q_i(t) E^2(t)$$

describes the modulation of the second harmonic at twice the fundamental frequency by the phonon mode, similar to the first term. The main difference is the symmetry of the phonon modes that can be observed in the fundamental and second harmonic. In centrosymmetric materials the expansion can be simplified by a symmetry analysis. As the Polarization P is odd under spatial inversion, the same must be true for all individual terms on the right side of equation B.1.1. To further simplify the problem, we omit the sum over all phonon coordinates and just consider coupling to one infrared and one Raman phonon. As the electric field E and the infrared phonon coordinate Q_{ir} are odd while Raman modes Q_{R} are even, all terms on the right side must be of odd order in E, Q_{IR} or mixed terms. Thus, for centrosymmetric materials, the polarization limited to third order terms reduces to:

$$P(t) = \varepsilon_0 \left(\chi E(t) + \frac{\partial^2 \chi}{\partial E^2} E^3(t) + \sum_{\mathrm{R}} \frac{\partial \chi}{\partial Q_{\mathrm{R}}} Q_{\mathrm{R}}(t) E(t) + \sum_{\mathrm{R}} \frac{\partial^2 \chi}{\partial Q_{\mathrm{R}}^2} Q_{\mathrm{R}}^2(t) E(t) \right.$$
$$\left. + \sum_{\mathrm{ir}} \frac{\partial^2 \chi}{\partial Q_{\mathrm{ir}}^2} Q_{\mathrm{ir}}^2(t) E(t) + \sum_{\mathrm{ir}} \frac{\partial^2 \chi}{\partial E \partial Q_{\mathrm{ir}}} Q_{\mathrm{ir}}(t) E^2(t) \right) . \qquad (\mathrm{B.1.2})$$

The reflectivity is thus directly modified by coherent Raman modes, while IR modes can be observed in the second harmonic of the incident light. Here, $\frac{\partial^2 \chi}{\partial E \partial Q_{\mathrm{ir}}}$ denotes the hypersusceptibility tensor of the mode Q_{ir}. Note that this is the phononic equivalent to electric field induced second harmonic generation (EFISH). Further, the product of any two infrared, Raman or even acoustic modes can modulate the reflectivity at their sum or difference frequency.

B.2 Optical probe of lattice dynamics

As discussed above, in centrosymmetric materials coherent Raman modes can be observed as oscillations in the reflectivity, described by the term

$$\frac{\partial \chi}{\partial Q_i} Q_i(t) E(t),$$

where $\partial \chi / \partial Q_i$ is the Raman tensor of the phonon mode Q_i. In order to quantify the atomic motions from the amplitude of the oscillatory component in the light induced reflectivity changes, the elements of the Raman tensor have to be known.

B.2.1 Experimental Setup

For a sketch of the experimental setup, see Figure B.2.1. The mid-infrared pulses are focused with a 90° off-axis parabola with an effective focal length of 100 mm to a minimal spot size of 140 μm. The 800 nm probe beam is focused through a hole in the parabola onto the sample. The measurements were done in a cryostat from the company Janis with a polypropylene window, which is transparent to the mid-infrared pump and the 800nm probe pulses. In the experiment on YBCO, the 800 nm pulses were polarized at 45° between the crystallographic c- and a-axis. Changes in the reflectivity of s- and p-polarized pulses were detected simultaneously with two diodes by splitting the reflected 800 nm pulses with a Wollaston prism. Before this scheme was applied, it was made sure that no polarization rotation occurs by checking for s-polarized reflected light with incident p-polarized pulses and p-polarized reflected light with incident s-polarized pulses. In order to increase the sensitivity, the mid-infrared pump pulses were chopped and the signals from the diodes measured with lock-in amplifiers.

Sample

To detection

800 nm-Probe

Mid-IR
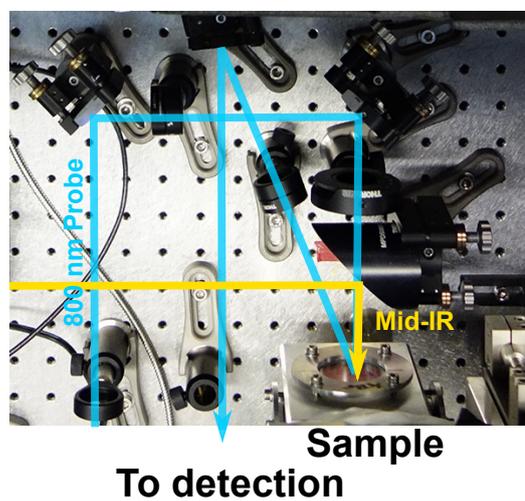
Figure B.2.1: Experimental setup for the optical pump-probe measurements in reflection geometry.

Appendix C

Basics of x-ray probe experiments

C.1   X-ray probe of lattice dynamics

The experiments presented in Chapters 2 and 3 make use of femtosecond x-ray pulses from the Linac Coherent Light Source free electron laser and were done at the X-ray Pump Probe (XPP) beamline.

C.1.1   X-ray diffraction

The hard x-ray wavelength range is usually defined as < 2 Angstrom (> 6 keV), which coincides with interatomic distances in solids. X-rays with these wavelengths are scattered by the periodically arranged atoms of the crystal lattice and interfere. The analysis of the resulting interference patterns gives detailed information on the crystal structure with sub-pm spatial resolution and has become a common tool in solid state physics. The scattering intensity of x-ray light is highly sensitive to the crystal structure and its basis, that is, the positions and types of atoms in the unit cell. The dependence of the diffracted intensity on the atomic positions in the basis is given by $I_{hkl} \sim |F_{hkl}|^2$, where F_{hkl} is the structure factor

$$F_{hkl} = \sum_j f_j \exp\left(-i\boldsymbol{G}_{hkl} \cdot \boldsymbol{r}_j\right).$$

Here, $\boldsymbol{G}_{hkl}$ is the reciprocal lattice vector with Miller indices (h, k, l). The sum runs over all atoms in the unit cell with $\boldsymbol{r}_j$ and f_j denoting their position and scattering factor. Lattice dynamics along optical phonon coordinates involve a motion of atoms in the unit cell away from their equilibrium positions $\boldsymbol{r}_j^{(0)}$ according to

$$\boldsymbol{r}_j' = \boldsymbol{r}_j^{(0)} + \sum_i Q_i\left(t\right) \boldsymbol{\epsilon}_{ij},$$

where $Q_i\left(t\right)$ is the normal coordinate of the phonon mode i, which for finite cubic coupling to an infrared mode describes a displacement and oscillations for modes with periods long compared to the the mid-infrared pulse duration as discussed in section 1.1. The relative motions of each atom of the unit cell are given by the eigenvector $\boldsymbol{\epsilon}_{ij}$ of the respective phonon mode. For given atomic displacements, the measured intensity of the Bragg reflection with indices (h, k, l) changes according to

$$\frac{\triangle I_{hkl}}{I_{hkl}} = \frac{\left|F_{hkl}(\boldsymbol{r}')\right|^2 - \left|F_{hkl}(\boldsymbol{r}^{(0)})\right|^2}{\left|F_{hkl}(\boldsymbol{r}^{(0)})\right|^2}.$$

The change in the structure factor for anticipated atomic motions can be evaluated and compared to the measurement to quantify the lattice displacements induced by the excitation of the infrared mode. In order to measure small changes and fast dynamics with sub picosecond time resolution, diffraction from femtosecond x-ray pulses is employed.

C.1.2   X-ray Free Electron Lasers

Characteristic timescales of lattice dynamics

As described in section 1.1, the timescale of lattice dynamics induced by anharmonic coupling to a resonantly excited infrared-active mode is limited by the impulsive force driving the Raman mode, which is given by the pump pulse duration of 250 fs in the experiments presented in this thesis. The response time of the indirectly coupled phonon modes can be estimated as $\frac{1}{4}$th of their period. Raman mode periods in Perovskites range from 50 fs for the fastest modes involving oxygen motions up to 1 ps. Dynamics on

these timescales (200 fs to 1 ps) following resonant lattice excitation have also been observed in other properties including insulator-metal transitions [9, 10], the enhancement of superconductivity [7, 8, 6] as well as melting of magnetic and charge order [80, 28]. In order to resolve and quantify the fast lattice dynamics underlying these light-induced phase transitions, femtosecond x-ray pulses have to be used. The relaxation time back to equilibrium can vary between a few picoseconds to very long timescales on the order of nanoseconds or longer, if the system is driven into a metastable state. Another critical requirement for mid-infrared pump, x-ray probe experiments is the pump fluence necessary to drive these transitions. As the mid-infrared pulses are generated through a cascade of nonlinear processes with an efficiency of around 0.2%, input pulses with high peak power are needed. At the same time, the average power is limited by the heat load on the crystals, thus limiting the repetition rate to a few kHz.

Short pulse x-ray sources

This requirement directly shows that these experiments are not well compatible with synchrotron sources, which in normal operation supply pulses on the order of tens of ps time duration with $\sim$500 MHz repetition rate. By limiting the repetition rate to a few kHz, pump-probe experiments investigating the recovery or slow dynamics can be done. The time resolution at synchrotrons can be increased to $\sim$1 ps by running the synchrotron with lower ring current, allowing for a better pulse compression (low-alpha mode), or to 140 fs by time-slicing the electron bunches with a femtosecond laser pulse. In this technique, the 100 ps electron bunches of the synchrotron are intersected with 55 fs optical laser pulses, which changes the energy of part of the electrons in the bunch (the numbers are given for the FEMTO beamline at the Swiss Light Source) [89]. In a second step, only radiation from the electrons with the modified energy is generated, yielding femtosecond x-ray pulses but reducing the number of photons per pulse by three orders of magnitude. Thus, both techniques lead to a significant loss in intensity. As an example, the FEMTO beamline at the Swiss Light Source provides

131

an x-ray flux of 10^5photons/s/0.1%bandwidth, which has to be compared to 10^{13}/s/0.1%bandwidth of the LCLS Free Electron Laser.

Free Electron Laser

The key advantage of using x-ray Free Electron Lasers (FEL) over synchrotrons to probe these lattice dynamics is thus the combination of femtosecond time resolution and high flux. Resolving small changes in weak diffraction peaks such as the (201) family of peaks, the Bragg reflections most sensitive to the induced lattice dynamics in LSMO of chapter 2, is only possible at free electron lasers. The functional principle of FELs can be compared to optical lasers, in which coherent radiation is generated by the stimulated emission of photons from an excited gain medium in a cavity. The gain medium in FELs are the electrons in a bunch, which start to radiate as they pass a cascade of undulators. The first photons, which are emitted spontaneously, interact with the electrons in the bunch, inducing a density variation. This micro-bunching is the basis for the generation of transverse coherent radiation. This process is called self-amplified spontaneous emission (SASE). Importantly, the electric field is added, when radiation is emitted coherently, while intensities are added for incoherently generated light as in undulators of synchrotrons. The intensity of the emitted x-ray pulses thus scales with the square of the number of electrons in the pulse instead of being linear to it. As SASE is a stochastic process, the pulse properties of emitted x-rays shows large variations from shot to shot. Figure C.1.1 shows the spectrum of two shots measured at the Soft X-ray Materials Science (SXR) beamline at 1.17 keV energy. Monochromators can be used to define the energy at the cost of higher intensity fluctuations.

The design of FELs is fundamentally different from synchrotrons. The basic design of LCLS-I and LCLS-II is sketched in Figure C.1.2. While electrons are kept on a circular trajectory in a synchrotron with undulators along the path, in which the x-ray radiation is generated in a tangential direction for each beamline, FELs are linear accelerators. The injector consists of a cathode in a high radio-frequency (RF) field. Upon illumination with a short
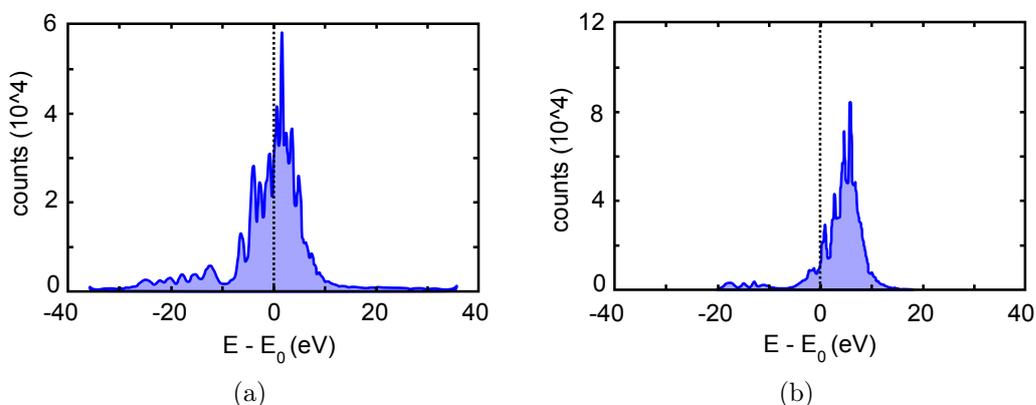
Figure C.1.1: Energy spectra of two x-ray pulses recorded at the SXR beamline at LCLS at a center wavelength of $E_0 = 1.17$ keV. Due to the random nature of the SASE process (see text), there are large energy fluctuations of consecutive pulses. (The data is taken from https://portal.slac.stanford.edu/sites/lcls_public/Lists/machine_faq/FAQ.aspx)

laser pulse, electrons are emitted and immediately accelerated by the RF field. This bunch is then further accelerated by RF cavities and compressed by magnetic chicanes, consisting of four magnetic dipoles. The radiation is generated in an array of undulators as discussed above. Thus, electrons have to be injected for each shot and only one beamline can operate at a time if the x-ray pulse is not shared. Due to this process, incorporating feedback loops to ensure a stable operation is more complicated than on synchrotron rings. The jitter between the x-ray pulses and the pump laser at LCLS was around 200-300 fs. For better time resolutions, additional time arrival monitors, which provide a shot-by-shot measurement of the time delay between pump and probe pulses, have to be used.

Further characteristics of x-ray FELs are the large wavelength range over which the pulses can be tuned, the high level of spatial coherence and the high peak intensity. They allow for resonant x-ray diffraction, x-ray absorption or imaging experiments as well as nano-crystallography or even single particle crystallography for biomolecules. The repetition rate at LCLS is mainly limited by the heat load generated in the non-superconducting acceleration cavities. The newly designed superconducting RF-cavities as implemented in the european XFEL support much higher repetition rates of up to 30000
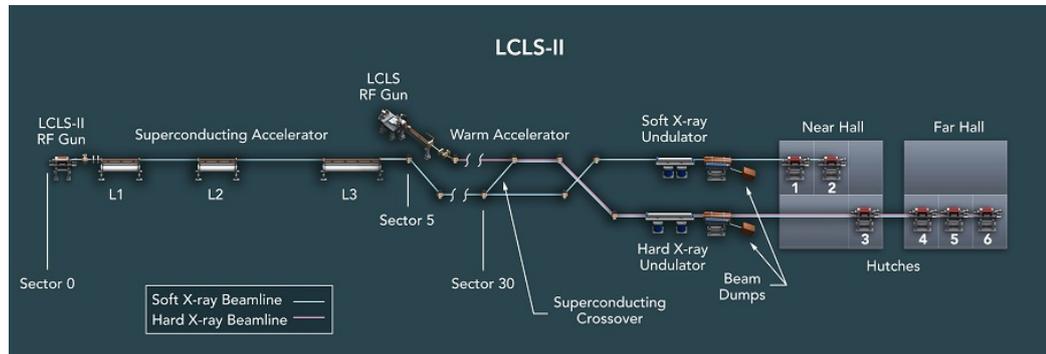
Figure C.1.2: FELs are linear accelerators, consisting of the injector, a cathode in a strong field RF cavity, from which electrons are emitted upon illumination with a short laser pulse, an accelerator section (L1-L3) with bunch compression and a cascade of undulators, in which the coherent radiation is generated. The image shows the layout of LCLS-I, which has Cu accelerators, labeled (Warm Accelerator) and LCLS-II, which will feature superconducting cavities for acceleration that can be operated in CW mode. The pictures are taken from the LCLS-II website with permission from LCLS.

pulses per second. The first operation will however feature trains of bunches evenly spaced in time with a repetition rate of 10 Hz that each consist of 3000 pulses, separated by 200 ns. This bunch structure is not generally suitable for time resolved studies of solid materials due to heating effects at such high repetition rates (200 ns pulse separation corresponds to 5 MHz). Future upgrades could however allow continuous wave (CW) operation of the cavities with evenly spaced pulses at high repetition rate. LCLS-II is aiming for a 100 kHz (or 1 MHz with the same average brilliance) system with evenly spaced pulses and pulse picking for multiple beamline operation, allowing for a range of new experiments that were not feasible due to small signals and new techniques such as time resolved resonant inelastic x-ray scattering (RIXS), which has already been tested successfully at LCLS-I with 120 Hz repetition rate and might be implemented as dedicated end station at LCLS-II [1].

---

[1]https://portal.slac.stanford.edu/sites/conf_public/LCLS2ScienceFeb15/
/sd/LCLS_II_Introduction_short_Dec_2014.pdf

C.1.3 Experimental setup
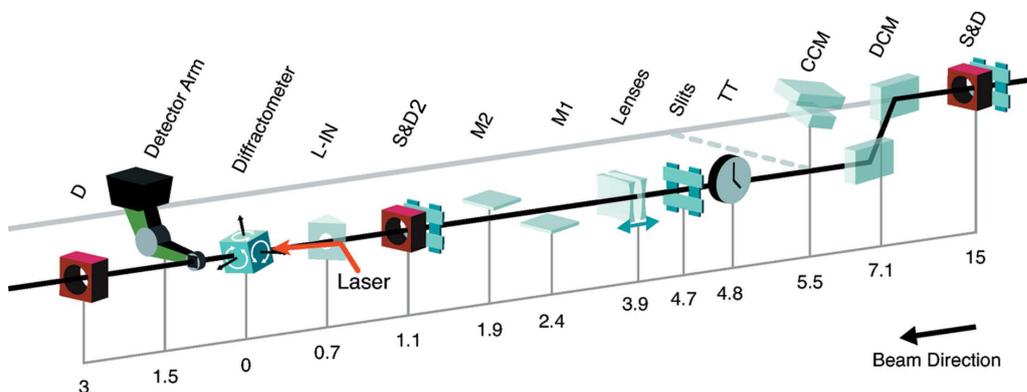
Figure C.1.3: Sketch of the x-ray pump probe beamline at LCLS. The entry slits and diagnostics (S&D) are used for the beamline alignment. CCM denotes a channel-cut Si (111) monochromator, (DCM) a monochromator with a better energy resolution, which cannot be scanned. The time tool (TT) monitors the arrival time of the x-ray pulses with respect to the optical pump pulses to achieve time resolutions of < 10 fs. The next pair of slits and lenses are used to define the spot size of the x-ray on the sample, M1 and M2 are a pair of Si vertical steering mirrors. The next slits and diagnostics (S&D2) feature a four quadrant intensity monitor for the x-ray pulses. The in-coupling of the pump pulses L-IN and the diffractometer depend on the experimental setup. The detector is mounted to a robot arm, which can freely be moved around the sample to pick up certain Bragg diffractions. The image was taken from [50].

Beamline design

The x-ray diffraction experiments were performed at the XPP beamline at the LCLS free electron laser. A sketch of the beamline is shown in Figure C.1.3 [50]. The entry slits and diagnostics S&D are used to align the x-ray beam through the beamline. We used a Si (111) channel-cut monochromator (CCM) with a resolution of $\Delta E/E = 1.4 \times 10^{-4}$ and x-ray energies of 6.0 keV for the experiments on LSMO and 6.7 keV for the experiments on YBCO. DCM denotes a second monochromator with a better energy resolution, which was not used in the experiments. In order to increase the time

resolution, the beamline features a timetool (TT), which measures the arrival time of the x-ray pulses with respect to the pump pulses from the optical laser system. The measurement of the arrival time relies on probing changes in the refractive index of a thin target, typically Si_3N_4or Ce:YAG induced by the x-ray pulses with chirped white light pulses generated from the optical laser and measured for each shot with a spectrometer. The delay between x-ray and optical pulses is then determined by fitting the frequency-resolved transmission change to resolutions below 10 fs. When the experiments presented in Chapters 2 and 4 were done, the timetool could not be operated with mid-infrared pump pulses, which limited the time resolution to around 250 fs. For the generation of the mid-infrared pulses, the 800nm pulses used to pump the optical parametric amplifier had to be stretched upstream. As no compatible compressor was available, the white light necessary for the operation of the timetool could not be generated.

The slits and lenses are used to define the size of the x-ray beam on the sample by either focusing with the lenses or using the slits to clip the beam. The second slits and diagnostics (S&D2) feature a 4 quadrant intensity monitor, which records the intensity of each x-ray pulse. This data can be used to normalize the measured diffracted intensity and filter the shots by pointing and x-ray pulse intensities. The in-coupling of the pump pulses L-IN and the diffractometer vary depending on the experiment. The detector is mounted to a robot arm, which can freely be moved around the sample to pick up certain Bragg diffractions.

Diffraction setup

Figure C.1.4 shows a picture of the experiment. The sample was mounted vertically to a huber goniometer with x-y-z stages, which was fixed to a rotational stage allowing for φ-rotation around the sample surface normal. A commercial nitrogen blower from Oxford Cryosystems was used to cool the sample to 100 K. The diffracted intensity was picked up by a diode, mounted to a robot arm, which can be freely moved above the experiment to pick up specific reflections. The x-ray diffraction experiments were performed in a
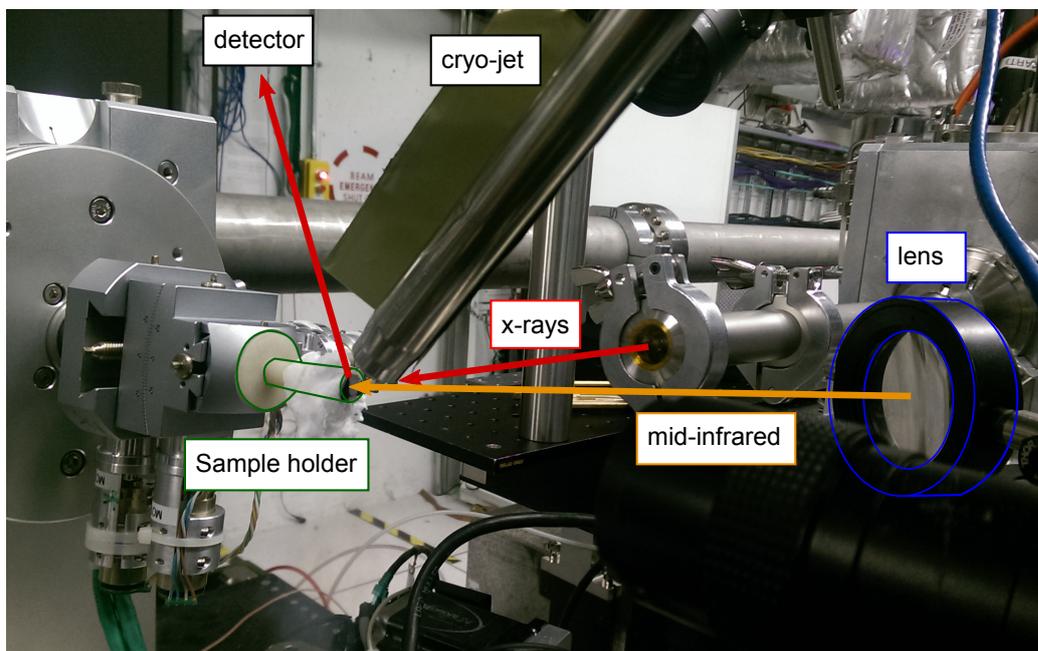
Figure C.1.4: The sample was mounted vertically to a huber goniometer with x-y-z stages, which was fixed to a rotational stage allowing for φ-rotation around the sample surface. A commercial nitrogen blower from Oxford Cryosystems was used to cool the sample to 100 K. The incidence angle of the x-ray beam was 5°, the mid-infrared beam was focused with a KBr lens, incident at an angle of 18° with respect to the sample surface normal. The diffracted x-ray pulses were measured with a diode, attached to a robot arm.

non-coplanar geometry, in which the angle of incidence α and the φ-rotation select the diffraction condition for certain Bragg peaks. The direction of the diffracted x-rays are defined by the azimuth and elevation angles δ and η, respectively, as shown in Figure C.1.5.

The measurement was done in grazing incidence geometry with a grazing angle of 5°, chosen to match the penetration depth of x-ray and mid-infrared light. P-polarized mid-infrared pulses were generated next to the experiment in a commercial optical parametric amplifier system by difference frequency generation in GaSe (see Appendix A.2) and focused on the sample using a KBr lens. Both for the $La_{0.7}Sr_{0.3}MnO_3$ (LSMO) and the $YBa_2Cu_3O_{6.5}$ (YBCO) experiments, the surface normal was the polarization axis of the
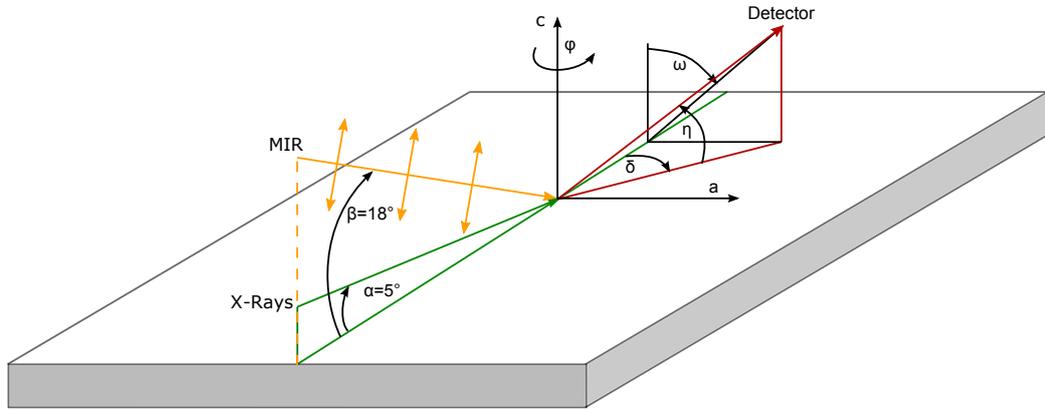
Figure C.1.5: The x-ray diffraction experiments were done in a non-coplanar geometry, in which the angle of incidence α and the φ-rotation select the diffraction condition for certain Bragg peaks. The direction of the diffracted x-rays (red) are defined by the azimuth and elevation angles δ and η, respectively. The incidence angles of x-ray and p-polarized mid-infrared beams were 5° and 18° with respect to the sample surface.

infrared-active phonon mode. The incidence angle of the mid-infrared pulses has to be chosen from a trade-off between losses in the excitation efficiency of the infrared phonon due to reflectivity, polarization of the electric field in the material and spot size elongation. While the spot size elongates with decreasing incidence angle β according to $1/\sin(\beta)$, reflectivity losses are minimized at the Brewster angle of $\sim$20°. Further, for efficient phonon excitation, the electric field should mainly be polarized along the polarization axis of the phonon, that is, the incidence angle should be small. The incidence angle of the p-polarized mid-infrared light was fixed at 18° with respect to the sample surface. This angle of incidence is close to the Brewster angle, ensuring a low reflectivity. Further, the decrease in time resolution due to the angle of 13° between x-ray and mid-infrared beams was negligible, as the time resolution was limited by the jitter between pump and probe pulses to 200 fs. Figure C.1.6 shows the efficiency of phonon excitation, which has a maximum at an incidence angle of 35°.
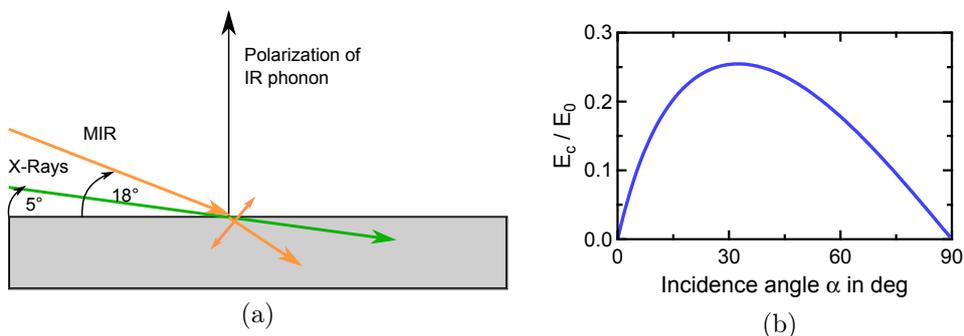
Figure C.1.6: a) The incidence angles of x-ray and mid-infrared beams were 5° and 18° with respect to the sample surface. The incidence angle of the x-rays were chosen to match the penetration depths of pump and probe pulses. b) The incidence angle α of the mid-infrared pulses results from a trade off between losses due to reflectivity, which are minimized at the Brewster angle of $\sim$20°, and losses due to the wrong polarization of the electric field in the material and spot size elongation. Shown is the angular dependence of the electric field in the material polarized along the c-axis and normalized to the incident electric field E_c for YBCO at 100 K. Note that this plot does not take into account the angular dependence of the penetration depth of the mid-IR.

Spot sizes and penetration depth

The minimal spot sizes of the mid-infrared pulses normal to the propagation direction were $250 \times 250 \mu m^2$ and $290 \times 225 \mu m^2$ (vertical $\times$ horizontal) for the experiments on LSMO and YBCO, respectively. The x-ray spot size was $60 \times 60 \mu m^2$ in both experiments. For YBCO, the penetration depth of the mid-infrared pulses along the surface normal was $\sim 1 \mu m$, the penetration depth of the x-rays $0.7 \mu m$ (both denote the distance at which the intensity is reduced to $1/e$). The x-ray penetration depth was calculated from the absorption coefficient, which is available online [2]. The penetration depth of the mid-infrared pulses along the surface normal is given by $\sin\left(\beta'\right) c/\left(4\pi f k\right)$, where β' is the angle between sample surface and propagation direction of the mid-infrared light in the material, c the velocity of light, f the frequency of the mid-infrared light and k the imaginary part of the refractive index. YBCO has different refractive indices for light polarized along the out-of

---

[2]http://henke.lbl.gov/optical_constants/atten2.html

plane direction **c** and the in-plane directions **a** and **b** and can be treated as a uniaxial crystal for the calculation of the refractive index for waves traveling with a **k**-vector with components along **a** and **c**. The refractive index then only depends on the angle ϑ of the **k** vector with respect to the crystallographic **c**-direction and is given by

$$n\left(\vartheta\right) = \frac{n_{ab} \cdot n_c}{\left(n_c^2 \cos^2\left(\vartheta\right) + n_{ab}^2 \sin^2\left(\vartheta\right)\right)},$$

where n_{ab} and n_c are the in-plane and out-of plane refractive indices for light with a given frequency. Even though penetration depth and spot size were larger for mid-infrared pulses, the probed volume was not homogeneously pumped. The average field of the mid-infrared light in the probed volume was smaller by a factor of 2.4 compared to the incident field. This mismatch was taken into account in the calculated crystal structure of YBCO in its excited state. As the infrared mode amplitude is proportional to the electric field of the pump pulse, the displaced structure was reported for a B_{1u} mode amplitude of 0.3, larger by a factor of ~ 2.4 compared to the experimentally determined structure.

C.1.4 Data collection

Filters and normalization

As shot to shot fluctuations of the x-ray pulse intensity can be very large, the experimentally acquired data has to be filtered and normalized to the measured x-ray intensity. Panel (a) of Figure C.1.7 shows the correlation between the measured diffracted intensity of the (2-11) Bragg peak of YBCO at 100 K and the measured x-ray intensity for $\sim$10000 shots. Panel b) of the same Figure shows a histogram of the diffracted intensity as measured and normalized shot by shot in blue and red, respectively. After the normalization, a much narrower Gaussian distribution is obtained. In addition to the intensity filter, a position filter is applied by comparing the relative intensities measured on the four channels of the intensity monitor. Shots with large deviations from the average ratio are disregarded. The red part

of the data shown in Figure C.1.8 is used for further processing, the fraction of shots eliminated by the filters was around (5-10) %.

Temporal and spatial overlap

To check spatial overlap, a piece of liquid crystal paper and thin 100 µm YAG screen were mounted on the sample holder, partially overlapping. The heat generated by the mid-infrared pulses changes the color of the liquid crystal paper, the x-ray pulses induce fluorescence of the YAG screen. Both pulses become visible and can be overlapped. The coarse temporal overlap was determined by steering both x-ray pulses and mid-IR pulses onto an SMA cable. The pulses induce an electric pulse, which can be measured with a scope and overlapped with a resolution of $\sim$20-30 ps. Following the coarse timing, the exact time zero was measured using the (111) reflection of Bismuth, which experiences a large drop in intensity following mid-infrared excitation as shown in Figure C.1.9. The response time of 250 fs was limited by the time resolution of the experiment. Following the time scan, lens-scans were performed to optimize the spatial overlap.


(a)   (b)
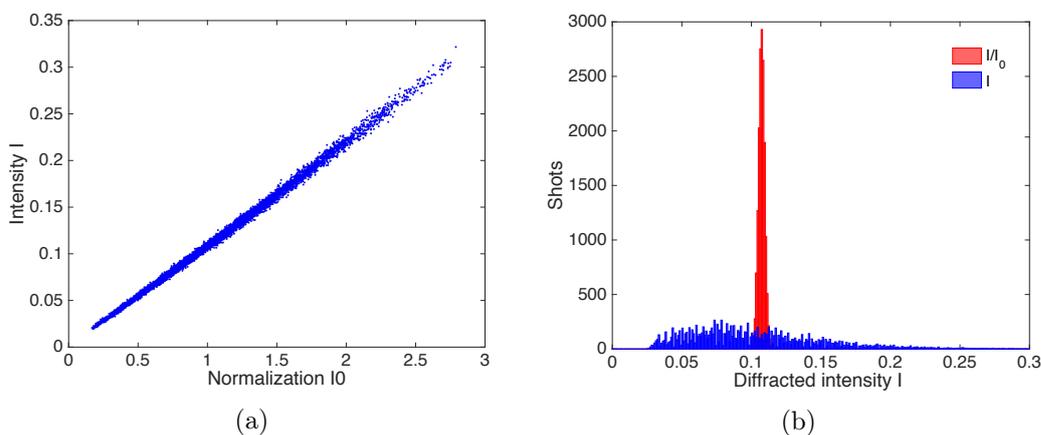
Figure C.1.7: a) Shown is the correlation between measured diffracted intensity I and the summed signal from the four x-ray intensity monitors I_0 for $\sim$10000 shots. b) The histogram of the measured diffraction intensities shows a very large spread (blue). Normalizing the diffracted intensity by the x-ray intensity shot by shot yields a much narrower Gaussian distribution.
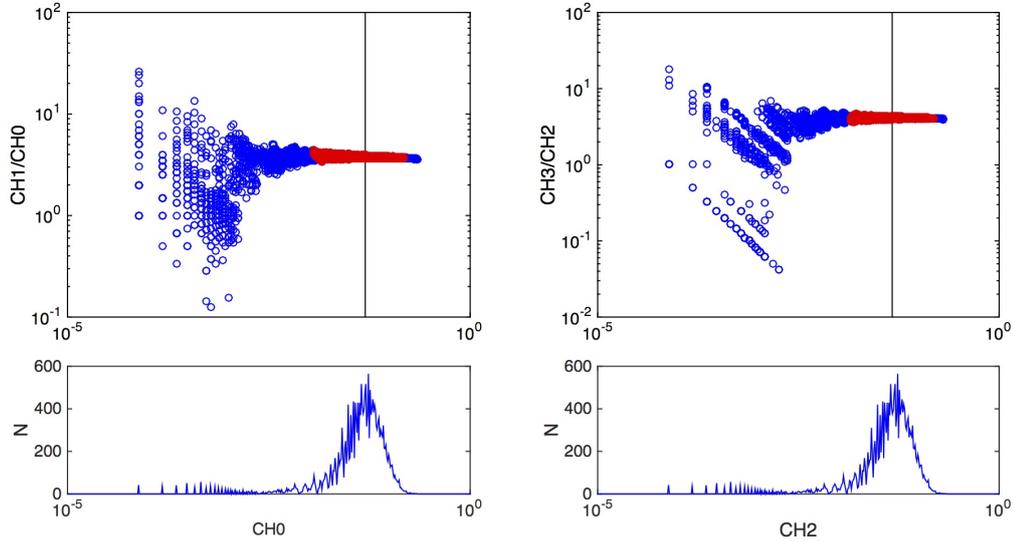
Figure C.1.8: Shown is the relative measured x-ray intensity of two of the four channels of the intensity monitor plotted against one of the channels. The lower panels show a histogram of the signal on the same channel. Shots with a large deviation from the average ratio of the two channels are disregarded. The region marked in red shows the shots that are used for further processing.
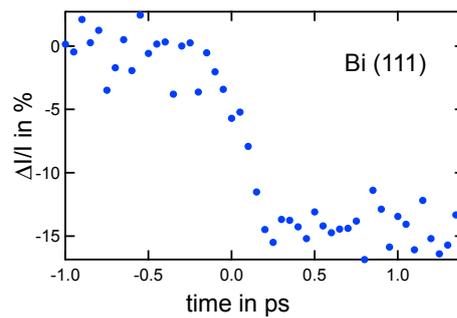

Figure C.1.9: Temporal overlap of mid-infrared pump and x-ray probe pulses was determined using the (111) reflection of Bismuth, which experiences a large drop in intensity following the excitation. The response time of 250 fs was limited by the time resolution of the experiment.
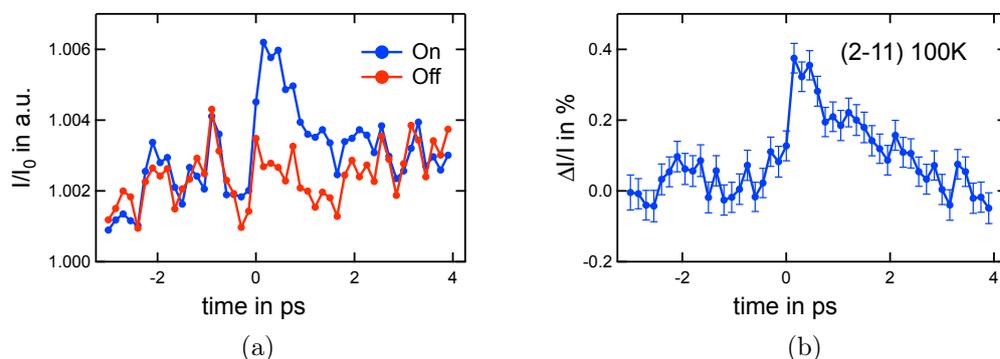
Figure C.1.10: a) The average of 20 time delay scans of the (2-11) reflection of YBCO at 100 K. For each scan, 480 shots were recorded per time step. Every second mid-infrared pump pulse was delayed to negative time delay, yielding a measurement of the equilibrium diffracted intensity for each time step. Short term drifts of the LCLS appear in both the pumped (blue) and the equilibrium signal (red). b) The relative intensity change can then be extracted as $\Delta I/I = I_{On}/I_{Off} - 1$.

Laser repetition rates

During the first experiment on LSMO, both optical and x-ray laser were operated at 120 Hz repetition rate. The time evolution of the diffracted intensity was obtained by delaying the optical pump pulses with respect to the x-ray pulses. Typically, 20 scans were measured in series, with 480 shots per time delay and step sizes of 150 fs. For the experiment on YBCO, we chose to delay every second pump pulse to negative time delays. This procedure allows for the correction of drifts of the LCLS properties on the scale of minutes by consecutively recording the excited and equilibrium state of the material. An example scan of the (2-11) diffraction peak is shown in Figure C.1.10. The blue curve shows the signal of the excited state I_{On}, the red curve the equilibrium state I_{Off}. The relative intensity change following the mid-infrared excitation can then be extracted as $\Delta I/I = I_{On}/I_{Off} - 1$ (see panel b) of the same Figure).
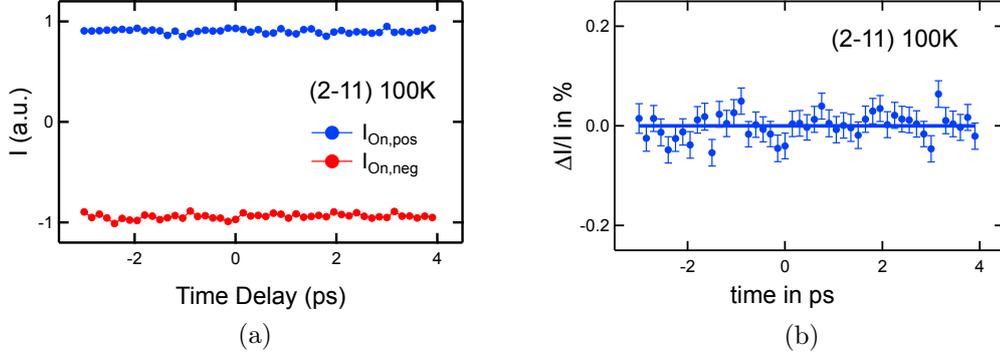
Figure C.1.11: Sorting the measured intensity of the pumped time delay trace for positive $I_{\mathrm{On,pos}}$ and negative $I_{\mathrm{On,neg}}$ deviations from the average yields the blue and red curves, respectively. The signal from Q^2Q^2 contributions can then be extracted by first subtracting the positive and negative deviations of the equilibrium diffracted intensity, which corresponds to the noise level of the experiment. Subsequent averaging of the absolute positive and negative residuals yields the blue curve, which shows no pump induced signals $\left(|I_{\mathrm{On,pos}} - I_{\mathrm{Off,pos}}| + |I_{\mathrm{On,neg}} - I_{\mathrm{Off,neg}}|\right)/2$.

C.1.5   Data analysis quartic coupling

The direction of the lattice displacements due to fourth order coupling depends on the velocity and position of the coupled Raman mode before excitation as described in section 1.2. In a typical pump-probe experiment the signal is obtained by fixing the time delay and averaging the measured diffracted intensity over many shots. Any random contributions such as quartic effects would however average to zero.

In order to extract the contributions from fourth order coupling, the difference in diffracted intensity of each individual shot from the average intensity over all shots has to be determined and sorted for positive and negative deviations for the pumped and equilibrium time traces, respectively. The positive $I_{\mathrm{On,pos}}$ and negative $I_{\mathrm{On,neg}}$ residuals for the pumped time trace are shown in Figure C.1.11 for the (-211) peak at 100 K. The constant offset of the curves corresponds to the average noise level. The time-dependent positive and negative signals can be extracted by subtracting the residuals of the equilibrium

signal from the pumped time trace. The relative change in diffracted intensity as shown in panel b) can then be obtained by averaging the modulus of the relative signals $\left(\left| I_{\text{On,pos}} - I_{\text{Off,pos}} \right| / I_{\text{Off,pos}} + \left| I_{\text{On,neg}} - I_{\text{Off,neg}} \right| / I_{\text{Off,neg}} \right) / 2$.

C.2   Additional information

All time-scans were done at the maximum of the diffraction curve. From these measurements alone it cannot be deduced, whether the observed change in diffracted intensity is due to a shift of the peak position, corresponding to a contraction or elongation of the crystal or a change in structure factors, which results in a uniform percentage decrease in scattering efficiency. We thus took rocking curves of the (-2-11) diffraction peak at 100 K at fixed pump-probe time-delay corresponding to the largest change in peak intensity. As shown in Figure C.2.1a, the change in diffracted intensity is uniform over the whole peak, confirming a change in structure factors as cause for the observed dynamics.

The dynamics for longer times are shown in Figure C.2.1b for the (-2-11) peak at 100 K. Following the positive signal, we observe a very small decrease
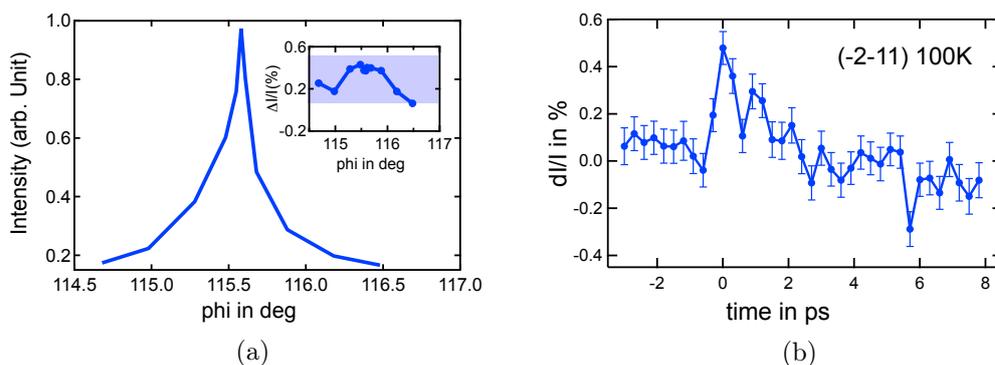

Figure C.2.1: (a) Measurement of the (-2-11) diffraction peak at 100 K. The inset shows the measured relative intensity change in percent at fixed pump-probe time-delay corresponding to the largest change in peak intensity. (b) Relative change in diffracted intensity of the same peak. At longer delays we observe a small decrease in peak intensity, which might be due to the Debye waller effects or small shifts of the diffraction peak.

in diffracted intensity below the equilibrium value, possibly due to Debye waller effects or lattice expansion. This decrease is however almost within the uncertainty of the experiment.

C.3 Density functional calculations

The calculations were performed by Alaska Subedi and are reported in [33].

Frozen phonon calculations

The phonon modes and the nonlinear phonon couplings were obtained using density functional theory (DFT) calculations with plane-wave basis sets and projector augmented-wave pseudo potentials [90, 91] as implemented in the VASP software package [92]. The local density approximation was used for the exchange and correlations. We used a cut-off energy of 950 eV for plane-wave expansion and a $4\times8\times4$ k-point grid for the Brillouin zone integration in the self-consistent cycles. We used the experimental lattice parameters of the $YBa_2Cu_3O_{6.5}$ ortho-II structure, but relaxed the internal coordinates. The interatomic force constants were calculated using the frozen-phonon method [93], and the PHONOPY software package was used to calculate the phonon frequencies and normal modes [94]. After the normal modes were identified, the total energy was calculated as a function of the Q_{ir} and Q_R phonon mode amplitudes to obtain the energy surfaces. The nonlinear coupling between the infrared and Raman modes was obtained by fitting the energy surfaces to the polynomial

$$H = \frac{1}{2}\omega_{ir}^2 Q_{ir}^2 + \frac{1}{2}\omega_R^2 Q_R^2 - a_{21}Q_{ir}^2 Q_R.$$

Calculations of the electronic structure

The changes in the electronic structure due to the light-induced distortions were studied using the generalized full-potential method within the local-density approximation as implemented in the WIEN2k package [95]. Muffin-tin radii of 2.35, 2.5, 1.78 and 1.53 Bohr radii (one Bohr radius equals 0.529

Å) were used for Y, Ba, Cu and O, respectively, and a $20 \times 40 \times 20$ k-point grid was used for the Brillouin zone integration. The plane-wave cut-off was set such that $RK_{max} = 7.0$, where K_{max} is the plane-wave cut-off and R is the small muffin-tin radius, that is, 1.53 Bohr radii. The density of states was generated with a $32 \times 64 \times 32$ k-point grid.

Bibliography

[1] Lacorre, P., Torrance, J., Pannetier, J., Nazzal, A., Wang, P., and Huang, T. Synthesis, crystal structure, and properties of metallic $PrNiO_3$: Comparison with metallic $NdNiO_3$ and semiconducting $SmNiO_3$. *Journal of Solid State Chemistry* **91**(2), 225–237 (1991).

[2] Torrance, J. B., Lacorre, P., Nazzal, a. I., Ansaldo, E. J., and Niedermayer, C. Systematic study of insulator-metal transitions in perovskites $RNiO_3$ (R=Pr,Nd,Sm,Eu) due to closing of charge-transfer gap. *Physical Review B* **45**(14), 8209–8212 (1992).

[3] Van Santen, J. and Jonker, G. Electrical conductivity of ferromagnetic compounds of manganese with perovskite structure. *Physica* **16**(7-8), 599–600 (1950).

[4] Volger, J. Further experimental investigations on some ferromagnetic oxidic compounds of manganese with perovskite structure. *Physica* **20**(1), 49–66 (1954).

[5] Bednorz, J. G. and Müller, K. A. Possible High-Tc Superconductivity in the Ba-La-Cu-O System. *Zeitschrift für Physik B Condensed Matter* **64**(2), 189–193 (1986).

[6] Fausti, D., Tobey, R. I., Dean, N., Kaiser, S., Dienst, A., Hoffmann, M. C., Pyon, S., Takayama, T., Takagi, H., and Cavalleri, A. Light-induced superconductivity in a stripe-ordered cuprate. *Science* **331**(6014), 189–191 (2011).

[7] Kaiser, S., Hunt, C. R., Nicoletti, D., Hu, W., Gierz, I., Liu, H. Y., Le Tacon, M., Loew, T., Haug, D., Keimer, B., and Cavalleri, A. Optically induced coherent transport far above Tc in underdoped $YBa_2Cu_3O_{6+x}$. *Physical Review B* **89**(18), 184516 (2014).

[8] Hu, W., Kaiser, S., Nicoletti, D., Hunt, C. R., Gierz, I., Hoffmann, M. C., Le Tacon, M., Loew, T., Keimer, B., and Cavalleri, A. Optically enhanced coherent transport in $YBa_2Cu_3O_{6.5}$ by ultrafast redistribution of interlayer coupling. *Nature materials* **13**(May), 705–711 (2014).

[9] Rini, M., Tobey, R., Dean, N., Itatani, J., Tomioka, Y., Tokura, Y., Schoenlein, R. W., and Cavalleri, A. Control of the electronic phase of a manganite by mode-selective vibrational excitation. *Nature* **449**(7158), 72–74 (2007).

[10] Caviglia, A. D., Scherwitzl, R., Popovich, P., Hu, W., Bromberger, H., Singla, R., Mitrano, M., Hoffmann, M. C., Kaiser, S., Zubko, P., Gariglio, S., Triscone, J. M., Först, M., and Cavalleri, A. Ultrafast strain engineering in complex oxide heterostructures. *Physical Review Letters* **108**(13), 136801 (2012).

[11] Först, M., Tobey, R. I., Wall, S., Bromberger, H., Khanna, V., Cavalieri, A. L., Chuang, Y. D., Lee, W. S., Moore, R., Schlotter, W. F., Turner, J. J., Krupin, O., Trigo, M., Zheng, H., Mitchell, J. F., Dhesi, S. S., Hill, J. P., and Cavalleri, A. Driving magnetic order in a manganite by ultrafast lattice excitation. *Physical Review B - Condensed Matter and Materials Physics* **84**(24), 241104 (2011).

[12] Först, M., Caviglia, A. D., Scherwitzl, R., Mankowsky, R., Zubko, P., Khanna, V., Bromberger, H., Wilkins, S. B., Chuang, Y.-D., Lee, W. S., Schlotter, W. F., Turner, J. J., Dakovski, G. L., Minitti, M. P., Robinson, J., Clark, S. R., Jaksch, D., Triscone, J.-M., Hill, J. P., Dhesi, S. S., and Cavalleri, A. Spatially resolved ultrafast magnetic dynamics initiated at a complex oxide heterointerface. *Nature Materials* **14**(9), 883–888 (2015).

[13] Sommerfeld, A. Zur Eletronentheorie der Metalle auf Grund der Fermischen Statistik. *Zeitschrift für Physik* **47**, 1–32 (1927).

[14] Bloch, F. Über die Quantenmechanik der Elektronen in Kristallgittern. *Zeitschrift für Physik* **52**(7-8), 555–600 (1929).

[15] de L. Kronig, R. and Penney, W. G. Quantum Mechanics of Electrons in Crystal Lattices. *Proceedings of the royal society of London series A* **130**(814), 499–513 (1930).

[16] Mott, N. F. Conduction of Electricity in Solids. *Nature* **139**, 951–954 (1937).

[17] Mott, N. F. The Basis of the Electron Theory of Metals, with Special Reference to the Transition Metals. *Proceedings of the Physical Society. Section A* **62**(7), 416–422 (1949).

[18] Mott, N. F. Metal-insulator transition. *Reviews of Modern Physics* **40**(4), 677–683 (1968).

[19] Anslyn, E. V. and Dougherty, D. A. *Modern Physical Organic Chemistry*, volume 43. University Science Books, (2004).

[20] Hwang, H. Y., Palstra, T. T. M., Cheong, S.-W., and Batlogg, B. Pressure effects on the magnetoresistance in doped manganese perovskites. *Physical Review B* **52**(21), 15046–15049 (1995).

[21] Hwang, H. Y., Cheong, S.-W., Radaelli, P. G., Marezio, M., and Batlogg, B. Lattice Effects on the Magnetoresistance in Doped $LaMnO_3$. **75**(4), 729–732 (1995).

[22] Först, M., Manzoni, C., Kaiser, S., Tomioka, Y., Tokura, Y., Merlin, R., and Cavalleri, A. Nonlinear phononics as an ultrafast route to lattice control. *Nature Physics* **7**(11), 854–856 aug (2011).

[23] Maradudin, A. A. and Wallis, R. F. Ionic Raman Effect. I. Scattering by Localized Vibration Modes. *Physical Review B* **2**(10), 4294–4299 (1970).

[24] Wallis, R. F. and Maradudin, A. A. Ionic Raman Effect. II. The First-Order Ionic Raman Effect. *Physical Review B* **3**(6), 2063–2075 (1971).

[25] Martin, T. P. and Genzel, L. Ionic Raman Scattering and Ionic Frequency Mixing. *Physica Status Solidi (B)* **61**(2), 493–502 feb (1974).

[26] Först, M., Mankowsky, R., Bromberger, H., Fritz, D. M., Lemke, H., Zhu, D., Chollet, M., Tomioka, Y., Tokura, Y., Merlin, R., Hill, J. P., Johnson, S. L., and Cavalleri, A. Displacive lattice excitation through nonlinear phononics viewed by femtosecond X-ray diffraction. *Solid State Communications* **169**, 24–27 (2013).

[27] Fink, J., Soltwisch, V., Geck, J., Schierle, E., Weschke, E., and Büchner, B. Phase diagram of charge order in $La_{1.8-x}Eu_{0.2}Sr_xCuO_4$ from resonant soft x-ray diffraction. *Physical Review B* **83**, 092503 (2011).

[28] Först, M., Tobey, R. I., Bromberger, H., Wilkins, S. B., Khanna, V., Caviglia, a. D., Chuang, Y. D., Lee, W. S., Schlotter, W. F., Turner, J. J., Minitti, M. P., Krupin, O., Xu, Z. J., Wen, J. S., Gu, G. D., Dhesi, S. S., Cavalleri, A., and Hill, J. P. Melting of charge stripes in vibrationally driven $La_{1.875}Ba_{0.125}CuO_4$: Assessing the respective roles of electronic and lattice order in frustrated superconductors. *Physical Review Letters* **112**(15), 157002 (2014).

[29] Huber, J. G. and Liverman, W. J. Superconductivity under high pressure of $YBa_2(Cu_{1-x}M_x)_3O_{7-\delta}$ (M = Fe, Co, Al, Ni, and Zn). *Physical Review B* **41**(13), 8757–8761 (1990).

[30] Schirber, J. E., Ginley, D. S., Venturini, E. L., and Morosin, B. Pressure dependence of the superconducting transition temperature in the 94-K superconductor $YBa_2Cu_3O_7$. *Physical Review B* **35**(16), 8709–8710 (1987).

[31] Bucher, B., Karpinski, J., Kaldins, E., and Wachter, P. Pressure Dependence of Tc and anisotropic Features in the Family $Y_2Ba_4Cu_{6+m}O_{16+n}$. *Journal of Less-Common Metals* **164, 165**, 20–30 (1990).

[32] Jorgensen, J., Pei, S., Lightfoot, P., Hinks, D., Veal, B., Dabrowski, B., Paulikas, A., Kleb, R., and Brown, I. Pressure-induced charge transfer and dT_c/dP in $YBa_2Cu_3O_{7-x}$. *Physica C: Superconductivity* **171**, 93–102 (1990).

[33] Mankowsky, R., Subedi, A., Först, M., Mariager, S. O., Chollet, M., Lemke, H. T., Robinson, J. S., Glownia, J. M., Minitti, M. P., Frano, A., Fechner, M., Spaldin, N. A., Loew, T., Keimer, B., Georges, A., and Cavalleri, A. Nonlinear lattice dynamics as a basis for enhanced superconductivity in $YBa_2Cu_3O_{6.5}$. *Nature* **516**(7529), 71–73 (2014).

[34] Raines, Z. M., Stanev, V., and Galitski, V. M. Enhancement of superconductivity via periodic modulation in a three-dimensional model of cuprates. *Physical Review B* **91**(18), 184506 (2015).

[35] Homes, C., Timusk, T., Bonn, D. A., Liang, R., and Hardy, N. Optical properties along the c-axis of $YBa_2Cu_3O_{6+x}$, for x = 0.50 0.95 Evolution of the pseudogap. *Physica C* **254**, 265–280 (1995).

[36] Raman, C. V. and Krishnan, K. S. A New Type of Secondary Radiation. *Nature* **121**(3048), 501–502 (1928).

[37] Long, D. A. *The Raman Effect: A Unified Treatment of the Theory of Raman Scattering by Molecules.* John Wiley & Sons Ltd, (2002).

[38] Mayer, A. and Keilmann, F. Far-infrared nonlinear optics. I. Chi(2) near ionic resonance. *Physical Review B* **33**(10), 6954–6961 (1986).

[39] Mills, D. L. Ionic contributions to the Raman tensor of insulators. *Physical review. B, Condensed matter* **35**(17), 9278–9283 jun (1987).

[40] Mankowsky, R., Först, M., Loew, T., Porras, J., Keimer, B., and Cavalleri, A. Coherent modulation of the $YBa_2Cu_3O_{6+x}$ atomic structure by displacive stimulated ionic Raman scattering. *Physical Review B* **91**(9), 094308 (2015).

[41] Subedi, A., Cavalleri, A., and Georges, A. Theory of nonlinear phononics for coherent light control of solids. *Physical Review B* **89**, 220301 (2014).

[42] Garrett, G. A., Albrecht, T., Whitaker, J., and Merlin, R. Coherent THz Phonons Driven by Light Pulses and the Sb Problem: What is the Mechanism? *Physical Review Letters* **77**(17), 3661–3664 (1996).

[43] Merlin, R. Generating coherent THz phonons with light pulses. *Solid State Communications* **102**(2-3), 207–220 (1997).

[44] Stevens, T., Kuhl, J., and Merlin, R. Coherent phonon generation and the two stimulated Raman tensors. *Physical Review B* **65**(14), 144304 mar (2002).

[45] Garrett, G. A., Whitaker, J., Sood, A., and Merlin, R. Ultrafast Optical Excitation of a Combined Coherent-Squeezed Phonon field in SrTiO$_3$. *Optics express* **1**(12), 385–389 (1997).

[46] Garrett, G. A. Vacuum Squeezing of Solids: Macroscopic Quantum States Driven by Light Pulses. *Science* **275**(5306), 1638–1640 (1997).

[47] Bartels, A., Dekorsy, T., and Kurz, H. Impulsive excitation of phonon-pair combination states by second-order raman scattering. *Physical Review Letters* **84**(13), 2981 (2000).

[48] Subedi, A. Proposal for ultrafast switching of ferroelectrics using mid-infrared pulses. *arXiv* , 1511.00149 (2015).

[49] Xiang, H. J. Origin of polar distortion in LiNbO$_3$-type "ferroelectric" metals: Role of A-site instability and short-range interactions. *Physical Review B* **90**(9), 094108 (2014).

[50] Chollet, M., Alonso-Mori, R., Cammarata, M., Damiani, D. S., Defever, J., Delor, J. T., Feng, Y., Glownia, J. M., Langton, J. B., Nelson, S., Ramsey, K., Robert, A., Sikorski, M., Song, S., Stefanescu, D., Srinivasan, V., Zhu, D., Lemke, H. T., and Fritz, D. M. The X-ray Pump-Probe instrument at the Linac Coherent Light Source. *Journal of Synchrotron Radiation* **22**(3), 1–5 (2015).

[51] Goodenough, J. B. Theory of the role of covalence in the perovskite-type manganites [La,M(II)]MnO$_3$. *Physical Review* **100**(2), 564–573 (1955).

Bibliography

[52] Urushibara, A., Arima, T., Asamitsu, A., Kido, G., and Tokura, Y. Insulator-metal transition and giant magnetoresistance in $La_{1-x}Sr_xMnO_3$. *Physical Review B* **51**(20), 14103–14109 (1995).

[53] Tomioka, Y., Asamitsu, A., Kuwahara, H., and Moritomo, Y. Magnetic-field-induced metal-insulator phenomena in $Pr_{1-x}Ca_xMnO_3$ with controlled charge-ordering instability. *Physical Review B* **53**(4), 1689–1692 (1996).

[54] Miyano, K., Tanaka, T., Tomioka, Y., and Tokura, Y. Photoinduced Insulator-to-Metal Transition in a Perovskite Manganite. *Physical Review Letters* **78**(22), 4257–4260 (1997).

[55] Kiryukhin, V., Casa, D., Hill, J. P., Keimer, B., Vigliante, A., Tomioka, Y., and Tokura, Y. An X-ray-induced insulator-metal transition in a magnetoresistive manganite, (1997).

[56] Fiebig, M., Miyano, K., Tomioka, Y., and Tokura, Y. Visualization of the Local Insulator-Metal Transition in $Pr_{0.7}Ca_{0.3}MnO_3$. *Science* **280**(5371), 1925–1928 (1998).

[57] Dubroka, A., Rössle, M., Kim, K. W., Malik, V. K., Munzar, D., Basov, D. N., Schafgans, A. A., Moon, S. J., Lin, C. T., Haug, D., Hinkov, V., Keimer, B., Wolf, T., Storey, J. G., Tallon, J. L., and Bernhard, C. Evidence of a precursor superconducting phase at temperatures as high as 180 K in $RBa_2Cu_3O_{7-\delta}$ (R=Y,Gd,Eu) superconducting crystals from infrared spectroscopy. *Physical Review Letters* **106**(4), 047006 (2011).

[58] Pavarini, E., Dasgupta, I., Saha-Dasgupta, T., Jepsen, O., and Andersen, O. K. Band-structure trend in hole-doped cuprates and correlation with T(c max). *Physical review letters* **87**(4), 047003 (2001).

[59] Meissner, W. and Ochsenfeld, R. Ein neuer Effekt bei Eintritt der Supraleitfähigkeit. *Die Naturwissenschaften* **21**(44), 787–788 (1933).

[60] Wu, M. K., Ashburn, J. R., Torng, C. J., Hor, P. H., Meng, R. L., Gao, L., Huang, Z. J., Wang, Y. Q., and Chu, C. W. Superconductivity at

155

93 K in a new mixed-phase Yb-Ba-Cu-O compound system at ambient pressure. *Physical Review Letters* **58**(9), 908–910 (1987).

[61] Mankowsky, R. Supraleitung bei Raumtemperatur. *Physik in unserer Zeit* **46**(5), 238–244 (2015).

[62] Blackburn, E., Chang, J., Hücker, M., Holmes, A. T., Christensen, N. B., Liang, R., Bonn, D. A., Hardy, W. N., Rütt, U., Gutowski, O., Zimmermann, M. V., Forgan, E. M., and Hayden, S. M. X-ray diffraction observations of a charge-density-wave order in superconducting ortho-II YBa$_2$Cu$_3$O$_{6.54}$ single crystals in zero magnetic field. *Physical Review Letters* **110**(13), 137004 (2013).

[63] Blanco-Canosa, S., Frano, A., Schierle, E., Porras, J., Loew, T., Minola, M., Bluschke, M., Weschke, E., Keimer, B., and Le Tacon, M. Resonant x-ray scattering study of charge-density wave correlations in YBa$_2$Cu$_3$O$_{6+x}$. *Physical Review B* **90**(5), 054513 (2014).

[64] Hashimoto, M., Vishik, I. M., He, R.-H., Devereaux, T. P., and Shen, Z.-X. Energy gaps in high-transition-temperature cuprate superconductors. *Nature Physics* **10**(7), 483–495 (2014).

[65] Tranquada, J. M. Stripes and superconductivity in cuprates. *Physica B: Condensed Matter* **407**(11), 1771–1774 (2012).

[66] Lu, D. H., Feng, D. L., Armitage, N. P., Shen, K. M., Damascelli, A., Kim, C., Ronning, F., Shen, Z. X., Bonn, D. A., Liang, R., Hardy, W. N., Rykov, A. I., and Tajima, S. Superconducting gap and strong in-plane anisotropy in untwinned YBa$_2$Cu$_3$O$_{7-\delta}$. *Physical Review Letters* **86**(19), 4370–4373 (2001).

[67] Nakayama, K., Sato, T., Terashima, K., Arakane, T., Takahashi, T., Kubota, M., Ono, K., Nishizaki, T., Takahashi, Y., and Kobayashi, N. Doping dependence of the gap anisotropy of the high-temperature YBa$_2$Cu$_3$O$_{7-\delta}$ superconductor. *Physical Review B* **79**(14), 140503 (2009).

[68] Ghiringhelli, G., Le Tacon, M., Minola, M., Blanco-Canosa, S., Mazzoli, C., Brookes, N. B., De Luca, G. M., Frano, A., Hawthorn, D. G., He, F., Loew, T., Sala, M. M., Peets, D. C., Salluzzo, M., Schierle, E., Sutarto, R., Sawatzky, G. a., Weschke, E., Keimer, B., and Braicovich, L. Long-Range Incommensurate Charge Fluctuations in $(Y,Nd)Ba_2Cu_3O_{6+x}$. *Science* **337**(6096), 821–825 (2012).

[69] Chang, J., Blackburn, E., Holmes, A. T., Christensen, N. B., Larsen, J., Mesot, J., Liang, R., Bonn, D. A., Hardy, W. N., Watenphul, A., Zimmermann, M. V., Forgan, E. M., and Hayden, S. M. Direct observation of competition between superconductivity and charge density wave order in $YBa_2Cu_3O_{6.67}$. *Nature Physics* **8**(12), 871–876 (2012).

[70] Josephson, B. Possible new effects in superconductive tunnelling. *Physics Letters* **1**(7), 251–253 (1962).

[71] van der Marel, D. and Tsvetkov, A. Transverse optical plasmons in layered superconductors. *Czechoslovak Journal of Physics* **46**, 3165–3168 (1996).

[72] Munzar, D., Bernhard, C., Golnik, A., Humlíček, J., and Cardona, M. Anomalies of the infrared-active phonons in underdoped $YBa_2Cu_3O_y$ as evidence for the intra-bilayer Josephson effect. *Solid State Communications* **112**(7), 365–369 (1999).

[73] Timusk, T. The mysterious pseudogap in high temperature superconductors: An infrared view. *Solid State Communications* **127**(5), 337–348 (2003).

[74] Timusk, T. and Homes, C. C. The role of magnetism in forming the c -axis spectral peak at 400 cm^{-1} in high temperature superconductors. *Solid State Communications* **126**, 63–69 (2003).

[75] Orenstein, J. Optical Conductivity and Spatial Inhomogeneity in Cuprate Superconductors. *Handbook of high Temperature superconductors: theory and experiment* **1**, 299–324 (2007).

[76] Zimmermann, M., Schneider, J., Frello, T., Andersen, N., Madsen, J., Käll, M., Poulsen, H., Liang, R., Dosanjh, P., and Hardy, W. Oxygen-ordering superstructures in underdoped $YBa_2Cu_3O_{6+x}$ studied by hard x-ray diffraction. *Physical Review B* **68**(10), 1–13 (2003).

[77] Elfimov, I. S., Sawatzky, G. A., and Damascelli, A. Theory of Fermi-surface pockets and correlation effects in underdoped Y Ba2 Cu3 O6.5. *Physical Review B - Condensed Matter and Materials Physics* **77**(6), 1–4 (2008).

[78] Carrington, A. and Yelland, E. A. Band-structure calculations of Fermi-surface pockets in ortho-II YBa2 Cu3 O6.5. *Physical Review B - Condensed Matter and Materials Physics* **76**(14), 3–6 (2007).

[79] Doiron-Leyraud, N., Proust, C., LeBoeuf, D., Levallois, J., Bonnemaison, J.-B., Liang, R., Bonn, D. A., Hardy, W. N., and Taillefer, L. Quantum oscillations and the Fermi surface in an underdoped high-Tc superconductor. *Nature* **447**(7144), 565–568 (2007).

[80] Först, M., Frano, A., Kaiser, S., Mankowsky, R., Hunt, C. R., Turner, J. J., Dakovski, G. L., Minitti, M. P., Robinson, J., Loew, T., Le Tacon, M., Keimer, B., Hill, J. P., Cavalleri, A., and Dhesi, S. S. Femtosecond x rays link melting of charge-density wave correlations and light-enhanced coherent transport in $YBa_2Cu_3O_{6.6}$. *Physical Review B* **90**, 184514 (2014).

[81] Magnuson, M., Schmitt, T., Strocov, V. N., Schlappa, J., Kalabukhov, A. S., and Duda, L.-C. Self-doping processes between planes and chains in the metal-to-superconductor transition of $YBa_2Cu_3O_{6.9}$. *Scientific Reports* **4**, 7017 (2014).

[82] Albrecht, W., Kruse, T., and Kurz, H. Time-resolved observation of coherent phonons in superconducting $YBa_2Cu_3O_{7-\delta}$ thin films. *Physical Review Letters* **69**(9), 1451–1454 (1992).

[83] Kutt, W. A., Albrecht, W., and Kurz, H. Generation of coherent phonons in condensed media. *IEEE Journal of Quantum Electronics* **28**(10), 2434–2444 (1992).

[84] Mazin, I. I., Liechtenstein, A. I., Jepsen, O., Andersen, O. K., and Rodriguez, C. O. Displacive excitation of coherent phonons in $YBa_2Cu_3O_7$. *Physical Review B* **49**(13), 9210–9213 (1994).

[85] Denny, S. J., Clark, S. R., Laplace, Y., Cavalleri, A., and Jaksch, D. Proposed Parametric Cooling of Bilayer Cuprate Superconductors by Terahertz Excitation. *Physical Review Letters* **114**(April), 137001 (2015).

[86] Höppner, R., Zhu, B., Rexin, T., Cavalleri, A., and Mathey, L. Redistribution of phase fluctuations in a periodically driven cuprate superconductor. *Physical Review B* **91**(10), 104507 (2015).

[87] Cerullo, G. and De Silvestri, S. Ultrafast optical parametric amplifiers. *Review of Scientific Instruments* **74**(1), 1 (2003).

[88] Boyd, R. W. *Nonlinear Optics*. Academic Press, 2 edition, (2007).

[89] Milne, C. J., Pham, V.-T., Gawelda, W., Veen, R. M. V. D., Nahhas, A. E., Johnson, S. L., Beaud, P., Ingold, G., Lima, F., Vithanage, D. A., Benfatto, M., Grolimund, D., Borca, C., Kaiser, M., Hauser, A., Abela, R., Bressler, C., and Chergui, M. Time-resolved x-ray absorption spectroscopy: Watching atoms dance. *Journal of Physics: Conference Series* **190**, 012052 (2009).

[90] Blöchl, P. E. Projector augmented-wave method. *Physical Review B* **50**, 17953 (1994).

[91] Kresse, G. and Joubert, D. From ultrasoft pseudopotentials to the projector augmented-wave method. *Physical Review B* **59**, 1758 (1999).

[92] Kresse, G. and Furthmüller, J. Efficient iterative schemes for ab initio total-energy calculations using a plane-wave basis set. *Physical Review B* **54**, 11169 (1996).

159

[93] Parlinski, K., Li, Z., and Kawazoe, Y. First-principles determination of the soft mode in cubic ZrO2. *Physical Review Letters* **78**, 4068 (1997).

[94] Togo, A., Oba, F., and Tanaka, I. First-principles calculations of the ferroelastic transition between rutile-type and CaCl2-type SiO2 at high pressures. *Physical Review B* **78**, 134106 (2008).

[95] Blaha, P., Schwarz, K., Madsen, G., Kvasnicka, D., and Luitz., J. WIEN2k. *http://www.wien2k.at/* (2001).